Draft version April 23, 2014
Preprint typeset using LaTeX style emulateapj v. 12/16/11

arXiv:1404.5514v1 [astro-ph.GA] 22 Apr 2014

THE COS/UVES ABSORPTION SURVEY OF THE MAGELLANIC STREAM. III: IONIZATION, TOTAL MASS, AND INFLOW RATE ONTO THE MILKY WAY[1]

Andrew J. Fox[2], Bart P. Wakker[3], Kathleen A. Barger[4,5], Audra K. Hernandez[3], Philipp Richter[6,7], Nicolas Lehner[4], Joss Bland-Hawthorn[8], Jane C. Charlton[9], Tobias Westmeier[10], Christopher Thom[2], Jason Tumlinson[2], Toru Misawa[11], J. Christopher Howk[4], L. Matthew Haffner[3,12], Justin Ely[2], Paola Rodriguez-Hidalgo[13,14], & Nimisha Kumari[2,15]

[2] Space Telescope Science Institute, 3700 San Martin Drive, Baltimore, MD 21218
[3] Department of Astronomy, University of Wisconsin–Madison, 475 North Charter St., Madison, WI 53706
[4] Department of Physics, University of Notre Dame, 225 Nieuwland Science Hall, Notre Dame, IN 46556
[5] National Science Foundation Astronomy and Astrophysics Postdoctoral Fellow
[6] Institut für Physik und Astronomie, Universität Potsdam, Haus 28, Karl-Liebknecht-Str. 24/25, 14476, Potsdam, Germany
[7] Leibniz-Institut für Astrophysik Potsdam (AIP), An der Sternwarte 16, 14482 Potsdam, Germany
[8] Institute of Astronomy, School of Physics, University of Sydney, NSW 2006, Australia
[9] Department of Astronomy and Astrophysics, Pennsylvania State University, University Park, PA 16802
[10] ICRAR, The University of Western Australia, 35 Stirling Highway, Crawley WA 6009, Australia
[11] School of General Education, Shinshu University, 3-1-1 Asahi, Matsumoto, Nagano 390-8621, Japan
[12] Space Science Institute, 4750 Walnut Street, Suite 205, Boulder, CO 80301
[13] Department of Physics and Astronomy, York University, 4700 Keele St., Toronto, Ontario, M3J 1P3, Canada
[14] Department of Astronomy and Astrophysics, University of Toronto, 50 St. George Street, Toronto, Ontario, M5S 3H4, Canada
[15] Ecole Polytechnique, Route de Saclay, 91128 Palaiseau, France

Draft version April 23, 2014

ABSTRACT

Dynamic interactions between the two Magellanic Clouds have flung large quantities of gas into the halo of the Milky Way. The result is a spectacular arrangement of gaseous structures including the Magellanic Stream, the Magellanic Bridge, and the Leading Arm (collectively referred to as the Magellanic System). In this third paper of a series studying the Magellanic gas in absorption, we analyze the gas ionization level using a sample of 69 *Hubble Space Telescope*/Cosmic Origins Spectrograph sightlines that pass through or within 30° of the 21 cm-emitting regions. We find that 81% (56/69) of the sightlines show UV absorption at Magellanic velocities, indicating that the total cross section of the Magellanic System is ≈11 000 square degrees, or around a quarter of the entire sky. Using observations of the Si III/Si II ratio together with *Cloudy* photoionization modeling, we calculate the total gas mass (atomic plus ionized) of the Magellanic System to be $\approx 2.0\times10^9\,M_\odot\,(d/55\,\mathrm{kpc})^2$, with the ionized gas contributing around three times as much mass as the atomic gas. This is larger than the current-day interstellar H I mass of both Magellanic Clouds combined, indicating that they have lost most of their initial gas mass. If the gas in the Magellanic System survives to reach the Galactic disk over its inflow time of ∼0.5–1.0 Gyr, it will represent an average inflow rate of ~ 3.7–$6.7\,M_\odot\,\mathrm{yr}^{-1}$, potentially raising the Galactic star formation rate. However, multiple signs of an evaporative interaction with the hot Galactic corona indicate that the Magellanic gas may not survive its journey to the disk fully intact, and will instead add material to (and cool) the corona.

Keywords: ISM: abundances – Magellanic Clouds – Galaxy: halo – Galaxy: evolution – quasars: absorption lines

1. INTRODUCTION

Like other massive spiral galaxies, the Milky Way has a gas-consumption time of a few billion years (e.g. Larson et al. 1980), far shorter than its age. Ongoing fuel replenishment (gaseous accretion) is therefore needed for it to sustain its star formation. Chemical and kinematic studies of stars in the solar neighborhood have shown that the Milky Way has been forming stars at a fairly constant rate for several Gyr (Twarog 1980; Binney et al. 2000; Chiappini et al. 2001), so we know that fuel replenishment has to be occurring. However, several open questions surround *how* accretion onto the Milky Way and other $\approx L_*$ galaxies occurs. Is the accreting gas predominantly cold, warm, or hot? Does it arrive smoothly from the unenriched IGM or episodically following satellite-galaxy interactions? And do most accreting streams become disrupted by fluid instabilities before reaching the disk?

Hydrodynamical simulations offer one approach to answering these questions. They make clear predictions for the physical and chemical state of gas accreting onto galaxies (Kereš et al. 2005, 2009; Bauermeister et al. 2010; Fumagalli et al. 2011; Stewart et al. 2011; Fernández et al. 2012; van de Voort & Schaye 2012; Murante et al. 2012; Joung et al. 2012b; Vogelsberger et al. 2012; Shen et al. 2013). However, clear observational evidence for gas accretion in external galaxies has been hard to find (see

afox@stsci.edu

[1] Based on observations taken under programs 11520, 11524, 11541, 11585, 11598, 11632, 11686, 11692, 12025, 12029, 12038, 12172, 12204, 12212, 12248, 12263, 12264, 12275, 12533, 12536, 12569, 12593, and 12604 of the NASA/ESA Hubble Space Telescope, obtained at the Space Telescope Science Institute, which is operated by the Association of Universities for Research in Astronomy, Inc., under NASA contract NAS 5-26555.

Ribaudo et al. 2011; Lehner et al. 2013; Burchett et al. 2013), largely due to a lack of kinematic information. Unambiguous *spectroscopic* evidence for inflow onto external galaxies exists in only a small number of cases (e.g. Rubin et al. 2012), and in these galaxies the inflow may be metal-enriched.

Fortunately, the Milky Way offers a prime opportunity for studying the fueling of an $\approx L_*$ galaxy. We have detailed knowledge of the neutral-gas distribution around the Galaxy from H I 21 cm observations, and information on the ionized-gas distribution from a large body of absorption-line data taken from ultraviolet (UV) spectra of background QSOs. In both the 21 cm and UV data, gaseous inflow onto the Galaxy can be seen directly among the high-velocity clouds (HVCs), interstellar clouds that are not co-rotating with the Galactic disk. First detected by Muller et al. (1963), HVCs are defined as having LSR velocities $|v_{\rm LSR}| > 100\,{\rm km\,s^{-1}}$ (or sometimes $>90\,{\rm km\,s^{-1}}$; see reviews by Wakker & van Woerden 1997; Richter 2006; Putman et al. 2012). While HVCs trace a variety of interstellar processes, *infalling* HVCs can be identified by their negative velocities in the Galactic-Standard-of-Rest (GSR) frame and their low metallicities.

Most H I HVCs are now known to be within 5–20 kpc of the Galactic disk, based on individual cloud distance measurements (Wakker 2001; Wakker et al. 2008; Thom et al. 2008; Lehner & Howk 2010; Smoker et al. 2011) and on the observation that the HVC sky-covering fraction $f_{\rm HVC}$ measured toward halo stars is similar to $f_{\rm HVC}$ measured toward AGN (Lehner & Howk 2011; Lehner et al. 2012). However, the Magellanic Stream (MS), anchored by the Magellanic Clouds, stands as a notable exception. Although the distance to the MS is poorly constrained, it likely lies in the interval ∼55–200 kpc. The SMC distance gives the lower limit, and we use the tidal models of Besla et al. (2012) to bound the upper limit, although Jin & Lynden-Bell (2008) argue the MS distance near the south Galactic pole is unlikely to exceed 100 kpc (see also Bland-Hawthorn et al. 2013).

The Stream's origin in the Magellanic Clouds is supported by its spatial, kinematic, and chemical properties, but the mechanism by which it was removed from the Clouds has puzzled dynamicists since its discovery in 21 cm observations over forty years ago (Dieter 1971; Wannier & Wrixon 1972; Mathewson et al. 1974)[2]. Recent models favor the tidal removal of much of the Stream during a close encounter between the two Magellanic Clouds ≈2 Gyr ago (Gardiner & Noguchi 1996; Connors et al. 2006; Besla et al. 2010, 2012; Diaz & Bekki 2011, 2012), although ram-pressure stripping (Meurer et al. 1985; Moore & Davis 1994; Mastropietro et al. 2005) and supernova-driven blowout of LMC material (Staveley-Smith et al. 2003; Lehner & Howk 2007; Lehner et al. 2009; Nidever et al. 2008, hereafter N08) may have also contributed to its production. Tidal forces are strongly favored as the mechanism responsible for creating the Leading Arm (LA), the gaseous counterpart to the MS lying in front of the direction of motion of the Magellanic Clouds (Wannier et al. 1972; Mathewson et al. 1974; Putman et al. 1998; Lu et al. 1998).

To probe the Stream's physical and chemical conditions across its full length on the sky, we are conducting an absorption-line survey with both UV (*HST*/Cosmic Origins Spectrograph) and optical (VLT/UVES) spectrographs. In Paper I (Fox et al. 2013a), we presented new MS chemical abundance measurements along the sightlines to the AGN RBS 144 and NGC 7714, and an upper limit on the metallicity toward the QSO PHL 2525. Combined with earlier work on the NGC 7469 sightline (Fox et al. 2010, hereafter F10), there are now three good measurements of ≈0.1 solar metallicity in the main body of the Stream, supporting the view that most of the MS was stripped from the SMC (not the LMC) 1.5–2.5 Gyr ago. This is because the SMC had a metallicity of ≈0.1 solar at that time according to its age-metallicity relation (Pagel & Tautvaisiene 1998; Harris & Zaritsky 2004). However, in Paper II (Richter et al. 2013, see also Gibson et al. 2000), we found a much higher metallicity of 0.5 solar along the inner-Stream sightline to QSO Fairall 9, which passes through a MS filament that can be traced kinematically back to the LMC (N08). This shows that the bifurcation of the Stream, previously seen in its spatial extent (Putman et al. 2003a) and kinematics (N08), is also seen in its metal enrichment. This supports a dual origin for the Stream, with both the SMC and LMC contributing to its origin.

We now turn our attention from the origin of the Stream to its fate, by observing its ionization level, which encodes information on the physical processes occurring as it interacts with the ambient plasma and radiation field. The MS and the LA contain both warm-ionized and highly-ionized material. The warm-ionized phase is seen in Hα emission (Weiner & Williams 1996; Putman et al. 2003b; Bland-Hawthorn et al. 2013; Barger et al. 2014) and absorption in low-ionization UV lines (Lu et al. 1994, 1998; Sembach et al. 2003; Fox et al. 2005a, F10, Paper I, Paper II). Photoionization and/or shock ionization followed by recombination may be responsible for exciting the Hα emission seen from the Stream, including the possibility of ionization by a Seyfert flare at the center of the Milky Way ≈1–3 Myr ago (Bland-Hawthorn et al. 2013). The highly ionized phase in the Stream is seen in C IV (Lu et al. 1994, 1998, F10, Paper II) and O VI (Sembach et al. 2003; Fox et al. 2005a, F10) absorption. These high ions have column-density ratios consistent with an origin in the conductive or turbulent interfaces that surround the Stream, where the warm low-ionization gas adjoins the hot coronal plasma (Fox et al. 2005a).

In this paper, we present the first UV survey of the Stream's ionization properties, using 69 COS sightlines passing through or within 30° of the MS, the LA, or the Magellanic Bridge (MB), the gaseous filament that connects the LMC and SMC. For brevity, we use the phrase "the Magellanic System" (MSys) to encompass the MS, MB, and LA. This is similar to the definition used by Brüns et al. (2005) in their Parkes survey of 21 cm emission from Magellanic gas, except that here we include the ionized outer regions of the MS that are not seen at 21 cm. Furthermore, Brüns et al. (2005) define the "Interface Region" of H I-emitting gas lying in-between the

[2] Parts of the Stream were detected even earlier by Dieter (1965), although the association with the Magellanic Clouds was not realized at that time.

Magellanic Clouds and the Stream proper. In this paper we include that region as part of the Stream, since the two principal MS filaments can be traced kinematically through it back to the Magellanic Clouds (N08), and hence there is no reason to treat it as a distinct object. Physically, the MSys refers to all gas that was stripped from the Magellanic Clouds at some point in the past (though not necessarily all at the same time). We define On-System and Off-System directions as those with and without a detection of H I 21 cm emission at Magellanic velocities. We also define a subset of "LMC-Halo" directions, that lie in the outer halo of the LMC; these are not part of the MS as traditionally defined, but are clearly Magellanic in origin, and hence are included in our analysis.

We also include Wisconsin H-alpha Mapper (WHAM) observations of Hα emission from the Stream in six of the MS sightlines and three of the MB sightlines. This allows us to compare the optical, radio, and UV profiles of the Magellanic gas in the same directions. Throughout the paper we use solar (photospheric) elemental abundances from Asplund et al. (2009) and absorption-line data (rest wavelengths and oscillator strengths) from Morton (2003). We present all velocities in the kinematical local standard-of-rest (LSR) frame, and all column densities are given in units of cm^{-2}.

This paper is laid out as follows. §2 describes the sample assembly, observations, data handling procedures, and absorption-line measurements. §3 presents an overview of the UV absorption-line profiles and WHAM emission-line profiles. §4 discusses the physical conditions of the Magellanic gas, presenting new constraints on the ionization level in both the low-ion and high-ion gas phases. In §5 we derive and discuss the total (neutral plus ionized) gas mass in the MSys. In §6 we discuss the accretion rate of Magellanic gas onto the Galaxy. In §7 we briefly discuss the MSys in terms of intervening quasar absorption line systems. §8 summarizes the main results.

2. OBSERVATIONS AND DATA HANDLING

2.1. *Sample Selection*

We assembled our sample of 69 targets by identifying all AGN observed with the *HST*/COS spectrograph (Green et al. 2012) that met the following criteria:

(1) lie within 30° of the 21 cm emission from the Magellanic System, as defined by the H I contours of Morras et al. (2000);
(2) have COS data taken with the G130M grating;
(3) have data with a signal-to-noise ratio S/N$\gtrsim$5 per resolution element at 1250 Å;
(4) lie in directions where Magellanic absorption is at $|v_{\rm LSR}| > 100\,{\rm km\,s^{-1}}$ and is therefore unblended with Galactic ISM absorption.
(5) have data publicly available in the MAST archive as of October 2013;

Criterion (1) was adopted to provide an extended search area around the MSys. This region covers most of the Southern Galactic hemisphere. Criterion (2) was used since G130M data (covering ≈1150–1450 Å) are needed to cover the Si III λ1206 and Si II λ1193 lines, which are used in our ionization analysis. When G160M data are also available, covering ≈1405–1775 Å and hence the C IV $\lambda\lambda$1548, 1550 doublet, we include them, but we do not include sightlines with G160M data only, since they do not contain sufficient information for our ionization modeling procedure. Criterion (3) was adopted to ensure that each spectrum in the sample had sufficient quality to determine the presence or absence of Magellanic absorption in the UV metal lines, and that the apparent optical depth (AOD) method could be reliably applied (this method becomes inaccurate at S/N$\lesssim$5; Fox et al. 2005b). Criterion (4) was necessary to ensure that Magellanic absorption could be reliably separated from low-velocity absorption, and implied that targets in a small region of sky near the south Galactic pole were excluded from the search. Criterion (5) was used since the holdings of the MAST archive are constantly changing, and October 2013 represented the time when we chose to define our final sample.

Targets with available COS spectra that did not meet the above criteria were: HS 2154+2228, SDSS J004042.09–110957.7, LBQS 0107–0232, Mrk 1501, and NGC 7469, which have G160M data only (criterion 2); 2dFGRS_TGS394Z150, HE 0946–0500, LBQS 0052–0038, NGC 3256, and NGC 7552, which have S/N$\lesssim$5 (criterion 3); HE 0056–3622 and HE 2347–4342, which fall within the search area but were removed from the sample since in these directions MS absorption overlaps in velocity with Galactic ISM absorption (criterion 4).

Six of the targets were observed in 2012 under *HST* program 12604 (PI A. Fox), which specifically targeted MS directions. Three were observed under *HST* program 12204 (PI C. Thom), which targeted three closely-spaced directions near the compact HVC 224.0–83.4–197 (hereafter, the CHVC), which lies near the edge of the Stream (Sembach et al. 2002; Kumari et al. 2014). Three more were observed under *HST* program 12263 (PI T. Misawa), which targeted QSOs lying behind the MB. Six were observed under *HST* program 11692 (PI J. Howk), which targeted QSOs lying behind the halo of the LMC. The remainder were drawn from various programs, including the COS Science Team Guaranteed Time Observations (GTO) programs. The 69 spectra in the sample have a mean S/N per resolution element at 1200Å of 22 and a median of 18.

Basic information for all the targets in the sample is given in Table 1, and their distribution on the sky is shown in Figures 1a and 1b, where we include H I data from a Gaussian decomposition (N08) to the Leiden-Argentine-Bonn (LAB) survey (Kalberla et al. 2005). Figure 1a is color-coded by H I column density, and Figure 1b is color-coded by central LSR velocity of Magellanic absorption/emission. The maps are shown in the MS coordinate system defined by N08, in which the Stream bisects the equator, the LMC is at $L_{\rm MS}, B_{\rm MS}$=0°, 0°, the LA extends to positive $L_{\rm MS}$, and the Stream itself extends to negative $L_{\rm MS}$. This coordinate system is chosen to display the MSys without the projection effects that can distort its appearance when shown in Galactic coordinates.

2.2. HST/*COS Observations*

Table 1
Overview of Sightline Properties

ID[a]	Target	Region[b]	l (°)	b (°)	$L_{\rm MS}$[c] (°)	$B_{\rm MSys}$[c] (°)	Prog.[d]	$v_{\rm min}, v_{\rm max}$[e] (km s^{-1})	$\langle v_{\rm MS}\rangle$[f] (km s^{-1})	log N(H I)[g] (cm^{-2})
1	3C57	MS-Off	173.08	−67.26	−64.05	29.33	12038	−260,−160	···	<17.97
2	ESO265-G23	LA-Off	285.91	16.59	48.41	−9.20	12275	160, 300	230	<18.02
3	ESO267-G13	LA-Off	294.10	18.34	49.67	−17.11	12275	215, 360	290	<18.03
4	ESO31-G8	Bridge	290.33	−40.79	−9.31	−3.93	12263	150, 340	207	20.51
5	FAIRALL9	MS-On	295.07	−57.83	−26.56	−2.30	12604	120, 280	184	19.97
6	H1101-232	LA-Off	273.19	66.55	99.29	−4.77	12025	130, 230	160	<18.12
7	HE0153-4520	MS-Off	271.77	−67.98	−35.10	9.47	11541	150, 240	180	<18.40
8	HE0226-4110	MS-Off	253.94	−65.78	−34.34	16.74	11541	90, 245	195	<18.33
9	HE0238-1904	MS-Off	200.48	−63.63	−50.95	33.21	11541	−260,−160	···	<17.98
10	HE0429-5343	LMC-Off	262.08	−42.17	−9.19	17.18	12275	220, 325	275	<17.98
11	HE0435-5304	LMC-Off	261.02	−41.38	−8.45	18.04	11520	200, 380	280	<18.00
12	HE0439-5254	LMC-Off	260.69	−40.90	−7.98	18.34	11520	190, 340	280	<18.03
13	HE1003+0149	LA-Off	238.53	42.79	85.30	22.25	12593	200, 300	···	<18.36
14	HE1159-1338	LA-Off	285.11	47.24	79.51	−9.98	12275	110, 240	205	<17.99
15	HS0033+4300	MS-Off	120.03	−19.51	−129.21	22.74	12264	−400,−300	···	<18.42
16	IO-AND	MS-Off	120.80	−59.52	−86.78	17.66	11632	−410,−320	−370	<18.12
17	IRAS01003-2238	MS-Off	152.05	−84.58	−60.56	11.85	12533	−280,−160	···	<18.14
18	IRASF09539-0439	LA-On	243.33	37.00	77.89	22.18	12275	140, 240	160	18.89
19	IRASZ06229-6434	LMC-Off	274.31	−27.32	5.98	7.14	11692	200, 480	350	<18.13
20	LBQS0107-0233	MS-Off	134.03	−64.78	−79.13	21.32	11585	−330,−220	−260	<18.03
21	LBQS0107-0235	MS-Off	134.01	−64.80	−79.12	21.30	11585	−340,−150	−252	<18.02
22	LBQS1019+0147	LA-Off	242.16	46.07	86.67	18.28	11598	180, 280	···	<18.00
23	MRC2251-178	MS-Off	46.20	−61.33	−74.97	−15.18	12029	−350,−200	−260	<18.12
24	MRK1014	MS-Off	156.57	−57.94	−77.04	33.87	12569	−260,−180	···	<18.21
25	MRK1044	MS-Off	179.69	−60.48	−62.67	36.61	12212	−280,−130	−220	<18.06
26	MRK1502	MS-Off	123.75	−50.17	−95.87	21.78	12569	−340,−150	···	<18.19
27	MRK1513	MS-Off	63.69	−29.07	−109.97	−25.55	11524	−370,−170	−270	<18.28
28	MRK304	MS-Off	75.99	−34.22	−109.18	−13.91	12604	−400,−230	−350	<18.25
29	MRK335	MS-Off	108.76	−41.42	−106.41	12.64	11524	−400,−200	−340	<18.22
30	MS0117-2837	CHVC-Off	225.73	−83.65	−53.35	12.53	12204	−270,− 95	−120	<17.29
31	NGC3125	LA-Off	265.33	20.64	55.22	9.52	12172	150, 300	220	<18.47
32	NGC3783	LA-On	287.46	22.95	54.74	−11.13	12212	150, 300	240	20.10
33	NGC7714	MS-On	88.22	−55.56	−91.08	0.43	12604	−420,−190	−320	19.01
34	PG0003+158	MS-Off	107.32	−45.33	−102.43	11.52	12038	−430,−200	−315	<18.21
35	PG0026+129	MS-Off	114.64	−49.25	−98.04	16.19	12569	−330,−250	−280	<18.14
36	PG0044+030	MS-Off	120.80	−59.52	−86.78	17.66	12275	−350,−250	−275	<18.39
37	PG1011-040	LA-Off	246.50	40.75	80.16	18.23	11524	185, 235	208	<18.08
38	PG1049-005	LA-Off	252.24	49.88	86.72	10.54	12248	100, 280	200	<18.00
39	PG2349-014	MS-Off	91.66	−60.36	−86.73	3.16	12569	−370,−200	−294	<18.11
40	PHL1811	MS-Off	47.47	−44.82	−87.33	−27.05	12038	−380,−120	−200	<18.00
41	PHL2525	MS-On	80.68	−71.32	−75.04	1.52	12604	−280,−120	−256	18.27
42	PKS0202-76	Bridge	297.55	−40.05	−10.09	−9.42	12263	100, 360	150	20.05
43	PKS0439-433	LMC-Off	247.98	−41.38	−10.41	27.65	12536	200, 340	240	<18.03
44	PKS0552-640	LMC-On	273.47	−30.61	2.72	8.12	11692	200, 450	279	18.23
45	PKS0558-504	LMC-Off	257.96	−28.57	4.91	21.59	11692	220, 350	265	<18.07
46	PKS0637-75	LMC-On	286.37	−27.16	4.73	−3.51	11692	180, 400	240	19.28
47	PKS0932+02	LA-Off	232.39	36.84	83.08	29.58	11598	200, 300	···	<18.10
48	PKS1101-325	LA-Off	278.12	24.77	57.35	−2.79	12275	220, 320	···	<18.03
49	PKS1136-13	LA-Off	277.53	45.43	77.98	−4.66	12275	150, 220	180	<18.09
50	QSO1220-2859	CHVC-On	227.78	−82.93	−52.69	12.94	12204	−270,−120	−180	18.42
51	RBS144	MS-On	299.48	−65.84	−34.80	−1.50	12604	65, 210	92	20.17
52	RBS1795	MS-Off	355.18	−50.87	−47.56	−30.50	11541	100, 200	···	<18.08
53	RBS1892	MS-Off	345.90	−58.37	−44.75	−21.65	12604	160, 240	···	<18.02
54	RBS1897	MS-Off	338.51	−56.63	−40.11	−21.30	11686	100, 200	135	<18.29
55	RBS542	LMC-Off	266.99	−42.00	−8.76	13.56	11686	200, 400	300	<18.14
56	RBS563	LMC-On	272.25	−39.23	−5.94	9.56	11692	180, 400	220	19.22
57	RBS567	LMC-Off	261.22	−40.93	−7.96	17.94	11520	180, 360	220	<17.97
58	RXJ0209.5-0438	MS-Off	165.99	−60.81	−70.31	34.10	12264	−260,−160	−220	<18.23
59	RXJ0503.1-6634	LMC-On	277.18	−35.42	−2.36	5.41	11692	160, 375	285	20.98
60	SDSSJ001224.01-102226.5	MS-On	92.32	−70.89	−76.35	5.07	12248	−340,−140	−285	18.43
61	SDSSJ015530.02-085704.0	MS-Off	165.72	−66.34	−67.52	29.10	12248	−180,−100	−140	<18.07
62	SDSSJ021218.32-073719.8	MS-Off	171.15	−62.66	−66.72	33.41	12248	−260,−160	···	<18.12
63	SDSSJ094331.60+053131.0	LA-Off	230.04	40.41	87.57	28.71	11598	130, 200	160	<18.26
64	SDSSJ095915.60+050355.0	LA-On	233.37	43.48	88.38	24.84	12248	225, 325	289	19.09
65	SDSSJ225738.20+134045.0	MS-Off	85.28	−40.73	−105.05	−4.97	11598	−440,−260	−360	<18.17
66	SDSSJ234500.43-005936.0	MS-On	88.79	−59.39	−87.41	1.56	11598	−330,−190	−300	18.54
67	TONS210	CHVC-On	224.97	−83.16	−53.11	12.98	12204	−280,−140	−200	18.36
68	UGC12163	MS-Off	92.14	−25.34	−121.31	−2.49	12212	−460,−350	−420	<18.29
69	UKS0242-724	Bridge	292.17	−42.00	−10.82	−4.98	12263	100, 340	193	20.69

[a] Numerical ID of target, used to identify source on Figure 1.
[b] Region probed by target, either Stream (MS), Bridge, Leading Arm (LA), LMC Halo, or CHVC (near HVC 224.0–83.4–197). On and Off refer to directions with and without Magellanic H I 21 cm emission.
[c] Magellanic Longitude and Latitude, defined in Nidever et al. (2008). The LMC is at $L_{\rm MS}$, $B_{\rm MS}$=0°, 0°.
[d] *HST* Program ID of COS dataset.
[e] Minimum and maximum LSR velocities of Magellanic absorption, used for AOD integrations. Errors are ±10 km s^{-1} on each.
[f] Central Magellanic LSR velocity, defined by 21 cm emission when present, and by UV absorption otherwise. "..." denotes no UV detection.
[g] H I column density of Magellanic absorption measured from GASS, LAB, or Parkes data. Upper limits are 3σ, assuming a 40 km s^{-1} wide line.

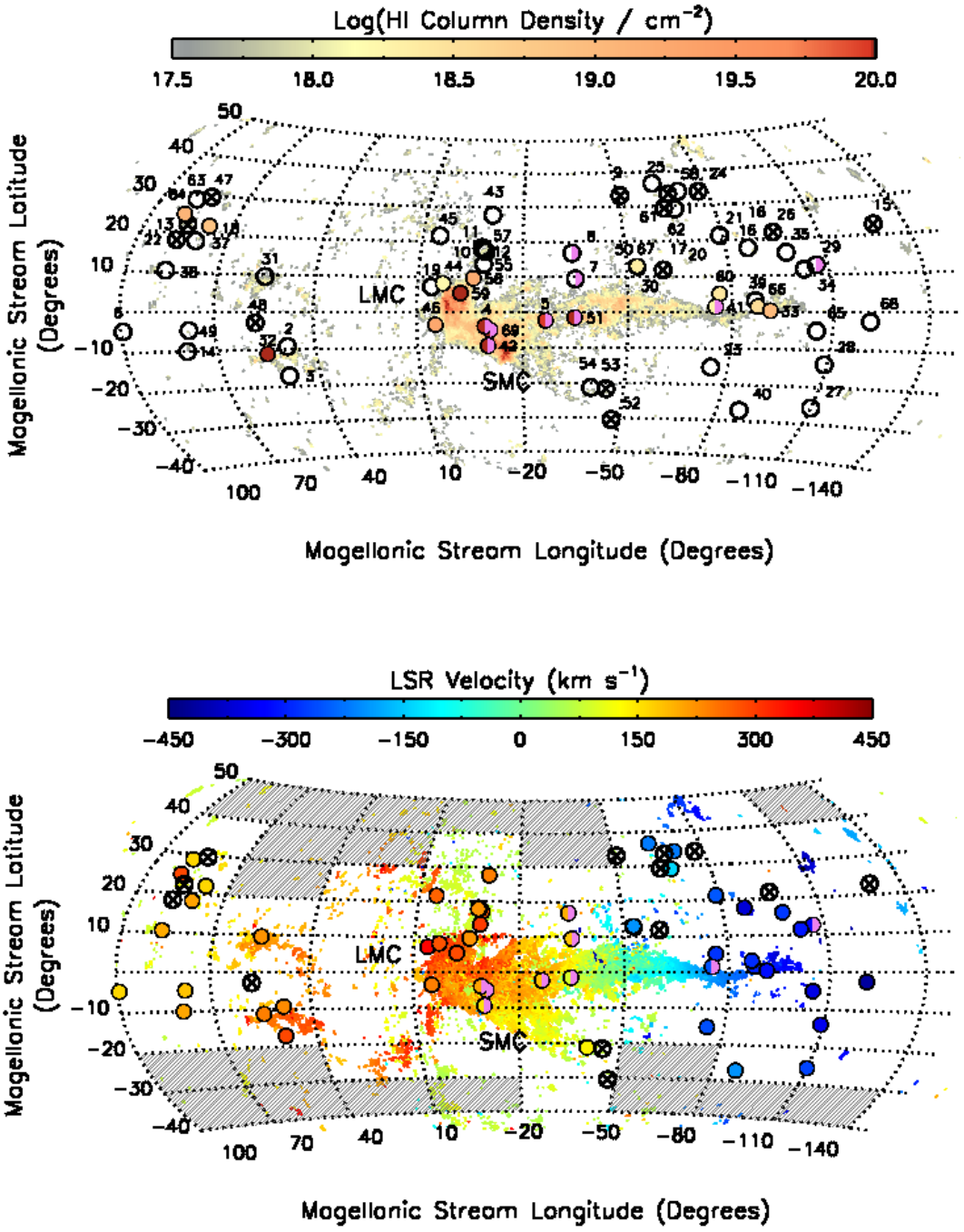

Figure 1. Maps of the Magellanic System comparing our 69 COS directions (circles) with a Gaussian decomposition (N08) of the H I 21 cm emission from the LAB survey (colored shading; Kalberla et al. 2005). The maps are plotted in the MS coordinate system of N08. **Top:** MSys map color-coded by H I column density. 56 out of 69 COS directions display Magellanic UV absorption; the non-detections are shown with crossed circles. Directions with WHAM data are shown half-shaded in pink. The numbers next to each sightline identify the targets in Table 1 and the appendix. **Bottom:** MSys map color-coded by central LSR velocity. The coloring of the circles shows the velocity of the UV absorption, whereas the coloring of the background shading shows the velocity of the 21 cm emission. The 21 cm velocity field is closely reflected in the UV absorption lines, even when moving from On-System to Off-System directions. The non-hatched regions show our adopted cross-section of Magellanic gas, used in our gas-mass and inflow-rate calculations.

Table 2
Apparent Column Densities and Ion Ratios in Magellanic Gas

Target	Region	log N(Si II) (cm^{-2})	log N(Si III) (cm^{-2})	log N(Si IV) (cm^{-2})	log N(C II) (cm^{-2})	log N(C IV) (cm^{-2})	log $\frac{\text{Si III}}{\text{Si II}}$	log $\frac{\text{Si IV}}{\text{Si II}}$	log $\frac{\text{C IV}}{\text{C II}}$
3C57	MS-Off	<12.97	<12.42	<12.71	13.98±0.04	<13.25	···	···	<−0.73
ESO265-G23	LA-Off	13.72±0.10	13.35±0.10	<13.37	···	···	−0.36±0.15	<−0.34	···
ESO267-G13	LA-Off	13.22±0.20	13.20±0.20	<13.58	<14.40	···	−0.03±0.29	< 0.36	···
ESO31-G8	Bridge	14.63±0.10	>13.87	13.47±0.13	···	13.89±0.14	>−0.76	−1.17±0.17	···
FAIRALL9	MS-On	14.53±0.02	13.54±0.01	13.02±0.09	>14.88	13.49±0.06	−0.98±0.05	−1.51±0.10	<−1.39
H1101-232	LA-Off	13.84±0.04	>13.44	<13.46	>14.51	<13.64	>−0.41	<−0.38	<−0.87
HE0153-4520	MS-Off	12.98±0.09	12.83±0.04	<12.72	13.82±0.04	<13.25	−0.14±0.11	<−0.26	<−0.58
HE0226-4110	MS-Off	13.12±0.05	13.26±0.01	13.03±0.07	14.28±0.01	13.88±0.02	0.15±0.07	−0.08±0.10	− 0.39±0.06
HE0238-1904	MS-Off	<12.70	<12.28	<12.91	<13.24	<13.09	···	···	···
HE0429-5343	LMC-Off	13.42±0.13	13.24±0.09	<13.34	<14.25	···	−0.17±0.17	<−0.07	···
HE0435-5304	LMC-Off	13.79±0.06	>13.67	13.22±0.12	···	13.62±0.16	>−0.12	−0.58±0.14	···
HE0439-5254	LMC-Off	13.62±0.03	13.36±0.04	<13.77	<14.27	13.57±0.13	−0.27±0.07	< 0.15	>−0.71
HE1003+0149	LA-Off	<13.17	<12.87	<12.92	<13.88	<13.31	···	···	···
HE1159-1338	LA-Off	13.38±0.12	13.31±0.07	<13.16	···	···	−0.07±0.14	<−0.22	···
HS0033+4300	MS-Off	<13.68	12.48±0.20	···	13.49±0.42	···	>−1.19	···	···
IO-AND	MS-Off	12.92±0.08	12.85±0.04	<12.56	13.96±0.03	<13.12	−0.06±0.10	<−0.36	<−0.85
IRAS01003-2238	MS-Off	···	<13.01	<13.53	<14.18	···	···	···	···
IRASF09539-0439	LA-On	>14.05	>13.55	12.86±0.10	>14.86	···	···	<−1.19	···
IRASZ06229-6434	LMC-Off	14.28±0.01	>13.92	13.29±0.05	···	<13.36	>−0.36	−1.00±0.07	···
LBQS0107-0233	MS-Off	12.33±0.20	12.70±0.12	<13.11	<13.59	13.29±0.17	0.37±0.24	< 0.79	>−0.30
LBQS0107-0235	MS-Off	13.05±0.19	12.87±0.10	<13.14	13.67±0.15	13.71±0.07	−0.18±0.22	< 0.10	0.05±0.17
LBQS1019+0147	LA-Off	<13.38	<12.85	<13.15	<14.17	<13.72	···	···	···
MRC2251-178	MS-Off	<12.96	12.99±0.03	13.04±0.06	13.29±0.12	13.71±0.04	> 0.03	> 0.08	0.42±0.13
MRK1014	MS-Off	<12.87	<12.39	<12.99	<13.53	···	···	···	···
MRK1044	MS-Off	<12.96	12.73±0.07	<12.97	13.58±0.11	<13.43	>−0.24	···	<−0.15
MRK1502	MS-Off	<13.30	<13.02	<13.36	<13.85	···	···	···	···
MRK1513	MS-Off	<12.91	13.00±0.04	12.95±0.09	13.48±0.10	14.04±0.04	> 0.09	> 0.04	0.56±0.12
MRK304	MS-Off	<13.03	13.26±0.03	12.91±0.10	13.70±0.06	13.85±0.05	> 0.23	>−0.12	0.15±0.10
MRK335	MS-Off	<13.09	12.83±0.05	<12.90	<13.42	13.62±0.06	>−0.26	···	> 0.20
MS0117-2837	CHVC-Off	13.21±0.08	13.39±0.03	13.05±0.08	14.11±0.04	13.71±0.06	0.18±0.10	−0.16±0.12	− 0.40±0.08
NGC3125	LA-Off	13.32±0.08	13.23±0.19	<13.34	<14.43	···	−0.09±0.21	< 0.02	···
NGC3783	LA-On	13.86±0.02	13.02±0.04	<12.86	···	<13.24	−0.84±0.07	<−1.01	···
NGC7714	MS-On	13.65±0.11	13.69±0.10	13.51±0.11	14.46±0.10	13.93±0.12	0.04±0.16	−0.14±0.16	− 0.53±0.16
PG0003+158	MS-Off	13.36±0.07	13.34±0.03	···	···	14.01±0.03	−0.02±0.09	···	···
PG0026+129	MS-Off	<12.95	12.71±0.09	<12.68	<13.64	···	>−0.24	···	···
PG0044+030	MS-Off	13.31±0.19	12.93±0.19	<13.25	14.02±0.12	···	−0.37±0.28	<−0.05	···
PG1011-040	LA-Off	12.44±0.08	12.57±0.06	<12.74	13.60±0.05	<13.14	0.13±0.11	< 0.30	<−0.46
PG1049-005	LA-Off	13.88±0.07	13.51±0.07	<13.22	14.67±0.06	13.59±0.16	−0.37±0.11	<−0.66	− 1.08±0.18
PG2349-014	MS-Off	13.35±0.07	>13.73	13.44±0.04	14.44±0.03	···	> 0.37	0.09±0.10	···
PHL1811	MS-Off	13.37±0.04	13.60±0.01	13.46±0.03	14.29±0.02	14.30±0.02	0.23±0.07	0.09±0.07	0.02±0.06
PHL2525	MS-On	13.38±0.07	>13.70	13.19±0.09	14.38±0.03	14.01±0.05	> 0.32	−0.19±0.12	− 0.37±0.08
PKS0202-76	Bridge	14.60±0.07	···	13.18±0.24	>15.23	13.70±0.20	···	−1.42±0.26	<−1.53
PKS0439-433	LMC-Off	14.06±0.03	13.29±0.03	13.16±0.07	<13.98	···	−0.77±0.07	−0.89±0.09	···
PKS0552-640	LMC-On	13.98±0.03	>13.86	<13.10	···	13.83±0.04	>−0.12	<−0.88	···
PKS0558-504	LMC-Off	12.82±0.20	12.68±0.10	<13.23	<14.06	13.24±0.24	−0.15±0.23	< 0.41	>−0.82
PKS0637-75	LMC-On	14.24±0.03	13.82±0.03	<13.31	···	13.84±0.05	−0.42±0.06	<−0.93	···
PKS0932+02	LA-Off	<13.60	<13.08	<13.43	<14.21	<13.91	···	···	···
PKS1101-325	LA-Off	<13.18	<12.76	<12.81	<14.20	···	···	···	···
PKS1136-13	LA-Off	12.57±0.20	12.36±0.17	<12.77	13.62±0.09	···	−0.21±0.27	< 0.19	···
QSO1220-2859	CHVC-On	13.46±0.06	13.32±0.04	13.08±0.10	<14.39	13.66±0.11	−0.15±0.09	−0.38±0.13	>−0.74
RBS144	MS-On	13.86±0.03	>13.56	<13.10	>14.60	<13.51	>−0.30	<−0.76	<−1.08
RBS1795	MS-Off	<12.50	<12.51	<12.60	<13.29	<13.49	···	···	···
RBS1892	MS-Off	<12.53	<12.37	<12.80	<13.57	<13.26	···	···	···
RBS1897	MS-Off	12.60±0.12	12.57±0.04	<12.48	<13.00	<13.20	−0.03±0.14	<−0.12	···
RBS542	LMC-Off	13.29±0.02	13.46±0.00	12.97±0.08	···	13.53±0.02	0.17±0.05	−0.32±0.10	···
RBS563	LMC-On	14.53±0.07	>14.08	13.85±0.04	···	14.36±0.07	>−0.45	−0.68±0.10	···
RBS567	LMC-Off	13.17±0.12	13.38±0.03	<13.13	<14.26	<13.56	0.22±0.13	<−0.03	···
RXJ0209.5-0438	MS-Off	<13.43	···	12.86±0.14	14.03±0.05	13.30±0.12	···	>−0.57	− 0.73±0.14
RXJ0503.1-6634	LMC-On	>14.82	>14.14	13.38±0.11	···	13.67±0.14	···	<−1.45	···
SDSSJ0012-1022	MS-On	13.58±0.16	>13.79	13.50±0.15	14.53±0.17	14.02±0.13	> 0.21	−0.08±0.23	− 0.51±0.22
SDSSJ0155-0857	MS-Off	13.44±0.08	13.10±0.05	<13.08	14.13±0.09	<13.61	−0.35±0.11	<−0.36	<−0.52
SDSSJ0212-0737	MS-Off	<13.19	<12.61	<13.11	<13.79	<13.60	···	···	···
SDSSJ0943+0531	LA-Off	12.81±0.20	12.71±0.20	<13.34	13.55±0.30	<13.77	−0.11±0.29	< 0.53	< 0.22
SDSSJ0959+0504	LA-On	<13.05	12.46±0.15	<12.99	<13.99	13.52±0.13	>−0.58	···	>−0.47
SDSSJ2257+1340	MS-Off	13.61±0.16	>13.63	13.76±0.09	14.36±0.10	14.25±0.09	> 0.02	0.15±0.19	− 0.11±0.14
SDSSJ2345-0059	MS-On	13.75±0.11	13.52±0.20	13.41±0.12	14.38±0.11	>13.87	−0.23±0.23	−0.34±0.17	>−0.51
TONS210	CHVC-On	13.47±0.03	13.40±0.01	13.02±0.05	14.28±0.01	13.79±0.03	−0.08±0.06	−0.45±0.07	− 0.49±0.06
UGC12163	MS-Off	<13.47	13.24±0.10	13.24±0.15	14.02±0.10	13.58±0.17	>−0.24	>−0.24	− 0.44±0.21
UKS0242-724	Bridge	14.65±0.06	>14.02	13.46±0.10	>15.08	13.86±0.09	>−0.63	−1.19±0.12	<−1.22

Note. — All measurements of apparent column densities are made in the LSR velocity intervals given in Table 1. Upper limits are 3σ and are based on non-detections. Lower limits are 1σ and indicate saturated lines. C II column densities are given as upper limits in sightlines where Magellanic absorption in C II λ1334 blends with Galactic C II* λ1335 absorption. No entry (...) indicates no data coverage. Full names of SDSS quasars are given in Table 1.

For each direction in our survey, the raw COS spectra were downloaded from the MAST archive in the form of `x1d` fits files. Overlapping exposures were aligned in wavelength space by matching the centroids of low-ionization interstellar absorption lines, combined by calculating the total count rate in each pixel, and converted back to flux after co-addition. Errors were calculated in the coadded spectra by weighting by inverse variance. Each coadded spectrum was shifted to the LSR velocity scale using the centroid of the Galactic 21 cm emission in that direction from the LAB survey (Kalberla et al. 2005) as the reference point.

In addition, for six directions with Magellanic H I column densities high enough for O I λ1302 absorption to be detectable (RBS 144, PHL 2525, NGC 7714, QSO1220–2859, TON S210, and MS0117–2837), we performed an orbital night-only reduction of the COS data to remove the geocoronal airglow emission that contaminates this line. To do this, the spectra were extracted only using the time intervals when the Sun altitude as seen by the telescope was less than 20°. This criterion selects low-background intervals corresponding to the night-side portion of the *HST* orbit. The filtering of the night-only data was done using the timefilter module in the `costools` package, and the spectral re-extraction (for these data only) was done with the standard `CalCOS` pipeline.

The spectra were normalized around each absorption line of interest by fitting low-order polynomials to the local continuum, using intervals several 100 km s^{-1} wide on either side of the line. The spectra have a velocity resolution $R \approx$15 000–20 000 (instrumental FWHM≈15–20 km s^{-1}) depending on wavelength, and a native pixel size of 3 km s^{-1} (Holland et al. 2014). For analysis and display on the figures, the COS spectra were rebinned by either three or five native pixels, depending on the S/N ratio. Spectra with medium or good S/N (>10 per resolution element) were rebinned by three pixels, giving final spectra that are Nyquist sampled. Spectra with low S/N (<10 per resolution element) were rebinned by five pixels, giving final spectra with close to one pixel per resolution element.

2.2.1. *Identification of Magellanic UV Absorption*

For On-System (21 cm-bright) sightlines, the Magellanic velocity is known from the H I velocity field of the MSys (Putman et al. 2003a, N08). In these directions, the Magellanic velocity intervals $v_{\rm min}$ to $v_{\rm max}$ were identified from the H I profiles, by finding the pixels where the 21 cm emission rises above the baseline. For Off-System (21 cm-faint) sightlines, we searched the COS spectra for high-velocity ($|v_{\rm LSR}| > 100$ km s^{-1}) absorption components, and when such components were found, we compared their velocities with the Magellanic velocity *expected* for that sightline's Magellanic Longitude based on the 21 cm velocity field. When a match was found, the absorption component was labeled as Magellanic, and $v_{\rm min}$ and $v_{\rm max}$ were defined by the UV absorption. This approach assumes that the Magellanic velocity intervals do not vary over scales of $\lesssim$30° perpendicular to the Stream, which is reasonable since the velocity gradient is largest along the Stream, not tangential to it (Putman et al. 2003a, N08). This can be seen in Figure 1b: the H I fragments to the North and South of the body of the MS reflect the velocity field of the MS itself.

The MSys map color-coded by central velocity (Figure 1b) illustrates how we can be confident that the high-velocity absorption features analyzed in this paper are Magellanic in origin. Notice the close correspondence in color between the velocity field of the 21 cm emission (background shading) and the UV absorption (colored circles) in the On-System directions. Also note that as one moves to the North and South (in $B_{\rm MS}$) from the Stream, the velocity field of the absorbers matches the velocity along the axis of the Stream. Finally, notice the correspondence in color between the 21 cm emission and the UV absorption in the LA sightlines. *In summary, the UV absorption-line detections kinematically trace the MSys H I velocity field, even at impact parameters of up to 30° from directions where 21 cm emission is detected.*

2.2.2. *Measurement of Magellanic UV Absorption*

Measurements of the apparent column density of each absorbing ion in the COS data were made using the AOD technique of Savage & Sembach (1991) and are given in Table 2. The AOD in each pixel is given by $\tau_a(v)$=ln $[F_c(v)/F(v)]$, where $F_c(v)$ is the continuum level and $F(v)$ is the flux in that pixel. The apparent column density per pixel is defined by:

$$N_a(v) = \frac{m_e c}{\pi e^2}\frac{\tau_a(v)}{f\lambda} = 3.768{\times}10^{14}\frac{\tau_a(v)}{f\lambda}{\rm cm}^{-2}({\rm km\,s}^{-1})^{-1}, \quad (1)$$

where f is the transition oscillator strength and λ is the rest wavelength in Angstroms. The apparent column density in the line is obtained by integrating over the line profile, $N_a = \int_{v_{\rm min}}^{v_{\rm max}} N_a(v){\rm d}v$. In On-System directions, the same $v_{\rm min}$ and $v_{\rm max}$ values were used for the UV and 21 cm measurements; in Off-System directions, $v_{\rm min}$ and $v_{\rm max}$ were defined by the UV data only.

The AOD technique returns accurate estimates of the true column density of a given species provided the absorption-line profiles are resolved and unsaturated. While resolved saturation is readily apparent, unresolved saturation can be difficult to detect. When resolved saturation is seen in a given line, which we define as occurring whenever the normalized flux falls below 0.1 anywhere within the line profile, we treat the apparent column density of that ion as a lower limit in the analysis. Table 2 also presents the apparent-column-density ratios between several key ions; these ratios are used in the ionization modeling (§4.1).

2.3. *21 cm H I spectra*

We use publicly available 21 cm H I spectra from the LAB survey (Kalberla et al. 2005) and the Galactic All-Sky Survey (GASS; McClure-Griffiths et al. 2009; Kalberla et al. 2010) to derive H I column densities (or upper limits) in each Magellanic sightline. When both LAB and GASS data are available (which is true for sightlines with southern declinations), we use the GASS data because of their smaller beam size. In the case of the three sightlines labeled CHVC in Table 1, we instead use additional data obtained from the Parkes radio telescope. The LAB data have 1.3 km s^{-1} velocity resolution and 30–36′ angular resolution, the GASS data

have $0.8\,\mathrm{km\,s^{-1}}$ velocity resolution and $14.4'$ angular resolution, and the additional Parkes data have $0.4\,\mathrm{km\,s^{-1}}$ velocity resolution and $14.4'$ angular resolution. For both the LAB and the GASS data we adopt the closest pointing to each target direction, whereas the additional Parkes data were taken precisely along the three CHVC sightlines. The Magellanic H I columns were determined by integrating the 21 cm profiles using the equation:

$$N(\mathrm{H\,I}) = 1.823 \times 10^{18} \mathrm{cm^{-2}} \int_{v_{\mathrm{min}}}^{v_{\mathrm{max}}} T_B \, \mathrm{d}v, \qquad (2)$$

where T_B is the brightness temperature in K and the line is assumed to be optically thin. In Off-System directions, the 21 cm non-detections are used to place 3σ upper limits on the Magellanic H I column, assuming a line width of $40\,\mathrm{km\,s^{-1}}$.

2.4. *WHAM Hα emission-line spectra*

WHAM measurements of the Hα emission in a one-degree beam surrounding nine of our sample directions (six MS directions and three MB directions) were taken in 2011 and 2012. The MS and MB observations are described in detail in Barger et al. (2014) and Barger et al. (2013), respectively. WHAM (Haffner et al. 2003) is a dual-étalon Fabry-Perot spectrometer with a velocity resolution of $12\,\mathrm{km\,s^{-1}}$ (FWHM). The bandpass was tuned to $\pm 100\,\mathrm{km\,s^{-1}}$ around the central MS velocity in each sightline. The Hα profiles are presented in the form of intensity in milli-Rayleighs (mR) against LSR velocity, where 1 Rayleigh $= 10^6/4\pi$ photons $\mathrm{s^{-1}\,cm^{-2}\,sr^{-1}}$, which is $\approx 10^{-6}\,\mathrm{erg\,s^{-1}\,cm^{-2}\,sr^{-1}}$ at Hα.

3. OVERVIEW OF MAGELLANIC ABSORPTION

To illustrate the quality and nature of the data analyzed in this paper, in Figure 2 we present the COS absorption-line profiles of either S II λ1253 or Si III λ1206 and the H I 21 cm emission profiles for six sightlines selected to represent the various components of the MSys. The Fairall 9 spectrum shows multiple-component UV absorption from the MS at positive velocities with clear accompanying 21 cm emission (see Paper II). Toward Mrk 1513, strong negative-velocity UV absorption is observed from the MS *without* accompanying 21 cm emission, defining this as an Off-Stream direction. The 3C57 spectrum shows no Magellanic UV absorption, even in the highly sensitive Si III λ1206 line. Toward B0242–0724, multiple-component UV absorption from the MB is observed at positive velocities with a profile closely following the 21 cm emission. The NGC 3783 spectrum displays multiple-component positive-velocity UV absorption from the LA, with strong 21 cm component at the same velocity. The TON S210 spectrum shows strong UV absorption and 21 cm emission at $-205\,\mathrm{km\,s^{-1}}$ from the CHVC (Sembach et al. 2002; Richter et al. 2009; Kumari et al. 2014).

A larger set of absorption-line profiles for each sightline in our sample is shown in the appendix, together with the H I 21 cm emission profile. The default UV lines included are C II λ1334, Si II λ1193, Si III λ1206, Si IV λ1393, and C IV λ1548. These lines were chosen because they are among the strongest available indicators of low-ion (C II and Si II), intermediate-ion (Si III), and high-ion (C IV, Si IV) absorption from the MSys. Si II λ1193 is used instead of the stronger line Si II λ1260, because in directions where MSys absorption is at negative LSR velocities, MSys absorption in Si II λ1260 is blended with Galactic ISM absorption in S II λ1259. However, in directions where MSys absorption is at positive LSR velocities, we use Si II λ1260 when it gives a better indication of the Si II profile. In cases where the default lines are blended or saturated, we use C IV λ1550 instead of C IV λ1548, Si IV λ1402 instead of Si IV λ1393, and Si II λ1526 instead of Si II λ1193. When MSys absorption in C II λ1334 is blended with Galactic ISM absorption in C II* λ1335 (which occurs when the MSys absorption is near $v_{\mathrm{LSR}}{=}{+}260\,\mathrm{km\,s^{-1}}$), only an upper limit on the MSys C II column density can be derived, unless the absorption is saturated, in which case no limit on N(C II) can be made.

In a substantial fraction of sightlines, the Magellanic absorption consists of multiple components (see Figure 2, top-left panel). This indicates that the gas is clustered in velocity and hence is likely to be clustered spatially as well. In the extreme case of Fairall 9, seven components are seen in high-resolution VLT/UVES data of Ca II (Paper II). In our analysis, we present the *integrated* column densities, rather than component-by-component column densities, and our ionization modeling treats the Magellanic gas in each direction as arising in a single cloud. This is mainly because the COS spectral resolution is not high enough to fully resolve the cool-gas component structure, and our UVES observations only cover a subset of 13 sightlines (Paper I, Paper II).

3.1. *Detection Rate of Magellanic Absorption*

Of the 69 sightlines in our *HST*/COS sample, 56 (81%) show a Magellanic detection, which we define as significant absorption (3σ) at Magellanic velocities in a UV metal line. We refer the reader back to Figure 1b for an illustration of how the Magellanic velocities are identified, and how the UV velocity field closely follows the 21 cm velocity field. The lines detected vary between absorbers (see the appendix), but almost always include Si III λ1206, the most sensitive UV tracer of ionized gas available, and C II λ1334. Si II λ1260 or Si II λ1193 are often detected.

Given that we selected sightlines lying within 30° of the H I emission, and that the H I cross-section of the MSys $A(\mathrm{H\,I})_{\mathrm{MS}}$ is well known, we can use our UV detection rate to estimate the total cross-section of the MSys. $A(\mathrm{H\,I})_{\mathrm{MS}}$ is 2 701 square degrees down to a limiting column density $N(\mathrm{H\,I}){=}1{\times}10^{18}\,\mathrm{cm^{-2}}$ (Nidever et al. 2010). By finding the area on the sky in which Magellanic UV absorption is detected (determined by summing the area of the non-shaded grid cells in Figure 1b), and multipling by the covering fraction of 81%, the total cross-section of the MSys is ≈11 000 square degrees, of which ≈three-quarters is only seen in UV absorption. *The MSys therefore covers approximately one quarter of the entire sky of 41 253 square degrees.*

There is no clear break in the detection rate at impact parameters of 30° from the Magellanic H I contours, so it is possible that the true cross section is even higher, but we notice that non-detections are more likely to be found at at high impact parameter. The UV detection rate can be broken down by region: among the MB, CHVC, and

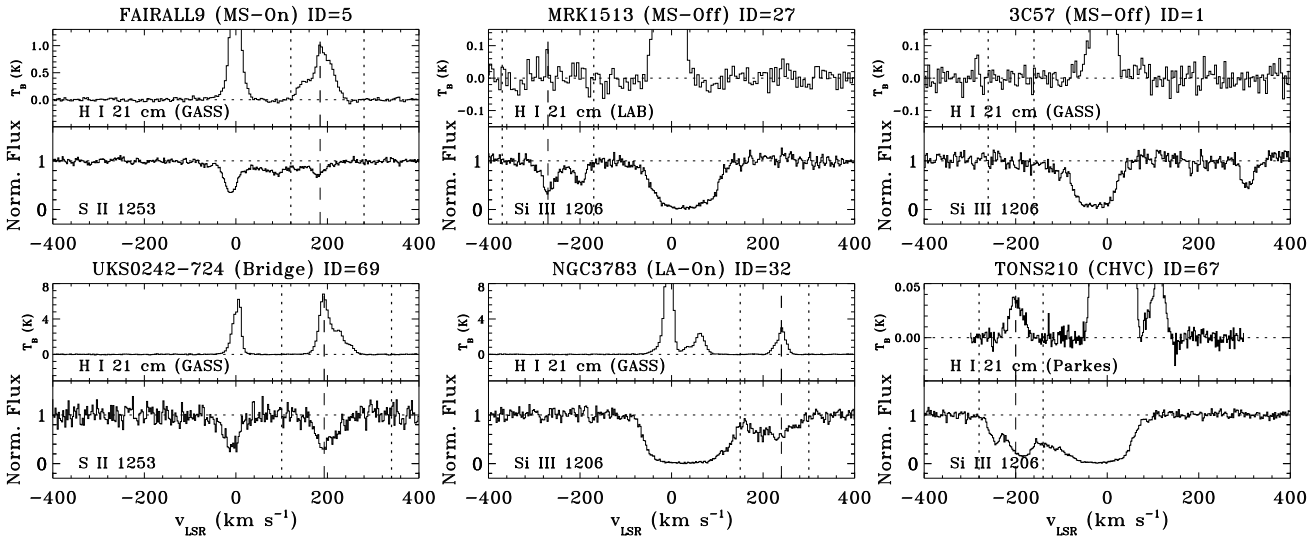

Figure 2. Example of COS absorption-line and 21 cm profiles in six MSys directions. The chosen sightlines sample different Magellanic regions: On-Stream (upper left), Off-Stream with a UV detection (upper middle), Off-Stream without a UV detection (upper right), Magellanic Bridge (lower left), Leading Arm (lower middle), and CHVC (lower right). The numerical ID in the title of each panel can be used to locate the sightline in Figure 1. The COS data are shown as normalized flux against LSR velocity, in each case showing a line that is unsaturated at Magellanic velocities. The 21 cm profiles are shown as brightness temperature against LSR velocity and are taken from the LAB survey, the GASS survey, or the Parkes telescope. Dashed vertical lines show the central Magellanic velocity in each direction, and dotted lines show the velocity integration range. Note how the MS velocities can be highly positive (as toward Fairall 9) or highly negative (as toward Mrk 1513), due to the large LSR velocity gradient along the Stream.

LMC halo sightlines, the detection rate is 100% (3/3 for the MB, 3/3 for the CHVC, and 12/12 for the LMC halo). Among the MS sightlines, the UV detection rate is 74% (26/35). Among the LA sightlines, the UV detection rate is 75% (12/16).

The UV non-detections are shown in Figure 1 as circles with black crosses, and they all lie in Off-System directions, as expected, since the H I column densities in the On-System directions are high enough that many UV metal lines are detectable in those sightlines. The MS non-detections tend to be found either to the North or South (in MS coordinates, as used in Figure 1) of the main body of the Stream. In particular, two clusters of non-detections are seen, one pair of sightlines (RBS 1795 and RBS 1892) near $L_{\rm MS}$=–40° $B_{\rm MS}$=–25°, and a group of four sightlines (3C57, HE0238–1904, SDSSJ021218.32–073719.8, and Mrk 1014) near $L_{\rm MS}$=–65°, $B_{\rm MS}$=+30°. Notably, three MS *detections* are also seen in this latter region, indicating the gas there is clumpy with a non-unity covering fraction.

We report four LA sightlines with UV non-detections (HE1003+0149, LBQS1019+0147, PKS0932+02, and PKS1101–325). High-velocity absorption between +100 and +200 km s^{-1} *is* detected in each of these directions, but these velocities are consistent with the foreground HVC complexes WA and WB (Wakker 2001), rather than the LA at $\gtrsim$200 km s^{-1}. While we cannot rule out an association between these complexes and the LA, we conservatively classify these sightlines as LA non-detections for the purposes of identifying Magellanic material. We also note that the sightlines toward IO–AND and HS0033+4300, which lie in the MS tip region, pass through the extended halo of M31, which has a systemic velocity of −300 km s^{-1} and a known velocity field (Chemin et al. 2009). For IO–AND, multiple HVC components are seen. We identify the −370 km s^{-1} component as the MS component, since this is the MS velocity in this part of the sky, and the absorption between −300 and −130 km s^{-1} as M31 components. Therefore we count this sightline as an MS detection. For HS0044+4300, high-velocity absorption is seen between −270 and −130 km s^{-1}. Since genuine MS absorption in this part of the sky would be closer to −400 km s^{-1}, these components could be entirely due to the M31 halo and its surrounding HVCs (Thilker et al. 2004), and so we classify this sightline as an MS non-detection.

3.2. *Kinematic Comparison of Neutral and Warm-Ionized Phases*

Our multi-wavelength dataset allows us to intercompare the profiles of emission or absorption from the various phases of the MSys in the same directions. In Figure 3, we present such a comparison for the nine sightlines with WHAM data covering Magellanic velocities. The plot compares the profiles of H I, Hα, and an unsaturated low-ionization UV metal-absorption line.

In five directions, namely the three MB sightlines PKS0202–76, UKS0242–724, and ESO 31–G08, and the high-column-density sightlines Fairall 9 and RBS 144, H I emission, Hα emission, and UV metal-line absorption are *all* detected at Magellanic velocities. These five directions are the most useful for assessing the connection in velocity between the various phases of the Magellanic gas. In each direction, Gaussian fits show that the Hα line widths are broader than the 21 cm H I line widths. This reflects two effects: (1) the ionized gas is warmer and/or more kinematically disturbed; (2) the lower WHAM spatial resolution causes multiple components to blend together within the 1° beam. For the three MB directions, the H I, Hα, and S II profiles are all centered within 10 km s^{-1} of each other. For the RBS 144 sightline, the H I, Hα, and S II profile centroids agree to within 1 km s^{-1}.

For the Fairall 9 direction, the profiles are more com-

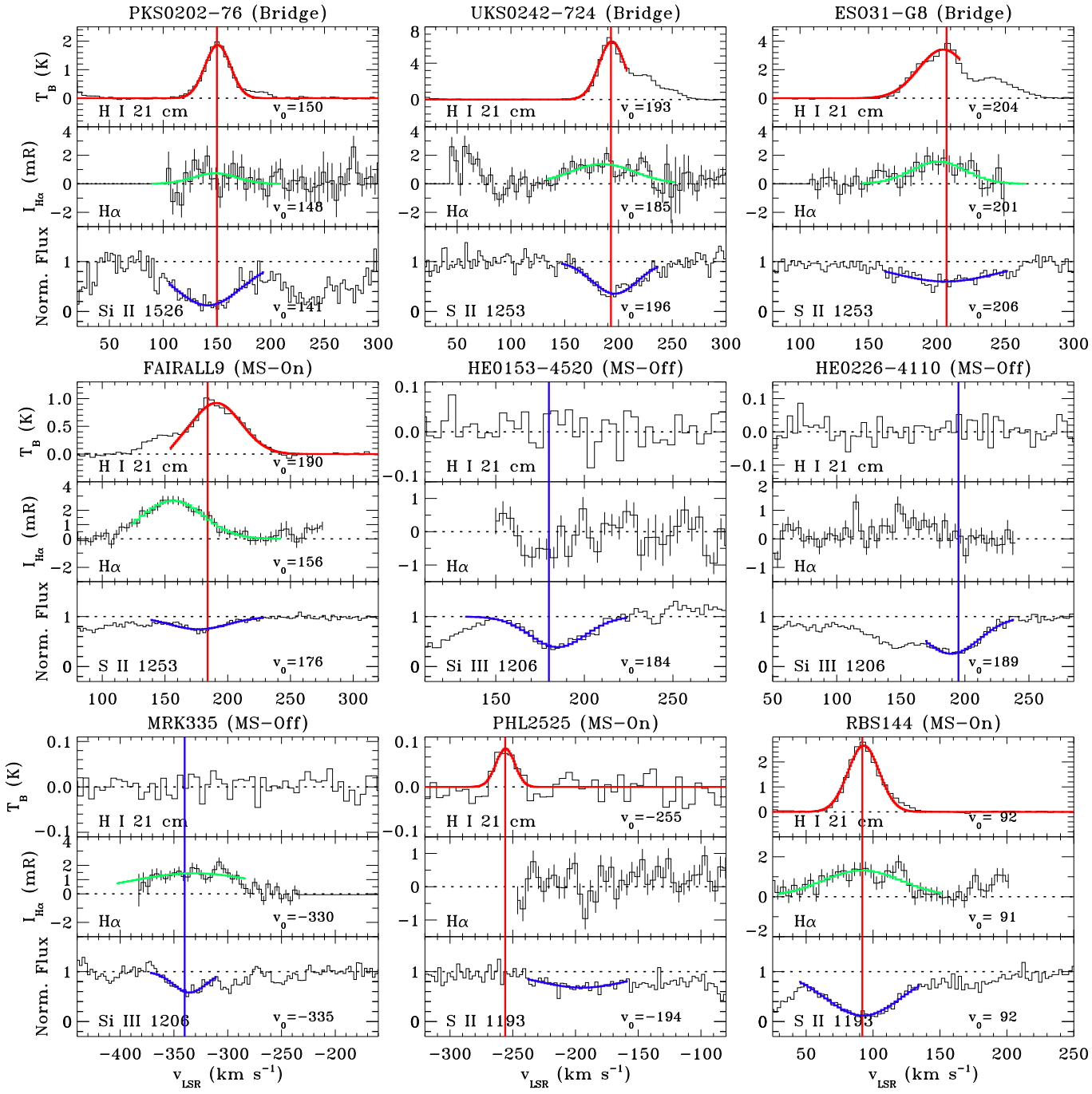

Figure 3. Comparison of 21 cm emission (GASS or LAB), Hα emission (WHAM), and UV metal-line absorption (COS) profiles in the nine sightlines with Hα data covering Magellanic velocities. In each panel, solid colored lines show Gaussian fits to the strongest component of emission or absorption. The velocity centroids of the fits are annotated on each panel, in units of km s^{-1}. The UV metal line shown in each panel is chosen to be unsaturated through the MS velocity interval. In each direction, a larger selection of UV absorption lines is shown in the appendix. The WHAM Hα intensities are in units of milli-Rayleighs (mR). Red vertical lines indicate the centroid of the Magellanic 21 cm emission; blue lines indicate the centroid of the Magellanic UV absorption.

plex. A significant offset ($34\,\mathrm{km\,s^{-1}}$) is seen between the strongest 21 cm component centered at $190\,\mathrm{km\,s^{-1}}$ and the Hα component centered at $156\,\mathrm{km\,s^{-1}}$, with the S II λ1253 centroid falling in-between at $178\,\mathrm{km\,s^{-1}}$ (see Barger et al. 2014). In Paper II, we reported C II* λ1335 absorption at $150\,\mathrm{km\,s^{-1}}$, *very close to the velocity where the Hα emission peaks*. This confirms the presence of ionized gas that is offset in velocity from the neutral gas. The strong Hα emission and C II* absorption indicate that the ionized gas has a relatively high electron density and recombination rate. This could indicate that the ionized gas exists in a boundary layer being compressed by ram pressure as the neutral core moves through an external medium. The presence of a dense neutral core in the Fairall 9 direction is known from observations of H_2 absorption (Richter et al. 2001) and Na I absorption (Paper II).

3.3. *Observed Ion Ratios*

In Table 2, we assess the ionization level in the Magellanic gas using three column-density ratios: Si III/Si II, Si IV/Si II, and C IV/C II. The Si III/Si II ratio probes the ionization level in the warm-ionized phase of the gas, because the two ions Si II and Si III generally show aligned absorption profiles and therefore co-exist in the same phase of gas. The Si IV/Si II and C IV/C II ratios probe the relative amounts of highly-ionized and warm-ionized gas, since Si IV and Si II (and C IV and C II) are thought to largely arise in different gaseous phases (see §4). These ratios are plotted against H I column density in the upper panels of Figure 4, and against MS Longitude $L_{\rm MS}$ in the lower panels.

In the upper panels, all three ratios (Si III/Si II, Si IV/Si II, and C IV/C II) show anti-correlations with N(H I), although the trends are complicated by the fact that many of the ion ratios and H I columns are limits, not measurements. Kendall-tau correlation tests show that the anti-correlations are significant at the 97.5% level for Si III/Si II (number of data points N=10), 96.4% level for Si IV/Si II (N=11), and 96.1% level for C IV/C II (N=6), where upper and lower limits were excluded from the analysis. For the C IV/C II ratio, including the limits strengthens the correlation, with all directions with $\log N(\mathrm{H\ I}) \gtrsim 20$ having $\log(\mathrm{C\ IV/C\ II}) < -1$, and all directions with $\log N(\mathrm{H\ I}) \lesssim 19$ having $\log(\mathrm{C\ IV/C\ II}) > -1.1$.

In the lower panels of Figure 4, a large scatter ($\approx$1 dex) is seen in each ion ratio at any $L_{\rm MS}$. Si IV/Si II (middle panel) and C IV/C II (right panel) each show a mild tendency for higher ratios at highly negative $L_{\rm MS}$, corresponding to MS directions far from the SMC and LMC, and lower ratios at less negative $L_{\rm MS}$. After excluding the upper and lower limits, Si IV/Si II and C IV/C II show weak anti-correlations with $L_{\rm MS}$ at the 92.3% (N=37) and 95.9% (N=43) confidence levels, respectively. The trends shown in Figures 4 reflect the declining H I column density along the body of the Stream (Nidever et al. 2010), following an approximately exponential decline from the Magellanic Clouds towards the tip.

4. PHYSICAL CONDITIONS IN THE MAGELLANIC GAS

In this section, we use ionization modeling to interpret the column densities of the UV ions in the MSys and to derive information on its physical conditions. These conditions are closely related to the System's interaction with the Galactic corona and with the incident ionizing radiation field.

We model the Magellanic gas as a two-phase plasma, with the H I, low ions (singly-ionized), and intermediate ions (doubly-ionized) existing in a photoionized (PI) phase, and the high ions (triply-ionized and above: C IV, Si IV, and O VI) existing in a separate, collisionally ionized (CI) phase. This approach is taken because photoionization models of the Stream, the Bridge, and other HVCs under-predict the observed high-ion column densities by orders of magnitude, particularly for C IV and O VI (Sembach et al. 2003; Tripp et al. 2003; Collins et al. 2004, 2005; Ganguly et al. 2005; Fox et al. 2005a; Misawa et al. 2009, F10). Further evidence for a two-phase structure is given by the different velocity-component structure seen in the low-ion and high-ion absorption profiles in many HVCs (Sembach et al. 1999; Tripp et al. 2003; Fox et al. 2004; Shull et al. 2011; Welsh et al. 2011; Tripp & Song 2012; Herenz et al. 2013), and by high-resolution observations of H I line widths in the MS (Nigra et al. 2012). The placement of the H I in the same phase as the low and intermediate ions, which is central to our modeling procedure, is supported by their similar ionization potentials and the similar kinematic structure of the H I and low-ion absorption profiles in directions where they have been compared (Fox et al. 2006; Zech et al. 2008). In our sample, the H I emission and UV absorption profiles are well-aligned for all On-System directions except PHL 2525 and J2345–0059.

4.1. *Low Ions: Cloudy Photoionization Modeling*

4.1.1. *Methodology*

We ran a set of photoionization models to reproduce the low-ion column densities observed in the MSys using the spectral synthesis code *Cloudy* (v08.00 Ferland et al. 1998). These models assume the gas exists in a uniform-density plane-parallel slab exposed to an incident radiation field (described below). We followed the same procedures described in F10 and Paper I, in which the key observational constraint on the models is the Si III/Si II ratio. For a given direction, the measured Si III/Si II ratio, the observed H I column density N(H I), the metallicity (Z/H), and the ionizing photon density n_γ in the incident radiation field are used as inputs to the models, with N(H I) acting as the stopping condition. A grid of models at varying gas density $n_{\rm H}$ was constructed for each direction on a 0.1 dex grid, and matching the observations solved for many physical parameters in the Magellanic gas, including the ionization parameter $U \equiv n_\gamma/n_{\rm H}$, the warm-ionized hydrogen column density N(H II), the hydrogen ionization fraction $x_{\rm H\ II}$=N(H II)/[N(H I)+N(H II)] the line-of-sight cloud size l=$N_{\rm H}/n_{\rm H}$, and the thermal pressure P/k=(1+$x_{\rm H\ II}$)$n_{\rm H}T$ (see Table 3).

The models are only applied to the 13 sightlines with measured H I columns and Si III/Si II ratios, because these two quantities are needed as inputs to *Cloudy*. If Si III and Si II are both undetected or both saturated, the ratio is undefined. The advantage of solving for the ionization parameter from the Si III/Si II ratio alone is that

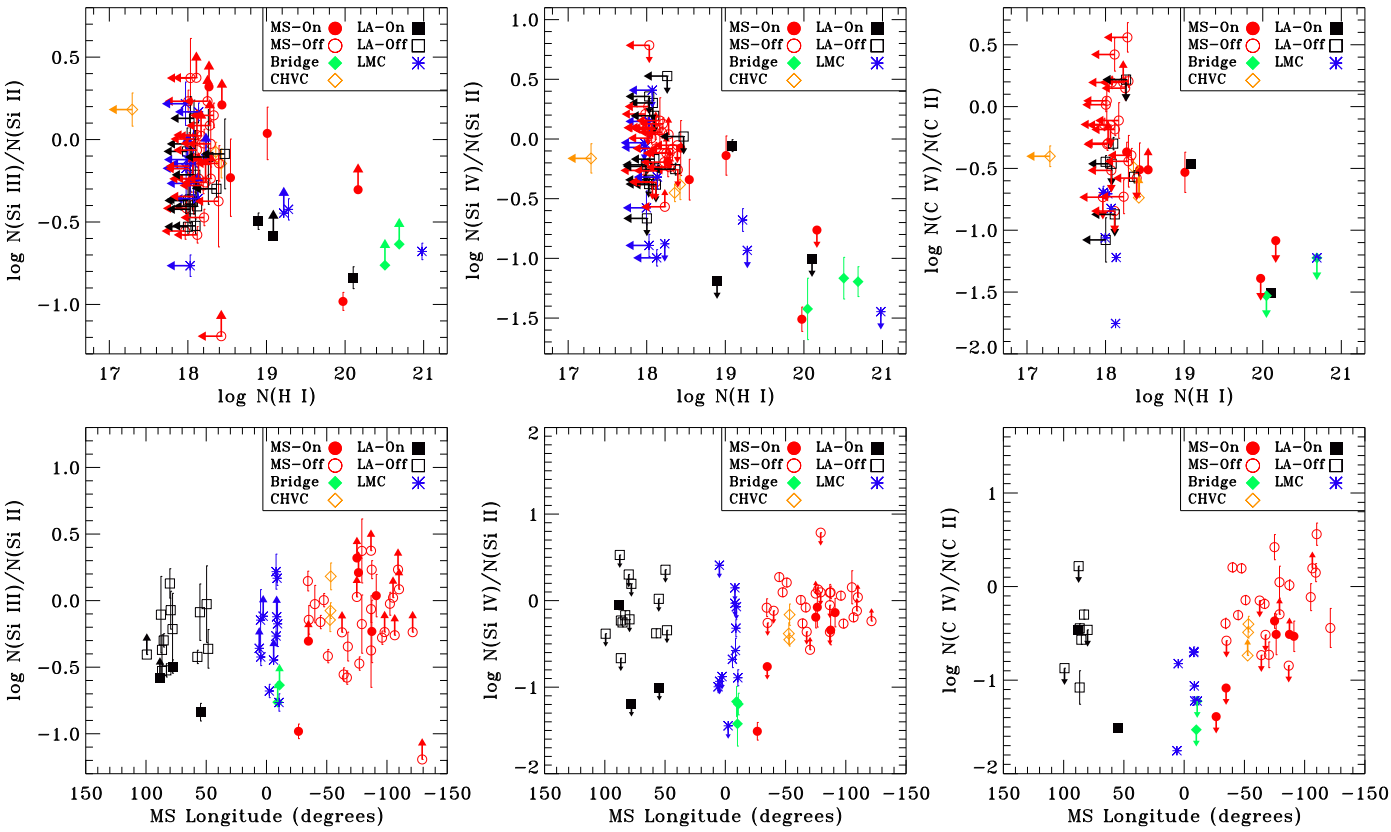

Figure 4. Upper panels: observed ion ratios against H I column density in Magellanic gas. The left, central, and right panels show the Si III/Si II, Si IV/Si II, and C IV/C II ratios, respectively. Upper and lower limits account for non-detections and saturation. The ratios were formed from apparent column densities measured in the same velocity integration range for each ion and for H I. **Lower panels:** observed ion ratios against MS Longitude $L_{\rm MS}$, as defined by N08. The LMC is at $L_{\rm MS}$=0°, the MS is at negative $L_{\rm MS}$, and the LA is at positive $L_{\rm MS}$. Note that $L_{\rm MS}$ here increases to the left, to match the format of the other figures.

it involves adjacent ionization states from the same element. This eliminates the possibility of non-solar abundance variations or differential dust depletions impacting the results.

The ionizing radiation field used in the models has two components:
(1) the Galactic radiation field taken from Fox et al. (2005a), which was based on Bland-Hawthorn & Maloney (1999, 2002), and which has an escape fraction of 1–2% averaged over solid angle and ≈6% normal to the disk;
(2) the ionizing radiation field emerging from the LMC and SMC, which is constrained by the Hα intensity of the Magellanic Bridge (Barger et al. 2013);
The combined field is shown in Figure 5, a contour plot showing the lines of constant hard (hydrogen-ionizing) and soft (non-hydrogen-ionizing) flux. Because this field is anisotropic, we extracted the hard and soft fluxes at the Magellanic Longitude $L_{\rm MS}$ of each sightline modeled, assuming an MS distance of 50 kpc. We then normalized the Galactic radiation field presented in Fox et al. (2005a) to these fluxes. This procedure gave the radiation field appropriate for a sightline at a given $L_{\rm MS}$, which was used as an input to the corresponding *Cloudy* model. For the six MS directions, we ran a second set of models appropriate for a MS distance of d=100 kpc, to see the effect of varying the distance. This was unnecessary for the LA, MB, and LMC Halo directions, since the Magellanic gas in those sightlines is clearly not at 100 kpc. We did not include the possibility of radiation from the vicinity of the super-massive black hole at the center of the Milky Way in a period of past Seyfert activity (Bland-Hawthorn et al. 2013), since that radiation was incident on the MSys ≈1–3 Myr ago, not the current epoch.

One potential source of systematic error in our modeling procedure is the beam-size mismatch between the radio data (finite beam) and UV data (infinitesimal beam). However, the magnitude of this effect on metallicity measurements along pencil-beam MS sightlines when using radio data with beam sizes of ≈14′ or less (such as GASS data) has been shown to be small ($\lesssim$0.15 dex; F10, Paper II).

4.1.2. *Results*

The results from our photoionization models are given in Table 3. The target direction is given in the first column, the next four columns define the model inputs specific to that direction, and the final six columns give the model outputs specifying the physical conditions in the Magellanic gas. Among all MSys sightlines, and considering the d=50 kpc models, the best-fit ionization parameters $\log U$ range from –3.8 to –3.1 with a median value of –3.5. The same range in $\log U$ is observed among MS sightlines only (i.e. not considering CHVC, MB, LMC Halo, or LA sightlines), in close agreement to values derived in earlier work on the Stream (F10, Paper I, Paper II). The median $\log U$=−3.5 corresponds to an av-

Table 3
Results of *Cloudy* Photoionization Simulations: Physical Conditions in Magellanic Gas

Target	Input				Output					
	$\log \frac{\text{Si III}}{\text{Si II}}$ [a]	$\log N$(H I) (cm^{-2})	[X/H] [b]	$\log n_\gamma$ [c] (cm^{-3})	$\log U$ [d]	$\log n_{\text{H}}$ [e] (cm^{-3})	$\log N$(H II) [f] (cm^{-2})	x_{HII} [g]	r_{los} [h] (kpc)	P/k [i] ($\text{cm}^{-3}\,\text{K}$)
Leading Arm										
NGC3783	−0.84	20.17	−0.6	−5.27	−3.5	−1.8	19.68	0.24	3.7	210
LMC Halo										
PKS0552-640	>−0.12	18.23	−1.0	−4.65	−3.8	−0.9	19.40	0.94	0.1	2740
PKS0637-75	−0.44	19.29	−1.0	−4.90	−3.8	−1.1	19.44	0.59	0.2	1260
Bridge										
UKS0242-724	>−0.63	20.69	−1.0	−5.07	−3.1	−2.0	20.15	0.22	19	130
ESO31-G8	>−0.76	20.51	−1.0	−4.97	−3.3	−1.7	19.94	0.21	6.2	260
CHVC										
QSO1220-2859	−0.11	18.42	−1.0	−5.41	−3.7	−1.7	19.52	0.93	0.6	380
TONS210	−0.08	18.36	−1.0	−5.41	−3.7	−1.7	19.52	0.94	0.6	380
Stream (50 kpc)										
FAIRALL9	−0.98	19.97	−0.3	−5.33	−3.5	−1.8	19.60	0.30	2.9	190
SDSSJ0012-1022	>+0.21	18.43	−1.0	−5.54	−3.4	−2.1	19.83	0.96	3.1	140
SDSSJ2345-0059	−0.23	18.54	−1.0	−5.67	−3.8	−1.9	19.42	0.88	0.7	250
NGC7714	+0.01	19.01	−1.0	−5.74	−3.5	−2.2	19.74	0.84	3.7	110
PHL2525	>+0.32	18.12	−1.0	−5.52	−3.3	−2.2	19.91	0.98	4.4	120
RBS144	>−0.32	20.17	−1.0	−5.40	−3.2	−2.2	20.04	0.43	13	89
Stream (100 kpc)										
FAIRALL9	−0.98	19.97	−0.3	−5.36	−3.5	−1.9	19.60	0.30	3.1	180
SDSSJ0012-1022	>+0.21	18.43	−1.0	−5.99	−3.4	−2.6	19.83	0.96	8.9	50
SDSSJ2345-0059	−0.23	18.54	−1.0	−6.17	−3.8	−2.4	19.42	0.88	2.3	80
NGC7714	+0.01	19.01	−1.0	−6.26	−3.5	−2.8	19.74	0.84	12	32
PHL2525	>+0.32	18.12	−1.0	−5.96	−3.3	−2.7	19.91	0.98	12	43
RBS144	>−0.32	20.17	−1.0	−5.60	−3.2	−2.4	20.04	0.43	20	56

Note. — Two sets of models are given for the MS directions, one assuming d=50 kpc and one assuming d=100 kpc. Full names for SDSS QSOs are given in Table 1.

[a] Logarithm of apparent-column-density ratio measured in LSR velocity interval given in Table 1.

[b] Metallicity of Magellanic gas, taken to be 0.1 solar (Lehner et al. 2008, Fox et al. 2010; Paper I) for all directions except Fairall 9 (0.5 solar; Gibson et al. 2000, Paper II) and NGC 3783 (0.25 solar; Sembach et al. 2001).

[c] Logarithm of ionizing photon density in radiation field. Value is variable since field is non-isotropic (see Figure 5).

[d] Logarithm of ionization parameter $U \equiv n_\gamma / n_{\text{H}}$.

[e] Logarithm of gas density.

[f] Logarithm of H II column density in the low-ion phase; this does not include the high-ion H II living with the C IV and Si IV.

[g] Ionization fraction x_{HII}=N(H II)/[N(H I)+N(H II)].

[h] Line-of-sight cloud size, r_{los}=$N_{\text{H}}/n_{\text{H}}$ where N_{H}=N(H I)+N(H II).

[i] Thermal pressure, P/k=(1+$x_{\text{H II}}$)$n_{\text{H}}T$ and T=10^4 K.

erage Magellanic gas density $\log(n_{\text{H}}/\text{cm}^{-3}) \approx -1.8$ given the calculated density of the ionizing radiation field. In turn, this implies line-of-sight cloud sizes for the Magellanic gas ranging from a few tenths of a kpc to several kpc (Table 3).

The hydrogen ionization level in the low-ion phase of the MSys depends closely on the H I column density, as expected; it ranges from ≈20% for the MB directions with $\log N(\text{H I}) \gtrsim 20$ to >80–90% for directions with $\log N(\text{H I}) \lesssim 19.5$. Since the low-$N$(H I) directions occupy a much larger cross-section than the high-N(H I) directions (§3.1), *the gas is predominantly ionized in most directions through the MSys*, and even the "low-ion" gas is predominantly ionized when $\log N(\text{H I}) < 20$. In terms of low-ion H II columns (warm H^+ columns), all six MS models have $\log N(\text{H II})$ in a fairly narrow range between 19.4 and 20.0, even though the H I columns vary by over two orders of magnitude. This finding allows us to use an average $\log N(\text{H II})$ for On-System directions when calculating the MSys mass (§5) and inflow rate onto the Galaxy (§6). The one LA direction modeled (NGC 3783) shows a similar H II column as the MS models.

The final six rows in Table 3 show the results from the MS models assuming a distance d=100 kpc. Here the ionizing photon density is lower than in the d=50 kpc case (Figure 5), although the degree by which it is lower depends on Magellanic Longitude, with sightlines close on the sky to the Magellanic Clouds (Fairall 9 and RBS 144) showing less reduction in flux than those farther away. As expected, the same best-fit ionization parameter is found for each sightline for the d=100 kpc models as for the d=50 kpc models (because the shape of the radiation field does not change). This in turn implies that the d=100 kpc MS models have lower gas density, lower thermal pressure, and larger line-of-sight cloud sizes. The H II columns show no dependence on distance, which is important for our mass calculation (Section 5).

The thermal pressure P/k for the six MS directions (considering both the d=50 kpc and d=100 kpc cases) lies in the range ≈30–250 cm^{-3} K. This can be compared with the thermal pressure exerted by the hot Galactic corona thought to confine the Stream. In the isothermal hot corona models of Sternberg et al. (2002), which have a plasma temperature of 2×10^6 K, the coronal pressure is ≈250 cm^{-3} K at 50 kpc, and ≈100 cm^{-3} K at 100 kpc, corresponding to a coronal density $\log(n_{\text{hot}}/\text{cm}^{-3}) = -3.9$ at 50 kpc and −4.3 at 100 kpc. Therefore, we find that if the Stream is at 50–100 kpc (as suspected by LMC/SMC orbital considerations), it would be close to pressure equilibrium with the hot corona.

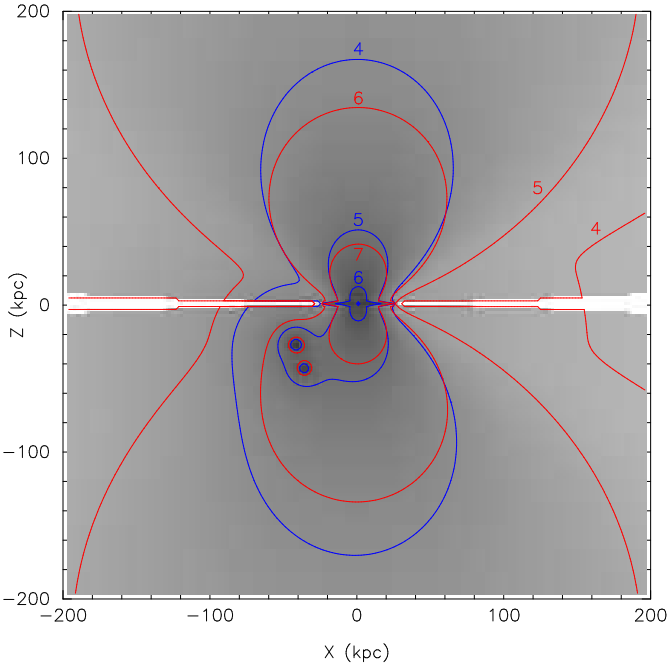

Figure 5. Galactic ionizing radiation field used in our *Cloudy* photoionization modeling, including contributions from the LMC and SMC. The plot shows a 400×400 kpc slice through the Galactic halo viewed from outside. The blue and red contours show the contours of constant hydrogen-ionizing flux ($E > 13.6$ eV) and non-hydrogen-ionizing flux ($E < 13.6$ eV), respectively. The numbers next to the contours give the logarithm of the flux in units of photons cm^{-2} s^{-1}. This model is an updated version of the radiation field presented in Bland-Hawthorn & Maloney (1999, 2002) and Fox et al. (2005a). The LMC and SMC contributions are normalized by the Hα intensity from the MB (Barger et al. 2013); they are important for the MB and LA ionization models but less important for the MS models. For comparison, the UV background at z=0 (not shown) has an ionizing flux of $\approx 10^4$ photons cm^{-2} s^{-1} (Haardt & Madau 2012).

4.2. *High Ions: Collisional Ionization Modeling*

C IV $\lambda\lambda$1548,1550 is the most highly-ionized doublet detected in the COS data, because N V $\lambda\lambda$1238,1242 is generally too weak to be detected in Magellanic gas and O VI $\lambda\lambda$1031,1037 falls below the bandpass of our COS observations. Therefore, we use C IV as the tracer of the highly-ionized phase of the MSys. C IV ions are created from C III with an energy of 47.9 eV and can be produced by either photoionization or collisional ionization. The C IV absorption profiles generally cover the same velocity interval as the low-ion absorption profiles, but often show important kinematic differences in their detailed component structure.

The highly-ionized hydrogen column traced by the C IV absorption in each direction is given by

$$N(\mathrm{H\ II})_{\mathrm{C\ IV}} = N(\mathrm{C\ IV})/[f(\mathrm{C\ IV})(\mathrm{C/H})_{\mathrm{MS}}], \qquad (3)$$

where the C IV ionization fraction $f(\mathrm{C\ IV}) \equiv N(\mathrm{C\ IV})/N(\mathrm{C})$ never rises above a maximum value 0.3 in either collisional ionization or photoionization (Sutherland & Dopita 1993; Gnat & Sternberg 2007; Oppenheimer & Schaye 2013). In collisional ionization equilibrium, C IV peaks in abundance at a temperature of 2.0×10^5 K, so the values of $N(\mathrm{H\ II})_{\mathrm{C\ IV}}$ we derive only represent the H$^+$ column existing at or below that temperature; they do not include any hotter plasma regions that may be present. With two exceptions (discussed below), the carbon abundance $(\mathrm{C/H})_{\mathrm{MS}}$ is taken to be $0.1(\mathrm{C/H})_{\odot}$, which assumes that the low-ion and high-ion phases of the Stream share the same metallicity of 0.1 solar (F10, Paper I). This assumption is valid if the high-ion phase evaporated out of the cool gas, which is believed to be the case for the MS as it interacts with the hot corona (Sembach et al. 2003, F10). The two sightlines where we adopt a higher carbon abundance are Fairall 9, where we use 0.5 solar (Paper II), and NGC 3783, where we use 0.25 solar (Sembach et al. 2001), because these are the directions where higher abundances have been measured. Our calculation also assumes that carbon atoms in the high-ion phase are undepleted onto dust grains, and ignores any deviation of the C/α ratio from solar. Because our adopted value of f(C IV) is an upper limit, the high-ion H II columns given by Equation (3) are lower limits.

5. TOTAL MASS OF MAGELLANIC GAS

In Figure 6, we combine the results from the ionization modeling (§4.1 and §4.2) to illustrate how the mass in the MSys is distributed between the atomic, warm-ionized, and highly-ionized phases. For each direction modeled, the plot shows the fraction of the total hydrogen column in each phase. The number of sightlines shown (13) is determined by the number of sightlines with 21 cm measurements of the Magellanic H I column (translating to directions with $N(\mathrm{H\ I}) \gtrsim 10^{18}$ cm^{-2}) and a Si III/Si II ratio. The height of the green and red bars relative to the blue bars indicates the dominant contribution of the ionized gas to the mass budget, particularly when considering that only sightlines with 21 cm H I measurements are included on this plot. If included, Off-System directions would be dominated by the green and red bars (low-ion and high-ion H II). Note that among the sightlines modeled, the MB directions (ESO31–G8 and UKS0242–724) show substantial H I fractions, as do the inner-Stream sightlines toward RBS 144 and Fairall 9. This is expected given the high H I columns in these directions. However, the MS sightlines (at negative MS Longitude) are dominated by low-ion H II. The LA sightlines (at positive MS Longitude) show a lower ionization level than the MS sightlines. Particularly interesting is that the single LA sightline modeled (NGC 3783) shows no C IV absorption. Only one out of sixteen LA sightlines shows C IV absorption (Table 2), hence the LA shows a much less developed high-ion phase than the MS.

The ionization fractions shown on Figure 6 can be used to estimate the total gas mass of the MSys. Among the 13 Magellanic directions modeled, the median value of $N(\mathrm{H\ II})_{\mathrm{total}}/N(\mathrm{H\ I})$ is 6.4, where $N(\mathrm{H\ II})_{\mathrm{total}} = N(\mathrm{H\ II})_{\mathrm{low}} + N(\mathrm{H\ II})_{\mathrm{C\ IV}}$. If we ignore the high-ion H II and just consider the low-ion H II, which is better constrained, the median value of $N(\mathrm{H\ II})_{\mathrm{low}}/N(\mathrm{H\ I})$ is 5.4, only slightly lower, indicating that the low-ion phase dominates the C IV phase in the mass budget of the MSys. However, our data has not constrained the mass of hotter plasma at $T \gtrsim 3\times10^5$ K in the MSys, which is seen in O VI absorption in both On-System and Off-System directions (Sembach et al. 2003).

To estimate the total gas mass (H I+H II) of the MSys M(MSys), we need to account for the H II mass in the directions with and without 21 cm emission, which we write as M(H II, on) and M(H II, off), respectively. Splitting

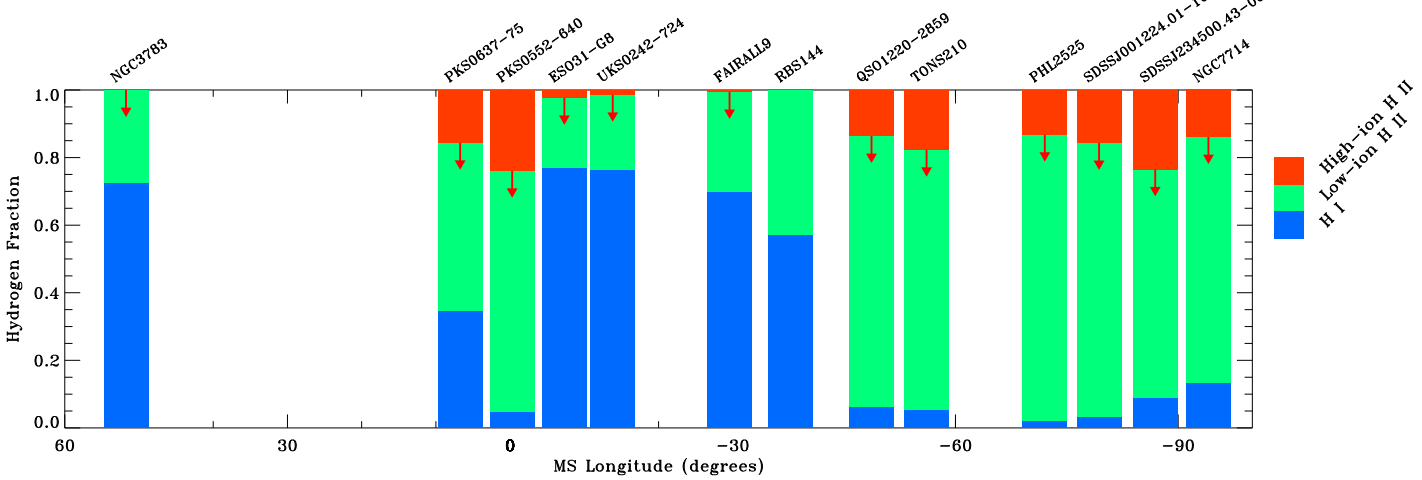

Figure 6. Hydrogen ionization breakdown in the Magellanic gas in each sightline where 21 cm emission is detected. The height of each bar indicates the fraction of the total hydrogen column density in the atomic (blue), warm-ionized (green), and highly-ionized (red) phase. The bars are presented in order of decreasing Magellanic Longitude, so LA directions are on the left, Bridge and LMC Halo directions are in the center, and Stream directions are on the right. The low-ion H II columns are derived from the photoionization models discussed in §4.1. The high-ion H II fractions are lower limits derived from the C IV observations (see §4.2) when C IV is detected.

up the calculation in this way is necessary to identify where most of the ionized gas mass resides, because of two competing effects: the H II columns are higher in the directions with high H I columns, but the H II cross-section is higher in the directions with low H I columns. M(MSys) can be written as a sum of three parts:

$$\mathrm{M(MSys)} = \mathrm{M(H\ I)} + \mathrm{M(H\ II, on)} + \mathrm{M(H\ II, off)}. \quad (4)$$

M(H I) in the MSys is known from 21 cm measurements to be $4.87{\times}10^8 (d/55\,\mathrm{kpc})^2\,\mathrm{M}_\odot$ (Brüns et al. 2005), summing over the MS, MB, and LA, and treating the "Interface region" as part of the MS.

M(H II, on) depends on the product of the cross-sectional area of the 21 cm-bright MSys and the average H II column density in those directions:

$$\mathrm{M(H\ II, on)} = m_\mathrm{H} A(\mathrm{H\ II, on}) \langle N(\mathrm{H\ II, on}) \rangle. \quad (5)$$

where m_H is the mass of a hydrogen atom, A(H II, on)=A(H I, on) by definition, and $\langle N(\mathrm{H\ II,\ on}) \rangle$ is the median H^+ column in the 21-cm bright directions. The angular cross-section of the MSys of 2 701 square degrees (N08) corresponds to A(H I, on)=$2.4{\times}10^{46}\,\mathrm{cm}^2 (d/55\,\mathrm{kpc}^2)$, where d is conservatively assumed to be constant along the Stream. Tidal models (Connors et al. 2006; Besla et al. 2012) predict that d increases approximately linearly along the MS as a function of MS Longitude, which would serve to increase the cross-section. From our *Cloudy* modeling to the low ions in 13 On-System directions, we adopt a median $\langle N(\mathrm{H\ II,\ on}) \rangle$=19.68 (Table 3), and this is not strongly dependent on N(H I). Equation (5) then gives M(H II, on)=$9.5{\times}10^8\,\mathrm{M}_\odot$. Comparing this to M(H I)=$4.87{\times}10^8\,\mathrm{M}_\odot$, we see that the majority of the Magellanic gas is ionized *even in On-System sightlines.*

M(H II, off) can be written in an analogous way, combining the cross-sectional area of 21 cm-faint ionized gas in the MSys with an estimate of the mean H II column $\langle N(\mathrm{H\ II,\ off}) \rangle$ in these Off-System directions:

$$\mathrm{M(H\ II, off)} = m_\mathrm{H} A(\mathrm{H\ II, off}) \langle N(\mathrm{H\ II, off}) \rangle. \quad (6)$$

Using our derived H II cross-section of the MSys of ≈11 000 square degrees (§3.1) and a distance of 55 kpc, we derive A(H II)≈$7.6{\times}10^{46}\,\mathrm{cm}^2$. Only two published derivations of N(H II, off) exist, in directions with far-UV data covering the sensitive high-order H I Lyman series absorption lines. In the HE0226–4110 direction, passing 10.8° from the $2.0{\times}10^{18}\,\mathrm{cm}^{-2}$ 21 cm contour of the MS, Fox et al. (2005a) measured an MS H I column of $\log N$(H I)=17.05 and derived $\log N$(H II, off)=18.75. In the Mrk 335 direction (part of the current sample), F10 measured $\log N$(H I)=16.67±0.05 and derived $\log N$(H II, off)=18.64–18.96, very similar to the level toward HE0226–4110.

With the large number of Off-System directions present in our sample, we can calculate N(H II, off) by summing the Si II, Si III, and Si IV columns to derive a total ionized silicon column in each direction, then using a 0.1 solar metallicity to convert this to an ionized hydrogen column:

$$N(\mathrm{H\ II,\ off}) = \frac{N(\mathrm{Si\ II} + \mathrm{Si\ III} + \mathrm{Si\ IV})}{0.1(\mathrm{Si/H})_\odot} \quad (7)$$

This does not include the contribution from unobserved highly-ionized states of silicon (Si V and above), but that would only serve to increase N(H II, off). Using 40 Off-System directions where at least one of Si II, Si III, and Si IV was detected, we find a mean and standard deviation $\log N$(H II, off)=18.93±0.50. Using this mean value in Equation 5, we derive M(H II, off)≈$5.5{\times}10^8\,\mathrm{M}_\odot$, smaller than M(H II, on) but slightly larger than M(H I).

Using Equations 4–7 above, we calculate that the total (neutral, warm ionized, and highly ionized) gas mass of the MSys is M(MSys)≈$2.0{\times}10^9\,(d/55\,\mathrm{kpc})^2\,\mathrm{M}_\odot$. If much of the Stream is at ≈100–150 kpc, a scenario predicted by recent tidal models (Besla et al. 2012) and supported by other arguments (Jin & Lynden-Bell 2008; Bland-Hawthorn et al. 2013), then this mass estimate

would increase by a factor of $(100/55)^2$ to $(150/55)^2$ or ≈3–7. As such our mass estimate is conservatively low.

An alternative, simpler method for estimating M(MSys) is to multiply the H I mass of $4.87\times10^8(d/55\,\mathrm{kpc})^2\,\mathrm{M}_\odot$ with the median ionized-to-neutral ratio derived in the 13 directions with photoionization models, $\langle N(\mathrm{total\ H\ II})/N(\mathrm{H\ I})\rangle$=6.4. This method gives M(MSys)≈$3.1\times10^9\,(d/55\,\mathrm{kpc})^2\,\mathrm{M}_\odot$, approximately 50% higher than the value derived from Equations 4–7. However, we adopt the lower value in our analysis below, since it accounts for the different ionization conditions in On- and Off-System directions.

We can calculate the contribution of the MS to M(MSys) by reevaluating Equation (4) without the contributions of the MB, LA, CHVC, and LMC Halo. Using $\mathrm{M(H\ I)_{MS}}=2.74\times10^8\,\mathrm{M}_\odot$ (including the Interface Region; Brüns et al. 2005), $A(\mathrm{H\ I})_{\mathrm{MS}} \approx 0.5A(\mathrm{H\ I})_{\mathrm{MSys}}$ ≈1 350 square degrees, and $A(\mathrm{H\ II})_{\mathrm{MS}}$ ≈5 500 square degrees (Figure 1b), we derive M(MS)≈$1.0\times10^9\,(d/55\,\mathrm{kpc})^2\,\mathrm{M}_\odot$, or approximately half of M(MSys). Our mass calculations can be summarized in simple terms: the MSys gas mass is approximately two billion solar masses and the MS gas mass is approximately one billion solar masses.

Our calculated value of M(MSys) is approximately twice the combined interstellar H I mass of the LMC ($4.4\times10^8\,\mathrm{M}_\odot$; Brüns et al. 2005; Bernard et al. 2008) and SMC ($4.0\times10^8\,\mathrm{M}_\odot$; Stanimirović et al. 1999; Brüns et al. 2005). Since ionized gas within the Magellanic Clouds is thought to be a minor contributor to their interstellar mass, a comparison of M(MSys) (the mass of gas stripped out of the Clouds) with the ISM mass remaining in the Magellanic Clouds shows that that *the MSys represents over two-thirds of the initial ISM mass of its two parent galaxies.* The MSys is therefore a striking example of the powerful nature of galaxy interactions and their ability to disperse the majority of a dwarf galaxy's gas (or two dwarf galaxies' gas) over large distances. The Milky Way will be the beneficiary of this interaction, since the MSys is now bound to the Galactic halo, and so the net result of the MSys creation is the transfer of gas out of the Magellanic Clouds and into the Galaxy's potential well.

The total MSys gas mass M(MSys)≈$2.0\times10^9\,(d/55\,\mathrm{kpc})^2\,\mathrm{M}_\odot$ can also be compared to (1) the stellar mass of the LMC disk, which is $2.7\times10^9\,\mathrm{M}_\odot$ (van der Marel 2006), only ≈50% more than the MSys gas mass; (2) the total mass of the ionized HVCs close the Milky Way disk, which is ≈$1.1\times10^8\,\mathrm{M}_\odot$ (Lehner & Howk 2011), indicating that the MSys is by far the most massive HVC complex around the Milky Way; (3) the total mass of the hot (∼10^6 K) Galactic corona out to 50 kpc, which for a uniform density can be written as $\mathrm{M_{hot}} \approx 1.7\times10^9\,\mathrm{M}_\odot(r_{\mathrm{hot}}/50\,\mathrm{kpc})^3(n_{\mathrm{hot}}/10^{-4}\,\mathrm{cm}^{-3})$. While r_{hot} and n_{hot} are poorly constrained (Bregman 2007; Gupta et al. 2012; Fang et al. 2013; Miller & Bregman 2013), the order-of-magnitude similarity of M(MSys) and the coronal mass has implications for the thermodynamics of the interaction between the MSys and the corona, because the corona cannot be viewed as an infinite heat reservoir. Instead, the passage of the MSys through the corona will simultaneously heat the Magellanic gas and cool the corona as the ensemble heads to energy equipartition. A similar "refrigeration" mechanism for the cooling of coronal gas by cool embedded clouds has been proposed for other (nearby) Galactic HVCs (Fraternali et al. 2013; Marasco et al. 2013).

6. INFLOW RATE OF MAGELLANIC GAS

Combining the average MS inflow velocity onto the Milky Way of ≈100 km s^{-1} (galactocentric; Mathewson et al. 1977) with a conservative MS distance d=55 kpc gives an inflow timescale of ≈540 Myr. If we instead use d=100 kpc, as may apply to the tip of the MS, then this timescale rises to ≈1.0 Gyr. Using M(MSys)≈$2.0\times10^9(d/55\,\mathrm{kpc})^2\,\mathrm{M}_\odot$, we then derive a *current-day* MSys inflow rate $\dot{\mathrm{M}}$(MSys)=M(MSys)/t of ≈3.7–6.7 $\mathrm{M}_\odot\,\mathrm{yr}^{-1}$ for d=55–100 kpc.

It is of interest to calculate the MS contribution to the MSys inflow rate, because the gas in the MB and LMC halo may be bound to the LMC and hence less likely to reach the Milky Way (unless stripped in the future). Using the value M(MS)≈$1.0\times10^9\,(d/55\,\mathrm{kpc})^2\,\mathrm{M}_\odot$ derived in the previous section, we derive $\dot{\mathrm{M}}$(MS)=M(MS)/t=1.9–3.4 $\mathrm{M}_\odot$ for d=55–100 kpc, or about half of the MSys inflow rate. Since one end of the MS is anchored to the Magellanic Clouds at 55 kpc, but the tip is likely to be closer to 100 kpc, the true MS inflow rate likely lies somewhere in-between these two values.

The MSys inflow rate is larger than the current Galactic star-formation rate (SFR), which recent measurements place between 0.68–1.45 $\mathrm{M}_\odot\,\mathrm{yr}^{-1}$ (Robitaille & Whitney 2010) and 1.9±0.4 $\mathrm{M}_\odot\,\mathrm{yr}^{-1}$ (Chomiuk & Povich 2011). *Therefore, the MSys is bringing in fuel at a rate sufficient to raise the Galactic SFR,* although whether or not it survives the journey to the disk depends on evaporative processes, as we discuss below.

The MSys inflow rate is also larger than the total (neutral plus ionized) inflow rate represented by all nearby ($d \lesssim$10–15 kpc) HVCs combined. Estimates for the HVC inflow rate vary, ranging from 0.08–0.4 $\mathrm{M}_\odot\,\mathrm{yr}^{-1}$ (Putman et al. 2012) based on a fit to the inflow rate represented by the largest 21 cm complexes, to 0.45–1.4 $\mathrm{M}_\odot\,\mathrm{yr}^{-1}$ (Lehner & Howk 2011) based on measuring the incidence of (predominantly ionized) HVCs seen in UV absorption lines toward background AGN and distant halo stars (see also Wakker et al. 1999, 2008; Shull et al. 2009; Collins et al. 2009). The MSys inflow rate surpasses both these estimates, and understanding the fate of the MSys is therefore crucial to understand the fueling of future star formation in the Galaxy.

A key question in determining the fate of the MSys is whether it will survive to reach the disk. Parts of the LA appear to have already reached the disk in the outer Galaxy (McClure-Griffiths et al. 2008), where the LA gas shows morphologies indicative of interaction with the ambient ISM, but the MS is further away, particularly the tip which may lie at ≳100 kpc (Besla et al. 2012). At 100 kpc the inflow time is ∼1 Gyr, which is much longer than the evaporation timescale for a small gas cloud being disrupted by its interaction with a hot corona: simulations find that clouds with H I masses $<10^{4.5}\,\mathrm{M}_\odot$ survive for ≈100 Myr (Heitsch & Putman 2009, see also

Bland-Hawthorn et al. 2007). The survival of the MSys therefore depends on which part of the structure is being considered, and on whether the gas fragments into smaller clumps or is stabilized against fragmentation (e.g. by magnetic fields; Kwak et al. 2009; Hill et al. 2013). Clear fragmentation and small-scale structure is seen in deep 21 cm observations of the MSys, particularly in the LA and MS tip regions (Wakker et al. 2002; Stanimirović et al. 2002, 2008; Westmeier & Koribalski 2008). Observations of high-ion absorption in the MS (Sembach et al. 2003; Fox et al. 2005a, F10, Paper II, this paper) are also indicative of MS/corona interactions, since the high ions are thought to trace the boundary layers between the H I and the hot corona.

The MS/corona interaction is disrupting the Stream's passage to the disk, and the evaporated gas must recondense and cool to participate in the Galactic inflow process instead of simply replenishing the hot corona with fresh material. Therefore the *current-day* gas inflow rate derived here will not necessarily equal the rate at which that fuel will be deposited in the disk in the future. However, an equilibrium scenario is possible in which infalling gas in the MSys evaporates into the corona at the same rate at which neutral gas condenses out of other (denser or more metal-enriched) regions, perhaps triggered by thermal instability (Field 1965; Oort 1966; Maller & Bullock 2004; Joung et al. 2012a). In this case, the MSys would be effectively fueling the halo rather than directly fueling star formation in the disk. We note that a population of H I clouds has been identified in the inner Galaxy, which could represent objects that have condensed out of the hot corona (Lockman et al. 2002; Stil et al. 2006, see also Peek et al. 2008).

Despite the evidence for an evaporative encounter between the Stream and the Milky Way corona, the fact that the MS has survived to reach its current age of $\approx$2 Gyr is itself an important clue to its fate. Murali (2000) argued that the continued existence of the MS constrains the density of the surrounding hot corona to be $\log(n_{\rm H}/{\rm cm}^{-3})<-5.0$ at the distance to the Stream, because otherwise the Stream would have been destroyed within $\approx$500 Myr by the ram pressure exerted by the hot corona. Although this density is lower than expectations for the coronal density at $\approx$50 kpc (e.g. Stanimirović et al. 2002; Grcevich & Putman 2009), recent proper-motion observations show that the Magellanic Clouds may be on their first infall into the Galactic halo (Besla et al. 2010; Kallivayalil et al. 2013). In this case, the density of the surrounding gas (and hence the strength of the ram pressure) was lower in the past, when the Stream was at larger Galactocentric radius, allowing the Stream to survive for longer than would otherwise be the case.

Our study of the MSys has indicated that the true role of tidal gas streams may be more subtle than the *direct* transport of fuel to the disks of massive galaxies. Instead, we favor a scenario where tidal streams serve to replenish the hot coronae of massive galaxies with new material at large galactocentric radii, and where cool gas clouds condense out of other, denser regions of these coronae via the thermal instability. In this picture, gaseous tidal streams represent one evanescent component of galaxy ecosystems in which hot coronae are equally important players. This illustrates the crucial and complex role of the gas cycle in the evolution of galaxies.

7. CONNECTION OF MAGELLANIC SYSTEM TO QUASAR ABSORPTION LINE SYSTEMS

Given its large cross-section and gas mass, the MSys provides an interesting case-study for understanding the origin of intervening quasar absorption line (QAL) systems. If the MSys was observed as an intervening absorber along a random sightline through the Galactic halo, it would present a UV metal-line covering fraction of $\approx$1/4 out to 55 kpc (based on the covering fraction of $\approx$1/4 observed at the solar circle). Since most of this material is below the detection threshold for 21 cm emission, it has H I column densities of $10^{16}<\log N({\rm H\ I})<10^{19}\,{\rm cm}^{-2}$ that classify it as a Lyman Limit System (LLS). Low-redshift LLSs have a bimodal metallicity distribution (Lehner et al. 2013) and a substantial highly-ionized phase (Fox et al. 2013b), and their relationship to galaxies is only known in a small number of cases (Jenkins et al. 2005; Rao et al. 2011; Ribaudo et al. 2011; Lehner et al. 2013). Our results show that tidally-stripped material can produce a LLS at impact parameters of $\approx$50–100 kpc from a star-forming ($\approx L_*$) spiral galaxy, and that such material can have a substantial covering fraction.

The 10^4 K ionized material in the MSys is effectively part of the Milky Way's cool circumgalactic medium (CGM). Werk et al. (2014) recently calculated the mass of the cool CGM around low-redshift $\sim L_*$ galaxies to be $>6\times10^{10}\,{\rm M}_\odot$ out to 150 kpc. Our results show that the MSys dominates the mass budget of the Galactic cool CGM, and hence that tidally stripped material can be the dominant form of such gas around $\approx L_*$ galaxies. That being said, the fact that the Milky Way possesses two dwarf irregular satellite galaxies within $\approx$50 kpc makes it highly aptyical (Tollerud et al. 2011), so although the Milky Way's gaseous halo offers a fertile test bed for CGM studies, caution is needed about using it to draw general conclusions about L_* galaxy halos.

Optical absorption-line measurements of Ca II, which serves as tracer for neutral gas with $\log N({\rm H\ I})\geq17.4$, demonstrate that the neutral-gas cross-section of galaxy halos exceeds that of galaxy disks by a factor of 2–3 (Richter et al. 2011). These measurements further indicate that the characteristic neutral-gas extent of galaxy halos at low redshift is $\approx$55 kpc, in line with the spatial distribution of neutral gas around the Milky Way and M31 (Richter 2012). Direct 21 cm searches for neutral gas in the extended halos of Milky-Way-type galaxies indicate that only a relatively small fraction contain H I structures detectable in emission beyond the disk-halo interface (Heald et al. 2011). One exception is the nearby spiral galaxy NGC 6946, which is connected to its nearest satellites by diffuse, filamentary H I (Pisano 2014). A clumpy H I filament has also been detected between M31 and M33 (Wolfe et al. 2013). Many such (possibly tidal) gas streams may await their detection in more sensitive 21 cm observations.

8. SUMMARY

We have presented an absorption-line survey of ionization in the MSys (MS, MB, LMC Halo, and LA) using a sample of medium-resolution (18 km s^{-1} FWHM) *HST*/COS UV spectra of 69 background AGN ly-

ing within 30° of the 21 cm emission from the MSys. These data are supplemented by Wisconsin Hα Mapper (WHAM) Hα emisssion-line observations in nine directions, and 21 cm emission spectra from the LAB survey, GASS survey, and additional Parkes telescope observations. The sightlines sample approximately four orders of magnitude of H I column density, ranging from the dense cores of the MB to the diffuse outer layers of the MS and LA. This dataset has allowed us to characterize the physical properties of the MSys and its relationship to the extended Galactic halo. Our main results are the following.

1. **Detection Rate**. UV absorption at Magellanic velocities is detected in 56 out of 69 directions (81% detection rate). The detected lines include one or more of Si III λ1206, Si II λ1190, C II λ1334, Si IV λ1393, and C IV λ1548, and occasionally other lines including O I λ1302. Since the 21 cm-emitting regions of the MSys cover 2 701 square degrees (Nidever et al. 2010), the total cross-section of the MSys is enormous, at ≈11 000 square degrees, which is around a quarter of the entire sky. The ionized (UV-absorbing) regions occupy ≈four times as much area as the neutral (21 cm-emitting) regions.

2. **Line ratios**. We measure the column-density ratios Si III/Si II, Si IV/Si II, and C IV/C II in the Magellanic gas. Among directions with 21 cm detections (with $\log N(\mathrm{H\ I}) \gtrsim 18$), all three ratios show significant anti-correlations with $N(\mathrm{H\ I})$ (Figure 4). In addition, Si IV/Si II and C IV/C II each show weak (but significant) anti-correlations with MS Longitude, such that the ionization level increases along the Stream from the Magellanic Clouds toward the tip. Given our current understanding of the Stream's orbit, in which the tip is the most distant region, this result is equivalent to an increase in ionization level with Galactocentric distance, consistent with the observed decline in $N(\mathrm{H\ I})$ along the MS.

3. **Ionization parameter and gas density.** Using *Cloudy* photoionization models applied to 13 Magellanic directions with measured H I columns and Si III/Si II ratios, we derive ionization parameters $\log U$ in the Magellanic gas ranging from –3.8 to –3.1 with a median value of –3.5. This corresponds to an average Magellanic gas density $\log(n_{\mathrm{H}}/\mathrm{cm}^{-3}) \approx -1.8$ given the calculated density of the ionizing radiation field (including both Milky Way and Magellanic photons).

4. **Ionization level and warm H II column.** The hydrogen ionization level $x_{\mathrm{H\ II}}$ varies considerably between MSys regions, depending on the H I column. In the MB, where $\log N(\mathrm{H\ I}) \gtrsim 20$, $x_{\mathrm{H\ II}} \approx 20\%$, whereas the directions with $\log N(\mathrm{H\ I}) \lesssim 19.5$ have $x_{\mathrm{H\ II}}$ up to ≈98%. Since the Off-Stream directions have a larger cross-section than the On-Stream directions, the gas is predominantly ionized in most sightlines through the MSys, and even the phase referred to as "low-ion" phase is predominantly ionized. The warm H II columns in the low-ion phase of the MSys take a fairly narrow range of values, between $\log N(\mathrm{H\ II}) \approx 19.4$–$20.1$, even though the H I columns in the same directions cover several orders of magnitude.

5. **Thermal pressure.** The MS thermal pressure P/k calculated from the photoionization models varies from ≈30–250 cm^{-3} K in the six Stream directions analyzed. This places the Stream close to pressure equilibrium in a two-million-degree hydrostatic Galactic corona at 50–100 kpc, where P_{corona}/k=100–250 cm^{-3} K in the isothermal models of Sternberg et al. (2002).

6. **Total mass**. We calculate the total (neutral plus ionized) gas mass of the MSys to be $\mathrm{M(MSys)} \sim 2.0\times10^9\,(d/55\,\mathrm{kpc})^2\,\mathrm{M}_\odot$, by combining the H I mass of $4.9\times10^8\,\mathrm{M}_\odot$ (Brüns et al. 2005) with estimates of the H II mass in 21 cm-bright regions ($9.5\times10^8\,\mathrm{M}_\odot$) and 21 cm-faint regions ($5.5\times10^8\,\mathrm{M}_\odot$). The MS accounts for about half of the mass in the MSys. M(MSys) is over twice as large as the remaining interstellar H I mass of the LMC and SMC combined, indicating *these two dwarf galaxies have lost over two-thirds of their initial gas mass.* M(MSys) is also comparable to the mass of the hot Galactic corona out to 50 kpc, $\mathrm{M_{hot}} \approx 1.7\times10^9\,\mathrm{M}_\odot (r_{\mathrm{hot}}/50\,\mathrm{kpc})^3 (n_{\mathrm{hot}}/10^{-4}\,\mathrm{cm}^{-3})$, although r_{hot} and n_{hot} are poorly constrained. The similarity between the mass of the MSys and the corona indicates that energetically, both components will be affected by their mutual interaction, causing the corona to cool as the Magellanic gas heats up.

7. **Mass flow rate onto the Galaxy.** The present-day infall rate of the MSys onto the Milky Way is ≈3.7–6.7 $\mathrm{M}_\odot\,\mathrm{yr}^{-1}$, using an average galactocentric infall velocity of 100 $\mathrm{km\,s}^{-1}$, a MS distance of 55–100 kpc, and the total gas mass derived above. This is considerably larger than the inflow rate of all nearby HVCs combined and larger than the current SFR of the Galaxy (≈1–2 $\mathrm{M}_\odot\,\mathrm{yr}^{-1}$). *The MSys therefore has the potential to raise the global Galactic SFR.* However, this gaseous fuel faces a tortuous path to reach the disk: multiple signs of an evaporative encounter with the hot corona suggests that the MSys is disintegrating and replenishing the hot coronae with fresh material at large galactocentric radii. For the inflow rate across the entire halo to be in or close to equilibrium, cooler clouds must condense out of other, denser or more metal-enriched regions of the corona. The MSys can therefore be thought of as fueling the Galactic halo rather than directly fueling star formation in the disk.

Acknowledgments. We thank David Nidever for providing the total area and velocity field of the H I emission from the Magellanic System. Support for programs 11692, 12204, 12263, and 12604 was provided by NASA through grants from the Space Telescope Science Institute, which is operated by the Association of Universities for Research in Astronomy, Inc., under NASA contract

NAS 5-26555. WHAM science and ongoing operations are supported by NSF award AST 1108911. The Parkes radio telescope is part of the Australia Telescope National Facility which is funded by the Commonwealth of Australia for operation as a National Facility managed by CSIRO. K.A.B. is supported through NSF Astronomy and Astrophysics Postdoctoral Fellowship award AST 1203059. The research was partially supported by the Japan Society for the Promotion of Science through Grant-in-Aid for Scientific Research 23740148.

REFERENCES

Anderson, M. E., Bregman, J. N., & Dai, X. 2013, ApJ, 762, 106
Asplund, M., Grevesse, N., Jacques Sauval, A., & Scott, P. 2009, ARA&A, 47, 481
Barger, K. A., Haffner, L. M., & Bland-Hawthorn, J. 2013, ApJ, 771, 132
Barger, K. A., et al. 2014, ApJ, in prep.
Bauermeister, A., Blitz, L., & Ma, C.-P. 2010, ApJ, 717, 323
Ben Bekhti, N., Winkel, B., Richter, P., et al. 2012, A&A, 542, A110
Bernard, J.-P., Reach, W. T., Paradis, D., et al. 2008, AJ, 136, 919
Besla, G., Kallivayalil, N., Hernquist, L., et al. 2010, ApJ, 721, L97
Besla, G., Kallivayalil, N., Hernquist, L., et al. 2012, MNRAS, 421, 2109
Binney, J., Dehnen, W., & Bertelli, G. 2000, MNRAS, 318, 658
Bland-Hawthorn, J., & Maloney, P. R. 1999, ApJ, 510, L33
Bland-Hawthorn, J., & Maloney, P. R. 2002, in ASP Conf. Proc. 254, *Extragalactic Gas at Low Redshift*, ed. J. S. Mulchaey & J. Stocke (San Francisco: ASP), 267
Bland-Hawthorn, J., Sutherland, R., Agertz, O., & Moore, B. 2007, ApJ, 670, L109
Bland-Hawthorn, J., Maloney, P., Sutherland, R. S., & Madsen, G. J. 2013, ApJ, 778, 58
Bregman, J. N. 2007, ARA&A, 45, 221
Brüns, C, Kerp, J., Staveley Smith, L., et al. 2005, A&A, 432, 45
Burchett, J. N., Tripp, T. M., Werk, J. K., et al. 2013, ApJ, 779, L17
Chemin, L., Carignan, C., & Foster, T. 2009, ApJ, 705, 1395
Chiappini, C., Matteucci. F., & Romano, D. 2001, ApJ, 554, 1044
Chomiuk, L. & Povich, M. S. 2011, AJ, 142, 197
Collins, J. A., Shull, J. M., & Giroux, M. L. 2004, ApJ, 605, 216
Collins, J. A., Shull, J. M., & Giroux, M. L. 2005, ApJ, 623, 196
Collins, J. A., Shull, J. M., & Giroux, M. L. 2009, ApJ, 705, 962
Connors, T. W., Kawata, D., & Gibson, B. K. 2006, MNRAS, 371, 108
Diaz, J. D., & Bekki, K. 2011, ApJ, 413, 2015
Diaz, J. D., & Bekki, K. 2012, ApJ, 750, 36
Dieter, N. H. 1965, AJ, 70, 552
Dieter, N. H. 1971, A&A, 12, 59
Fang, T., Bullock, J., & Boylan-Kolchin, M. 2013, ApJ, 762, 20
Ferland, G. J., Korista, K. T., Verner, D. A., et al. 1998, PASP, 110, 761
Fernández, X., Joung, M. R., & Putman, M. E. 2012, ApJ, 749, 181
Field, G. B. 1965, 142, 531
Fox, A. J., Savage, B. D., Wakker, B. P., et al. 2004, ApJ, 602, 738
Fox, A. J., Wakker, B. P., Savage, B. D., et al. 2005a, ApJ, 630, 332
Fox, A. J., Savage, B. D., & Wakker, B. P. 2005b, AJ, 130, 2418
Fox, A. J., Savage, B. D., & Wakker, B. P 2006, ApJS, 165, 229
Fox, A. J., Wakker, B. P., Smoker, J. V., et al. 2010, ApJ, 718, 1046 (F10)
Fox, A. J., Richter, P., Wakker, B. P., et al. 2013a, ApJ, 772, 110 (Paper I)
Fox, A. J., Lehner, N., Tumlinson, J., et al. 2013b, ApJ, 778, 187
Fraternali, F., Marasco, A., Marinacci, F., & Binney, J. 2013, ApJ, 764, L21
Fumagalli, M., Prochaska, J. X., Kasen, D., et al. 2011, MNRAS, 418, 1796
Ganguly, R., Sembach, K. R., Tripp, T. M., & Savage, B. D. 2005, ApJS, 157, 251
Gardiner, L. T., & Noguchi, M. 1996, MNRAS, 278, 191
Gibson, B. K., Giroux, M. L., Penton, S. V., et al. 2000, AJ, 120, 1803
Gnat, O., & Sternberg, A. 2007, ApJS, 168, 213
Green, J. C., Froning, C. S., Osterman, S., et al. 2012, ApJ, 744, 60
Grcevich, J., & Putman, M. E. 2009, ApJ, 696, 385
Gupta, A., Mathur, S., Krongold, Y., Nicastro, F., & Galeazzi, M. 2012, ApJ, 756, L8
Haardt, F. & Madau, P. 2012, ApJ, 746, 125
Haffner, L. M., Reynolds, R. J., Tufte, S. L., et al. 2003, ApJS, 149, 405
Harris, J., & Zaritsky, D. 2004, AJ, 127, 1532
Heald, G., Józsa, G., Serra, P., et al. 2011, A&A, 526, A118
Heitsch, F., & Putman, M. E. 2009, ApJ, 698, 1485
Herenz, P., Richter, P., Charlton, J. C., & Maseiro J. R. 2013, A&A, 550, 87
Hill, A. S., Mao, S. A., Benjamin, R. A., Lockman, F. J., & McClure-Griffiths, N. M. 2013, ApJ, 777, 55
Holland, S. T., et al. 2014, Cosmic Origins Spectrograph Instrument Handbook, Version 6.0 (Baltimore: STScI)
Jenkins, E. B., Bowen, D. V., Tripp, T. M., & Sembach, K. R. 2005, ApJ, 623, 767
Jin, S., & Lynden-Bell, D. 2008, MNRAS, 383, 1686
Joung, M. R., Bryan, G. L., & Putman, M. E. 2012, ApJ, 745, 148
Joung, M. R., Putman, M. E., Bryan, G. L., Fernandez, X., & Peek, J. E. G. 2012, ApJ, 759, 137
Kalberla, P. M. W., Burton, W. B., Hartmann, D., et al. 2005, A&A, 440, 775
Kalberla, P. M. W., McClure-Griffiths, N. M., Pisano, D. J., et al. 2010, A&A, 521, 17
Kallivayalil, N., van der Marel, R. P., Besla, G., Anderson, J., & Alcock, C. 2013, ApJ, 764, 161
Kereš, D., Katz N., Weinberg D. H., et al. 2005, MNRAS, 363, 2
Kereš, D., Katz N., Fardal, M., et al. 2009, MNRAS, 395, 160
Kumari, N., Fox, A. J., Tumlinson, J., et al. 2014, ApJ, in prep.
Kwak, K., Shelton, R. L., & Raley, E. A. 2009, ApJ, 699, 1775
Larson, R. B., Tinsley, B. M., & Caldwell, C. N. 1980, ApJ, 237, 692
Lehner, N., & Howk, J. C. 2007, MNRAS, 377, 687
Lehner, N., & Howk, J. C. 2010, ApJ, 709, 138
Lehner, N., & Howk, J. C. 2011, Science, 334, 955
Lehner, N., Howk, J. C., Keenan, F. P., & Smoker, J. V. 2008, ApJ, 678, 219
Lehner, N., Staveley-Smith, L., & Howk, J. C. 2009, ApJ, 702, 940
Lehner, N., Howk, J. C., Thom, C., et al. 2012, MNRAS, 424, 2896
Lehner, N., Howk, J. C., Tripp, T. M., et al. 2013, ApJ, 770, 138
Lockman, F. J. 2002, ApJ, 580, L47
Lu, L., Savage, B. D., Sembach, K. R. 1994, ApJ, 437, L119
Lu, L., Savage, B. D., Sembach, K. R., et al. 1998, AJ, 115, 162
Maller, A. H., & Bullock, J. S. 2004, MNRAS, 355, 694
Marasco, A., Marinacci, F., & Fraternali, F. 2013, MNRAS, 433, 1634
Mastropietro, C., Moore, B., Mayer, L., Wadsley, J., & Stadel, J. 2005, MNRAS, 363, 509
Mathewson, D. S., Cleary, M. N., & Murray, J. D. 1974, ApJ, 190, 291
Mathewson, D. S., Schwarz, M. P., & Murray, J. D. 1977, ApJ, 217, L5
McClure-Griffiths, N. M., Staveley-Smith, L, Lockman, F. J., et al. 2008, ApJ, 673, L143
McClure-Griffiths, N. M., Pisano, D. J., Calabretta, M. R., et al. 2009, ApJS, 181, 398
Meurer, G. R., Bicknell, G. V., & Gingold, R. A. 1985, PASAu, 6, 195
Miller, M. J., & Bregman, J. N. 2013, ApJ, 770, 118
Misawa, T., Charlton, J. C., Kobulnicky, H. A., Wakker, B. P., & Bland-Hawthorn, J. 2009, ApJ, 695, 1382
Moore, B., & Davis, M. 1994, MNRAS, 270, 209
Morras, R., Bajaja, E., Arnal, E. M., & Pöppel, W. G. L. 2000, A&AS, 142, 25
Morton, D. C. 2003, ApJS, 149, 205
Muller, C. A., Oort, J. H., & Raimond, E. 1963, CRAS, 257, 1661
Murali, C. 2000, ApJ, 529, L81
Murante, G., Calabrese, M., De Lucia, G., et al. 2012, ApJ, 749, 34

Nidever, D. L., Majewski, S. R., & Burton, W. B. 2008, ApJ, 679, 432 (N08)
Nidever, D. L., Majewski, S. R., Burton, W. B., & Nigra, L. 2010, ApJ, 723, 1618
Nigra, L., Stanimirović, S., Gallagher, J. S., et al. 2012, ApJ, 760, 48
Oort, J. H. 1966, Bull. Astron. Inst. Netherlands, 18, 421
Oppenheimer, B. D., & Schaye, J. 2013, MNRAS, 434, 1043
Pagel, B. E. J., & Tautvaisiene, G. 1998, MNRAS, 299, 535
Peek, J. E. G., Putman, M. E., & Sommer-Larsen, J. 2008, ApJ, 674, 227
Pisano, D. J. 2014, AJ, 147, 48
Putman, M. E., Gibson, B. K., Staveley-Smith, L., et al. 1998, Nature, 394, 752
Putman, M. E., Staveley-Smith, L., Freeman, K. C., Gibson, B. K., & Barnes, D. G. 2003a, ApJ, 586, 170
Putman, M. E., Bland-Hawthorn, J., Veilleux, S., et al. 2003b, ApJ, 597, 948
Putman, M. E., Peek, J. E. G., & Joung, M. R. 2012, ARA&A, 50, 491
Rao, S. M., Belfort-Mihalyi, M., Turnshek, D. A., et al. 2011, MNRAS, 416, 1215
Ribaudo, J., Lehner, N., Howk, J. C., et al. 2011, ApJ, 743, 207
Richter, P. 2006, Rev. Mod. Astron., 19, 31
Richter, P. 2012, ApJ, 750, 165
Richter, P., Sembach, K. R., Wakker, B. P., Savage, B. D., 2001, ApJ, 562, L181
Richter, P., Charlton, J. C., Fangano, A. P. M., Bekhti, N. B., & Maseiro, J. R. 2009, ApJ, 695, 1631
Richter, P., Krause, F., Fechner, C., Charlton, J. C., & Murphy, M. T. 2011, A&A, 528, A12
Richter, P., Fox, A. J., Wakker, B. P., et al. 2013, ApJ, 772, 111 (Paper II)
Robitaille, T. P. & Whitney, B. A. 2010, ApJ, 710, L11
Rubin, K. H. R., Prochaska, J. X., Koo, D. C., & Phillips, A. C. 2012, ApJ, 747, 26
Savage, B. D., & Sembach, K. R. 1991, ApJ, 379, 245
Sembach, K. R., Savage, B. D., Lu, L., & Murphy, E. M. 1999, ApJ, 515, 108
Sembach, K. R., Howk, J. C., Savage, B. D., & Shull, J. M., 2001, AJ, 121, 992
Sembach, K. R., Gibson, B. K., Fenner, Y, & Putman, M. E. 2002, ApJ, 572, 178
Sembach, K. R., Wakker, B. P., Savage, B. D., et al. 2003, ApJS, 146, 165
Shen, S., Madau, P., Guedes, J., et al. 2013, ApJ, 765, 89
Shull, J. M., Jones, J. R., Danforth, C. W., & Collins, J. A. 2009, ApJ, 699, 754
Shull, J. M., Stevans, M., Danforth, C., et al. 2011, ApJ, 739, 105
Smoker, J. V., Fox, A. J., & Keenan, F. P. 2011, MNRAS, 415, 1105
Stanimirović, S., Staveley-Smith, L., Dickey, J. M., Sault, R. J., & Snowden, S. L. 1999, MNRAS, 302, 417
Stanimirović, S., Dickey, J. M.; Krčo, M., & Brooks, A. M. 2002, ApJ, 576, 773
Stanimirović, S., Hoffman, S., Heiles, C., et al. 2008, ApJ, 680, 276
Staveley-Smith, L., Kim, S., Calabretta, M. R., Haynes, R. F., & Kesteven, M. J. 2003, MNRAS, 339, 87
Sternberg, A., McKee, C., & Wolfire, M. et al. 2002, ApJS, 143, 419
Stewart, K. R., Kaufmann, T., Bullock, J. S., et al. 2011, ApJ, 735, L1
Stil, J. M., Lockman, F. J., Taylor, A. R., et al. 2006, ApJ, 637, 366
Sutherland, R. S., & Dopita, M. A. 1993, ApJS, 88, 253
Thilker, D. A., Braun, R., Walterbos, R. A. M., et al. 2004, ApJ, 601, L39
Thom, C., Peek, J. E. G., Putman, M. E., et al. 2008, ApJ, 684, 364
Tollerud, E. J., Boylan-Kolchin, M., Barton, E. J., Bullock, J. S., & Trinh, C. Q. 2011, ApJ, 738, 102
Tripp, T. M., & Song, L. 2012, ApJ, 746, 173
Tripp T. M., Wakker, B. P., Jenkins, E. B. et al. 2003, AJ, 125, 3122
Twarog, B. A. 1980, ApJ, 242, 242
van de Voort, F., & Schaye, J. 2012, MNRAS, 423, 2991
van der Marel, R. P. 2006, Proc. STScI Symp., *The Local Group as an Astrophysical Laboratory*, ed. M. Livio & T. M. Brown (Cambridge: Cambridge Univ. Press), 47
Vogelsberger, M., Sijacki, D., Kereš, D., Springel, V., & Hernquist, L. 2012, MNRAS, 425, 3024
Wakker, B. P. 2001, ApJS, 136, 463
Wakker, B. P. & van Woerden, H. 1997, ARA&A, 35, 217
Wakker, B. P., et al. 1999, Nature, 402, 388
Wakker, B. P., Oosterloo, T. A., & Putman, M. E. 2002, AJ, 123, 1953
Wakker, B. P., York, D. G., Wilhelm, R., et al. 2008, ApJS, 146, 1
Wannier, P., & Wrixon, G. T., & Wilson, R. W. 1972, A&A, 18, 224
Wannier, P., & Wrixon, G. T. 1972, ApJ, 173, L119
Weiner, B. J., & Williams, T. B. 1996, AJ, 111, 1156
Welsh, B. Y., Wheatley, J., & Lallement, R. 2011, PASP, 123, 914
Werk, J. K., Prochaska, J. X., Tumlinson, J., et al. 2014, ApJ, submitted (arXiv:1403.0947)
Westmeier, T., & Koribalski, B. S. 2008, MNRAS, 388, L29
Wolfe, S. A., Pisano, D. J., Lockman, F. J., McGaugh, S. S., & Shaya, E. J. 2013, Nature, 497, 224
Zech, W. F., Lehner, N., Howk, J. C., Dixon, W. V. D., & Brown, T. M. 2008, ApJ, 679, 460

APPENDIX

The figures below show the *HST*/COS absorption-line profiles for all sightlines in the sample, sorted alphabetically. The title of each stack includes a numerical ID and the Magellanic coordinates of the target, which can be used to cross-reference with Figure 1, and a label identifying the region of the MSys probed by the sightline (MS-On, MS-Off, LA-On, LA-Off, Bridge, LMC Halo, or CHVC). The top panels of each stack show the H I 21 cm emission profile from either the Parkes telescope, the LAB survey, or the GASS survey, with brightness temperature plotted versus LSR velocity, and with the y-range scaled to the strength of the Magellanic emisison, regardless of the strength of the (usually stronger) Galactic emission. All other panels show the COS spectra, with normalized flux plotted against LSR velocity. The dotted vertical lines show the central velocity (solid) and velocity integration range (dashed) of Magellanic absorption and emission. In sightlines where Magellanic 21 cm emission is detected, these vertical lines are red and the solid line shows the centroid of the H I emission. In sightlines without Magellanic 21 cm emission but with UV absorption, these lines are blue and the solid line shows the velocity of the strongest UV absorption. In sightlines with neither 21 cm emission nor UV absorption at Magellanic velocities, the velocity integration range is taken from the predicted velocity field of the MSys in that direction (Figure 1b), and no centroid is given. The shaded gray regions denote the velocity interval of Magellanic absorption.

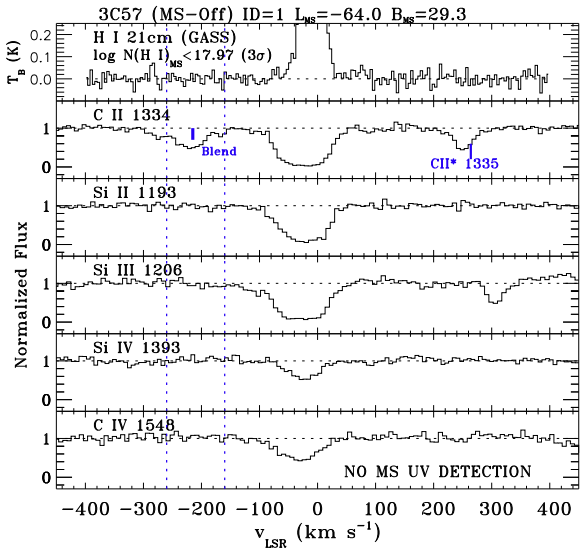
3C57 (MS−Off) ID=1 L_MS=−64.0 B_MS=29.3
H I 21cm (GASS)
log N(H I)_MS<17.97 (3σ)
C II 1334
Blend
CII* 1335
Si II 1193
Si III 1206
Si IV 1393
C IV 1548
NO MS UV DETECTION
T_B (K)
Normalized Flux
v_LSR (km s^-1)

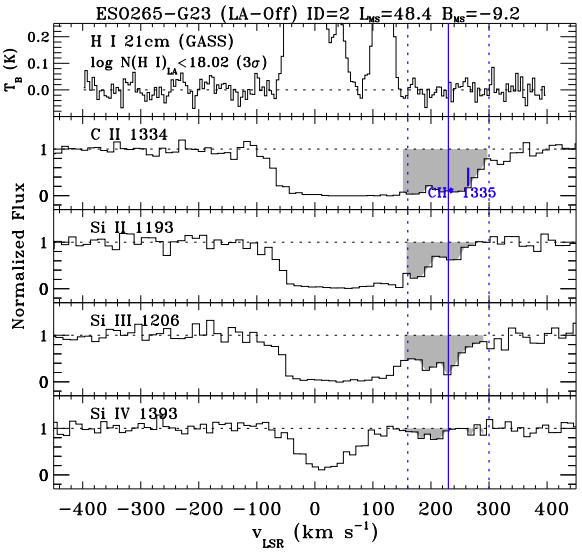
ES0265−G23 (LA−Off) ID=2 L_MS=48.4 B_MS=−9.2
H I 21cm (GASS)
log N(H I)_LA<18.02 (3σ)
C II 1334
CII* 1335
Si II 1193
Si III 1206
Si IV 1393
T_B (K)
Normalized Flux
v_LSR (km s^-1)

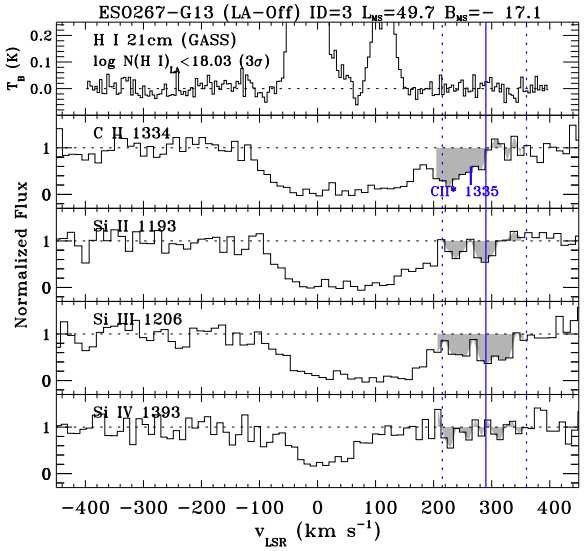
ES0267−G13 (LA−Off) ID=3 L_MS=49.7 B_MS=− 17.1
H I 21cm (GASS)
log N(H I)_LA<18.03 (3σ)
C II 1334
CII* 1335
Si II 1193
Si III 1206
Si IV 1393
T_B (K)
Normalized Flux
v_LSR (km s^-1)

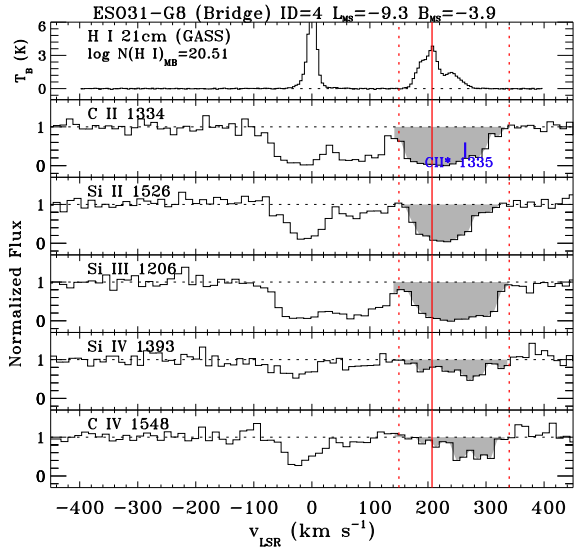
ES031−G8 (Bridge) ID=4 L_MS=−9.3 B_MS=−3.9
H I 21cm (GASS)
log N(H I)_MB=20.51
C II 1334
CII* 1335
Si II 1526
Si III 1206
Si IV 1393
C IV 1548
T_B (K)
Normalized Flux
v_LSR (km s^-1)

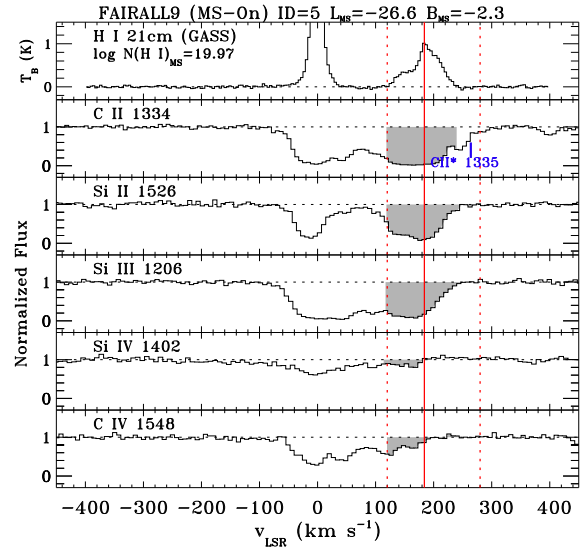
FAIRALL9 (MS−On) ID=5 L_MS=−26.6 B_MS=−2.3
H I 21cm (GASS)
log N(H I)_MS=19.97
C II 1334
CII* 1335
Si II 1526
Si III 1206
Si IV 1402
C IV 1548
T_B (K)
Normalized Flux
v_LSR (km s^-1)

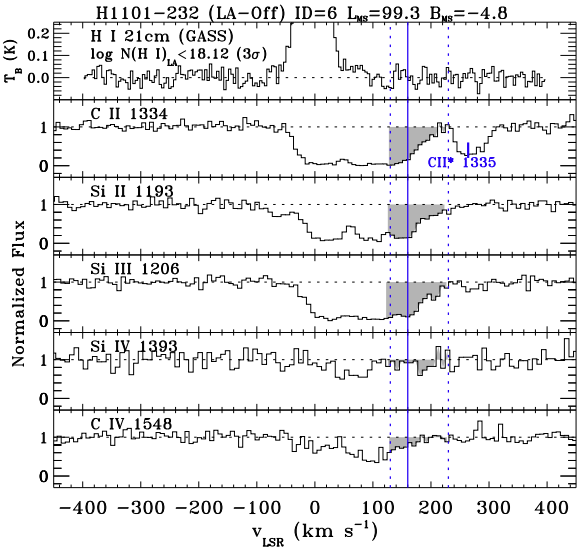
H1101−232 (LA−Off) ID=6 L_MS=99.3 B_MS=−4.8
H I 21cm (GASS)
log N(H I)_LA<18.12 (3σ)
C II 1334
CII* 1335
Si II 1193
Si III 1206
Si IV 1393
C IV 1548
T_B (K)
Normalized Flux
v_LSR (km s^-1)

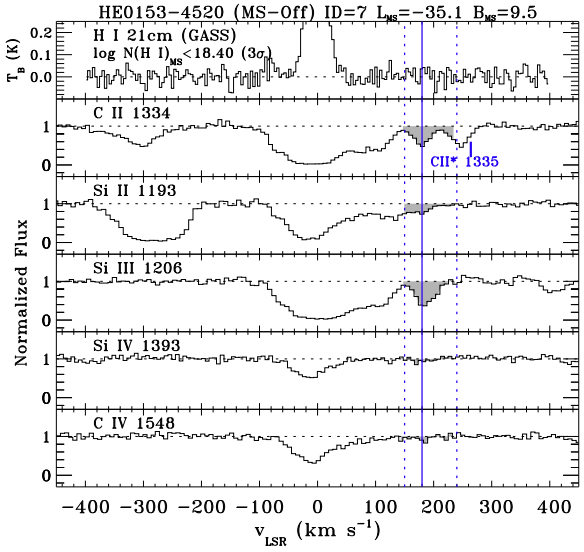
HE0153−4520 (MS−Off) ID=7 L_MS=−35.1 B_MS=9.5
H I 21cm (GASS)
log N(H I)_MS<18.40 (3σ)
C II 1334
CII* 1335
Si II 1193
Si III 1206
Si IV 1393
C IV 1548
T_B (K)
Normalized Flux
v_LSR (km s^−1)

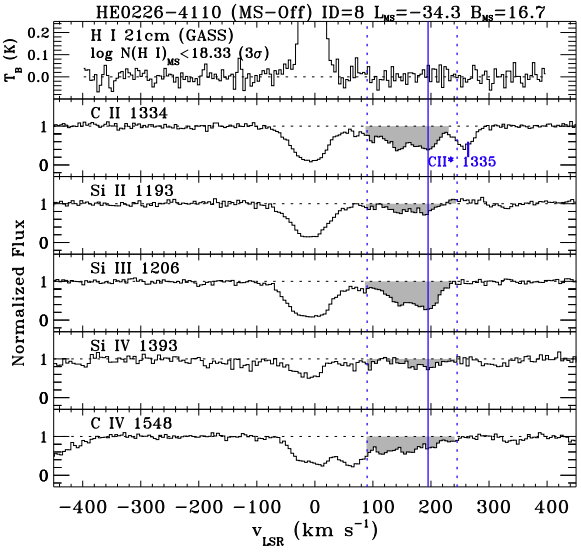
HE0226−4110 (MS−Off) ID=8 L_MS=−34.3 B_MS=16.7
H I 21cm (GASS)
log N(H I)_MS<18.33 (3σ)
C II 1334
CII* 1335
Si II 1193
Si III 1206
Si IV 1393
C IV 1548
T_B (K)
Normalized Flux
v_LSR (km s^−1)

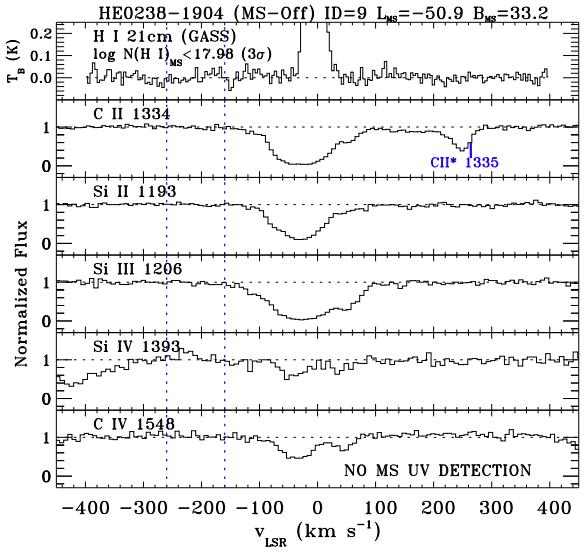
HE0238−1904 (MS−Off) ID=9 L_MS=−50.9 B_MS=33.2
H I 21cm (GASS)
log N(H I)_MS<17.98 (3σ)
C II 1334
CII* 1335
Si II 1193
Si III 1206
Si IV 1393
C IV 1548
NO MS UV DETECTION
T_B (K)
Normalized Flux
v_LSR (km s^−1)

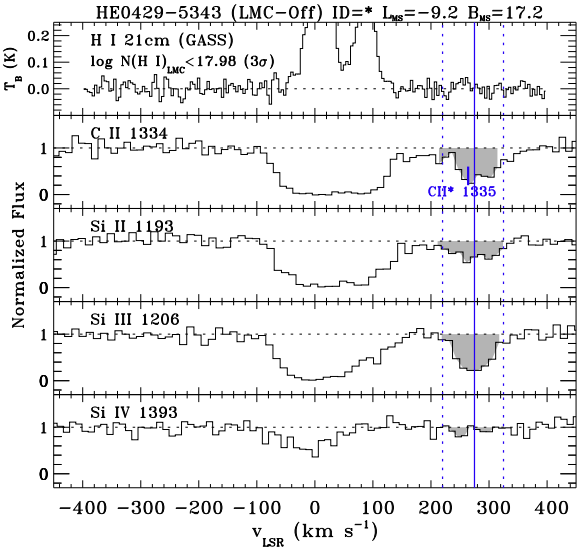
HE0429−5343 (LMC−Off) ID=* L_MS=−9.2 B_MS=17.2
H I 21cm (GASS)
log N(H I)_LMC<17.98 (3σ)
C II 1334
CII* 1335
Si II 1193
Si III 1206
Si IV 1393
T_B (K)
Normalized Flux
v_LSR (km s^−1)

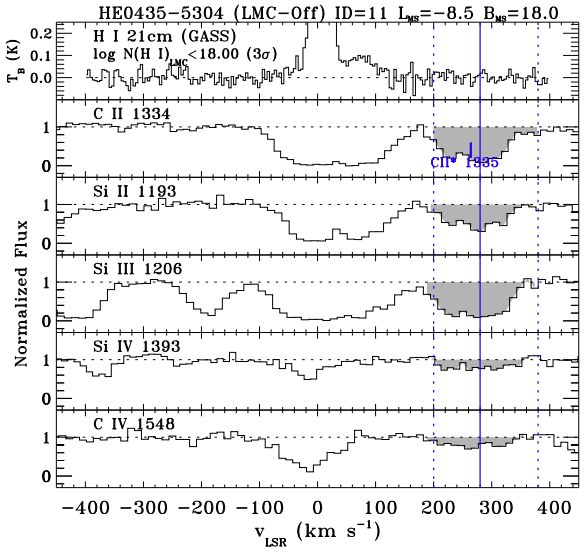
HE0435−5304 (LMC−Off) ID=11 L_MS=−8.5 B_MS=18.0
H I 21cm (GASS)
log N(H I)_LMC<18.00 (3σ)
C II 1334
CII* 1335
Si II 1193
Si III 1206
Si IV 1393
C IV 1548
T_B (K)
Normalized Flux
v_LSR (km s^−1)

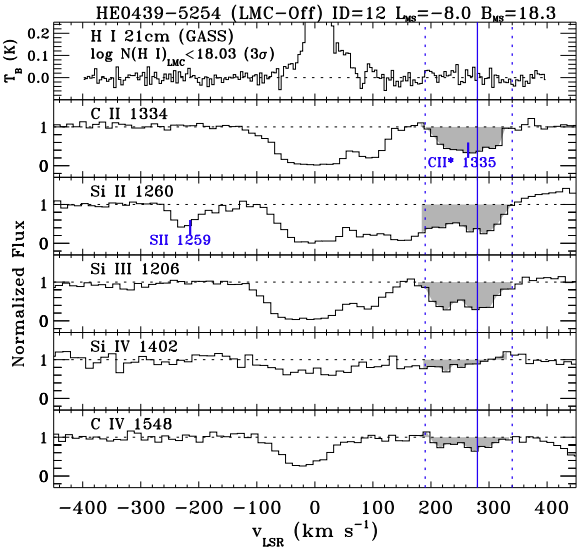
HE0439−5254 (LMC−Off) ID=12 L_MS=−8.0 B_MS=18.3
H I 21cm (GASS)
log N(H I)_LMC<18.03 (3σ)
C II 1334
CII* 1335
Si II 1260
SII 1259
Si III 1206
Si IV 1402
C IV 1548
T_B (K)
Normalized Flux
v_LSR (km s^−1)

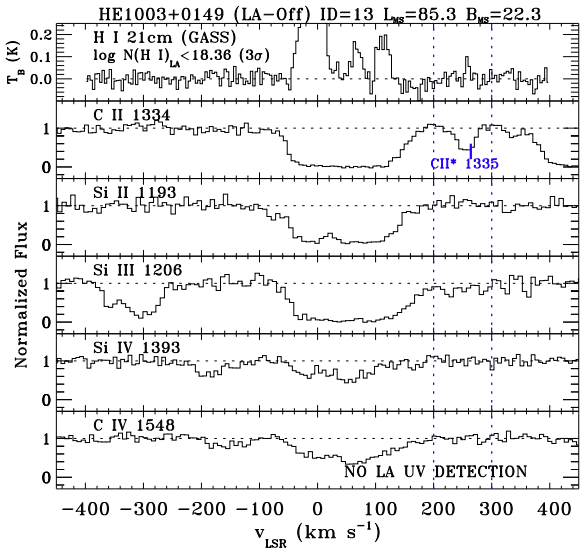
HE1003+0149 (LA−Off) ID=13 L_MS=85.3 B_MS=22.3
H I 21cm (GASS)
log N(H I)_LA<18.36 (3σ)
C II 1334
CII* 1335
Si II 1193
Si III 1206
Si IV 1393
C IV 1548
NO LA UV DETECTION
T_B (K)
Normalized Flux
v_LSR (km s^-1)

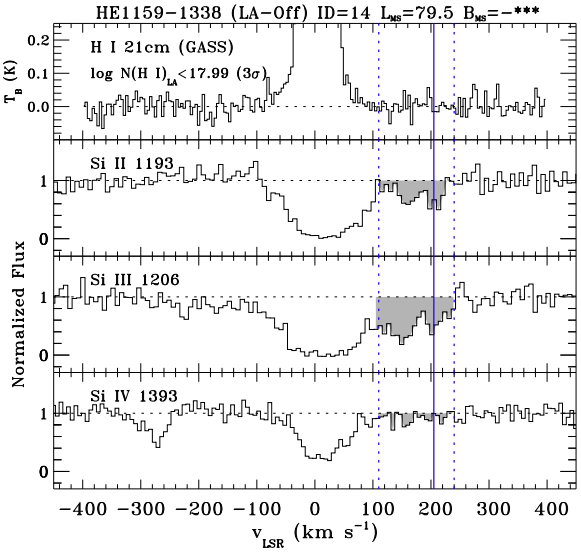
HE1159−1338 (LA−Off) ID=14 L_MS=79.5 B_MS=−***
H I 21cm (GASS)
log N(H I)_LA<17.99 (3σ)
Si II 1193
Si III 1206
Si IV 1393
T_B (K)
Normalized Flux
v_LSR (km s^-1)

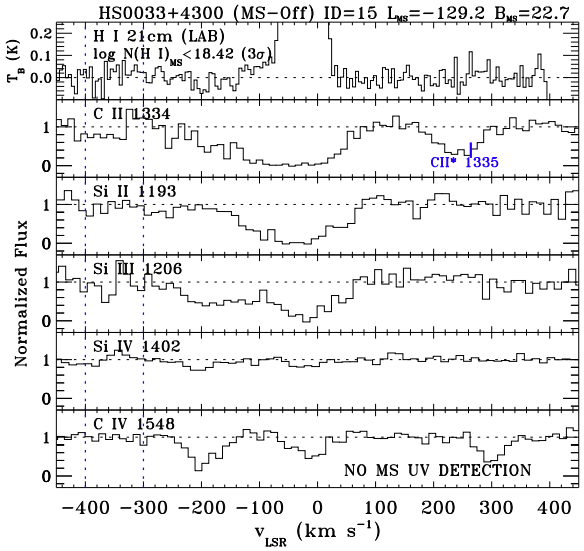
HS0033+4300 (MS−Off) ID=15 L_MS=−129.2 B_MS=22.7
H I 21cm (LAB)
log N(H I)_MS<18.42 (3σ)
C II 1334
CII* 1335
Si II 1193
Si III 1206
Si IV 1402
C IV 1548
NO MS UV DETECTION
T_B (K)
Normalized Flux
v_LSR (km s^-1)

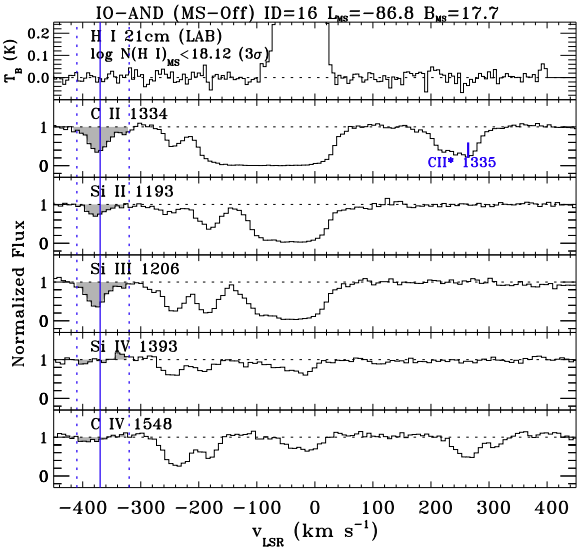
IO−AND (MS−Off) ID=16 L_MS=−86.8 B_MS=17.7
H I 21cm (LAB)
log N(H I)_MS<18.12 (3σ)
C II 1334
CII* 1335
Si II 1193
Si III 1206
Si IV 1393
C IV 1548
T_B (K)
Normalized Flux
v_LSR (km s^-1)

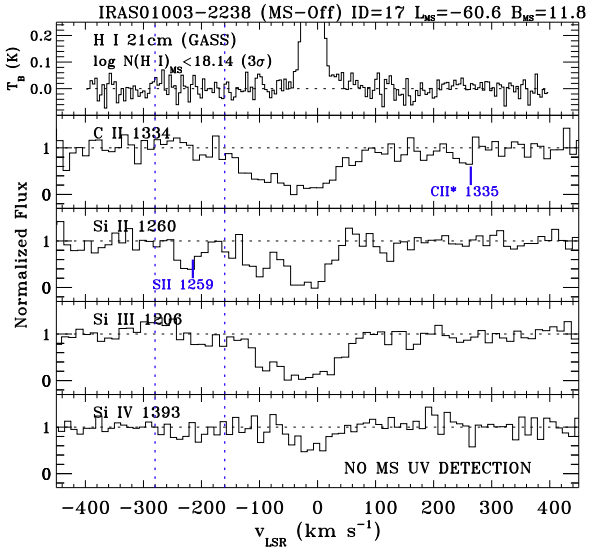
IRAS01003−2238 (MS−Off) ID=17 L_MS=−60.6 B_MS=11.8
H I 21cm (GASS)
log N(H I)_MS<18.14 (3σ)
C II 1334
CII* 1335
Si II 1260
SII 1259
Si III 1206
Si IV 1393
NO MS UV DETECTION
T_B (K)
Normalized Flux
v_LSR (km s^-1)

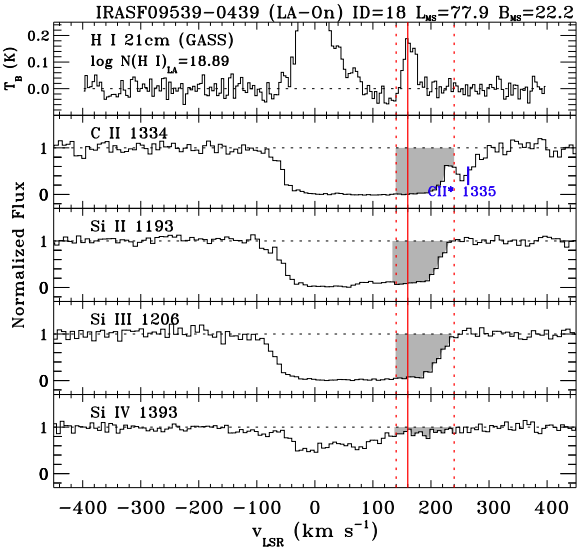
IRASF09539−0439 (LA−On) ID=18 L_MS=77.9 B_MS=22.2
H I 21cm (GASS)
log N(H I)_LA=18.89
C II 1334
CII* 1335
Si II 1193
Si III 1206
Si IV 1393
T_B (K)
Normalized Flux
v_LSR (km s^-1)

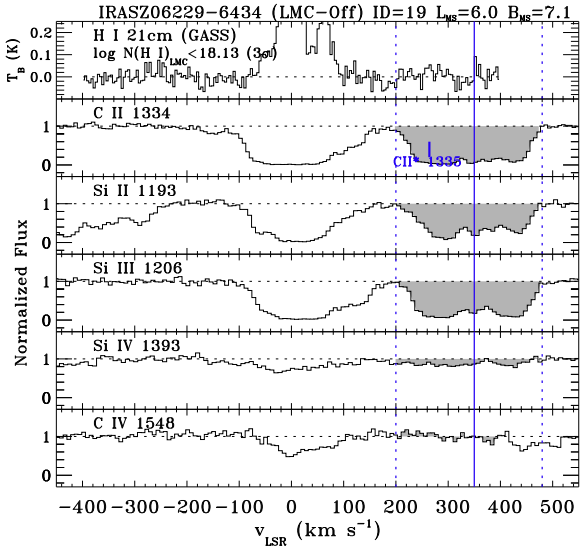
IRASZ06229−6434 (LMC−Off) ID=19 L_MS=6.0 B_MS=7.1
H I 21cm (GASS)
log N(H I)_LMC<18.13 (3σ)
C II 1334
CII* 1335
Si II 1193
Si III 1206
Si IV 1393
C IV 1548
T_B (K)
Normalized Flux
v_LSR (km s^-1)

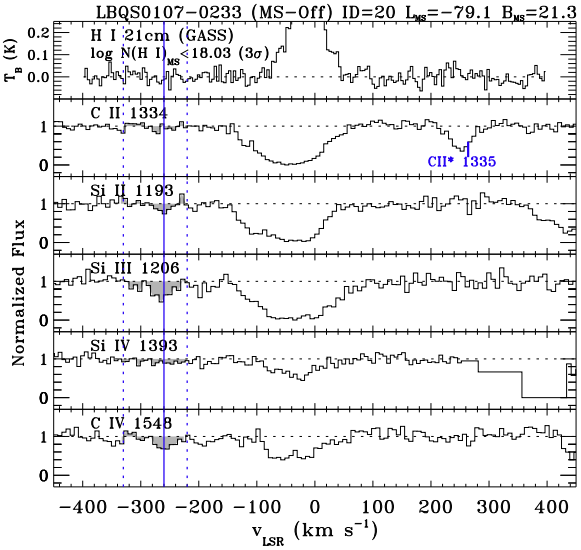
LBQS0107−0233 (MS−Off) ID=20 L_MS=−79.1 B_MS=21.3
H I 21cm (GASS)
log N(H I)_MS<18.03 (3σ)
C II 1334
CII* 1335
Si II 1193
Si III 1206
Si IV 1393
C IV 1548
T_B (K)
Normalized Flux
v_LSR (km s^-1)

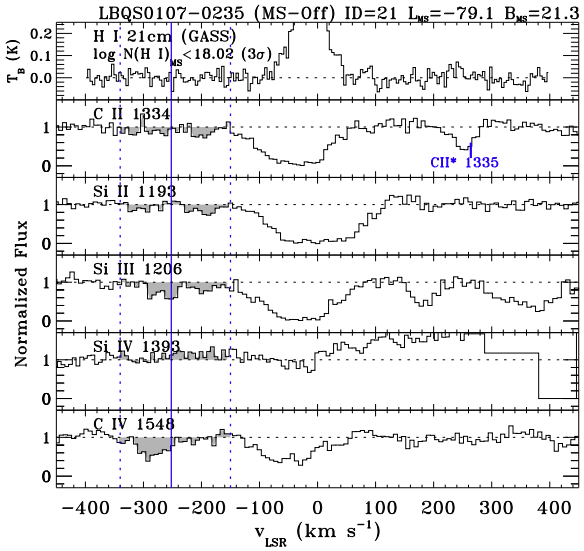
LBQS0107−0235 (MS−Off) ID=21 L_MS=−79.1 B_MS=21.3
H I 21cm (GASS)
log N(H I)_MS<18.02 (3σ)
C II 1334
CII* 1335
Si II 1193
Si III 1206
Si IV 1393
C IV 1548
T_B (K)
Normalized Flux
v_LSR (km s^-1)

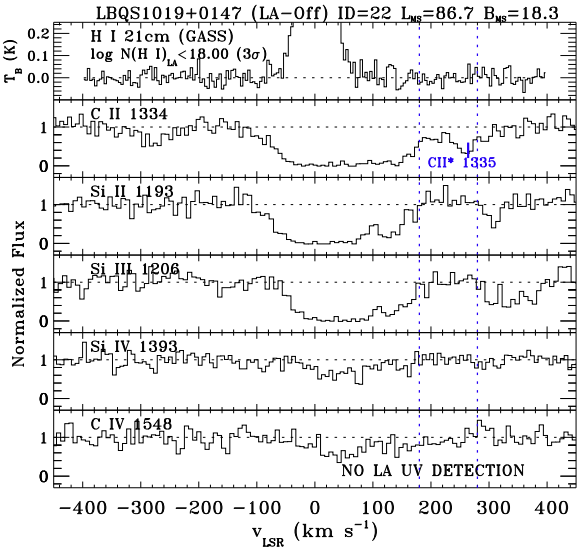
LBQS1019+0147 (LA−Off) ID=22 L_MS=86.7 B_MS=18.3
H I 21cm (GASS)
log N(H I)_LA<18.00 (3σ)
C II 1334
CII* 1335
Si II 1193
Si III 1206
Si IV 1393
C IV 1548
NO LA UV DETECTION
T_B (K)
Normalized Flux
v_LSR (km s^-1)

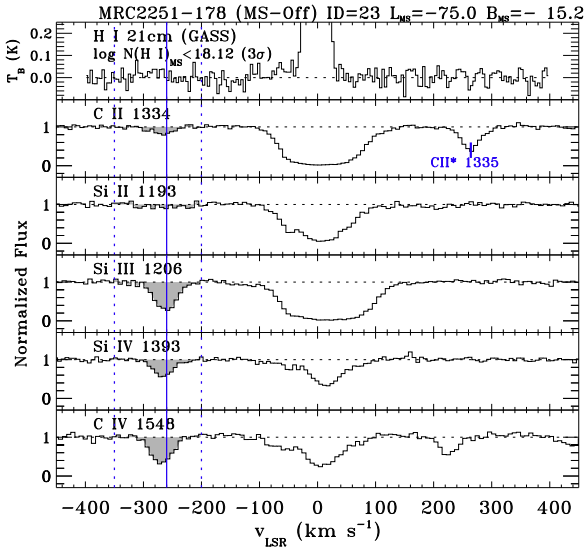
MRC2251−178 (MS−Off) ID=23 L_MS=−75.0 B_MS=− 15.2
H I 21cm (GASS)
log N(H I)_MS<18.12 (3σ)
C II 1334
CII* 1335
Si II 1193
Si III 1206
Si IV 1393
C IV 1548
T_B (K)
Normalized Flux
v_LSR (km s^-1)

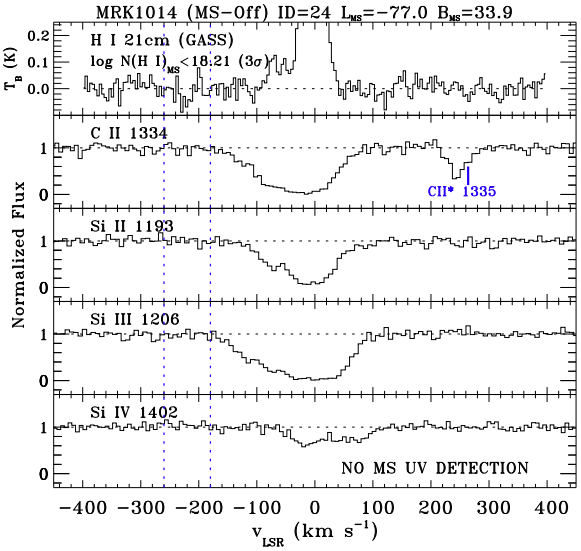
MRK1014 (MS−Off) ID=24 L_MS=−77.0 B_MS=33.9
H I 21cm (GASS)
log N(H I)_MS<18.21 (3σ)
C II 1334
CII* 1335
Si II 1193
Si III 1206
Si IV 1402
NO MS UV DETECTION
T_B (K)
Normalized Flux
v_LSR (km s^-1)

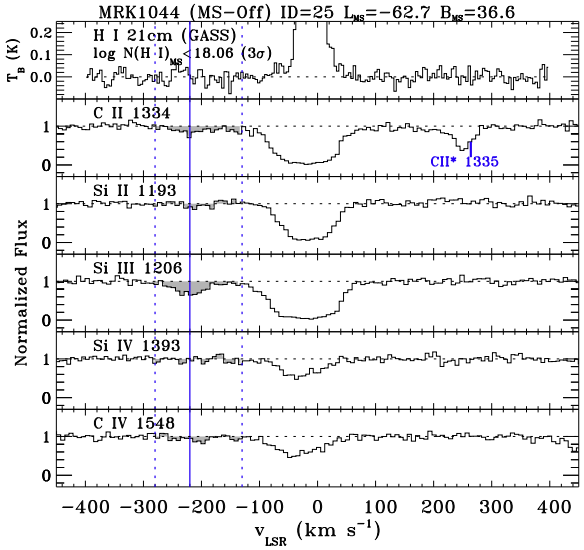
MRK1044 (MS−Off) ID=25 L_MS=−62.7 B_MS=36.6
H I 21cm (GASS)
log N(H I)_MS<18.06 (3σ)
T_B (K)
C II 1334
CII* 1335
Si II 1193
Si III 1206
Si IV 1393
C IV 1548
Normalized Flux
v_LSR (km s^−1)

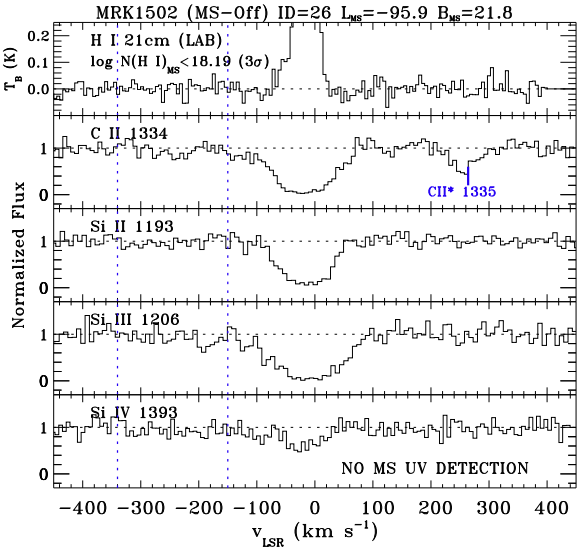
MRK1502 (MS−Off) ID=26 L_MS=−95.9 B_MS=21.8
H I 21cm (LAB)
log N(H I)_MS<18.19 (3σ)
T_B (K)
C II 1334
CII* 1335
Si II 1193
Si III 1206
Si IV 1393
NO MS UV DETECTION
Normalized Flux
v_LSR (km s^−1)

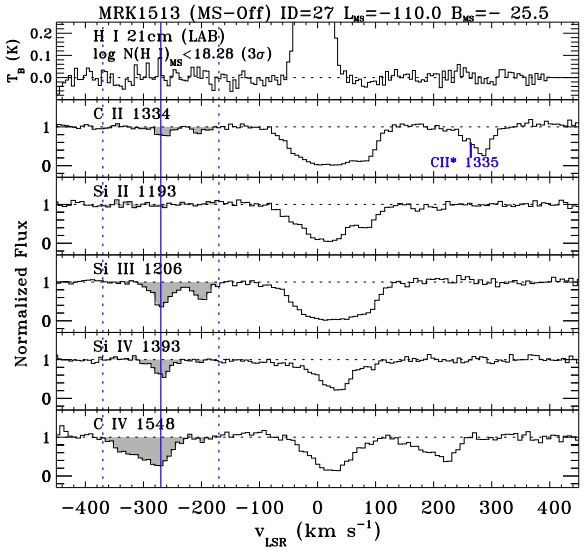
MRK1513 (MS−Off) ID=27 L_MS=−110.0 B_MS=− 25.5
H I 21cm (LAB)
log N(H I)_MS<18.28 (3σ)
T_B (K)
C II 1334
CII* 1335
Si II 1193
Si III 1206
Si IV 1393
C IV 1548
Normalized Flux
v_LSR (km s^−1)

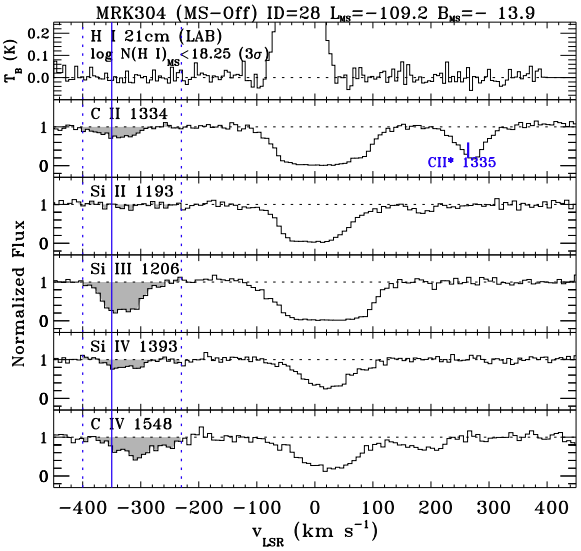
MRK304 (MS−Off) ID=28 L_MS=−109.2 B_MS=− 13.9
H I 21cm (LAB)
log N(H I)_MS<18.25 (3σ)
T_B (K)
C II 1334
CII* 1335
Si II 1193
Si III 1206
Si IV 1393
C IV 1548
Normalized Flux
v_LSR (km s^−1)

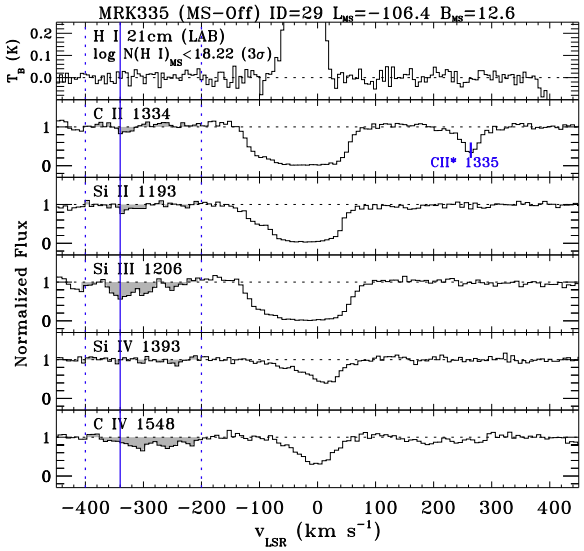
MRK335 (MS−Off) ID=29 L_MS=−106.4 B_MS=12.6
H I 21cm (LAB)
log N(H I)_MS<18.22 (3σ)
T_B (K)
C II 1334
CII* 1335
Si II 1193
Si III 1206
Si IV 1393
C IV 1548
Normalized Flux
v_LSR (km s^−1)

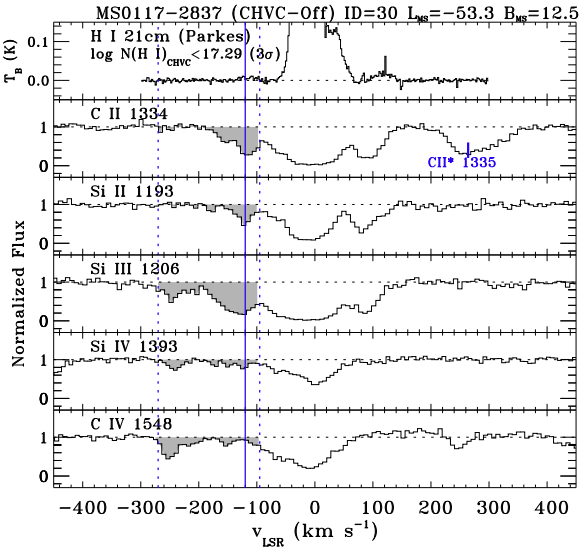
MS0117−2837 (CHVC−Off) ID=30 L_MS=−53.3 B_MS=12.5
H I 21cm (Parkes)
log N(H I)_CHVC<17.29 (3σ)
T_B (K)
C II 1334
CII* 1335
Si II 1193
Si III 1206
Si IV 1393
C IV 1548
Normalized Flux
v_LSR (km s^−1)

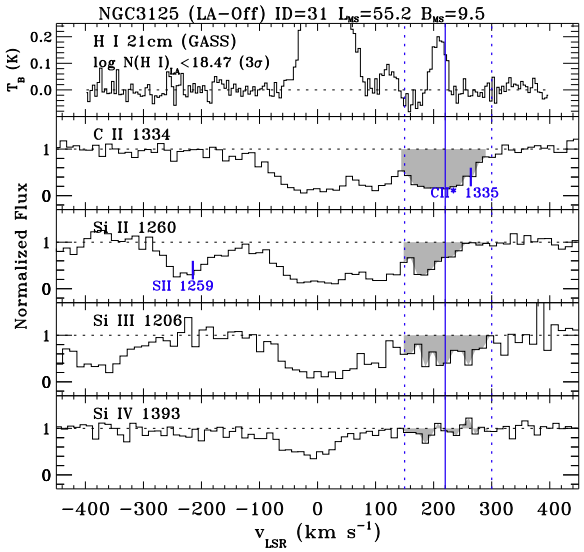
NGC3125 (LA−Off) ID=31 L_MS=55.2 B_MS=9.5
H I 21cm (GASS)
log N(H I)_LA<18.47 (3σ)
C II 1334
CII* 1335
Si II 1260
SII 1259
Si III 1206
Si IV 1393
T_B (K)
Normalized Flux
v_LSR (km s^-1)

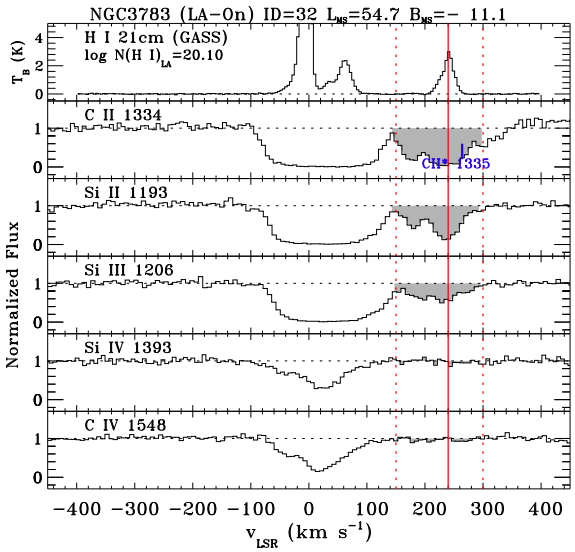
NGC3783 (LA−On) ID=32 L_MS=54.7 B_MS=− 11.1
H I 21cm (GASS)
log N(H I)_LA=20.10
C II 1334
CII* 1335
Si II 1193
Si III 1206
Si IV 1393
C IV 1548
T_B (K)
Normalized Flux
v_LSR (km s^-1)

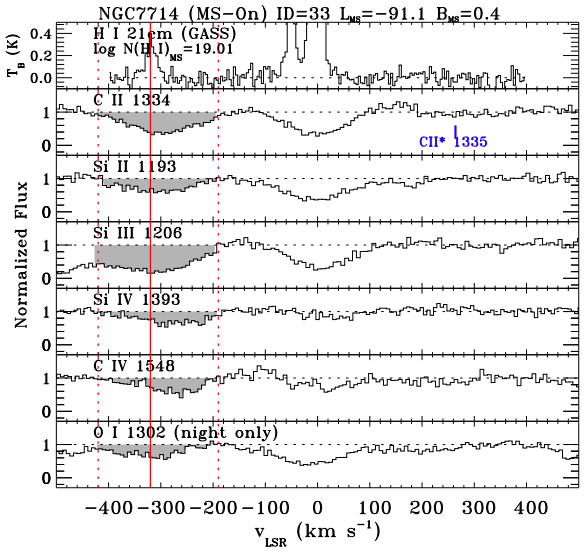
NGC7714 (MS−On) ID=33 L_MS=−91.1 B_MS=0.4
H I 21cm (GASS)
log N(H I)_MS=19.01
C II 1334
CII* 1335
Si II 1193
Si III 1206
Si IV 1393
C IV 1548
O I 1302 (night only)
T_B (K)
Normalized Flux
v_LSR (km s^-1)

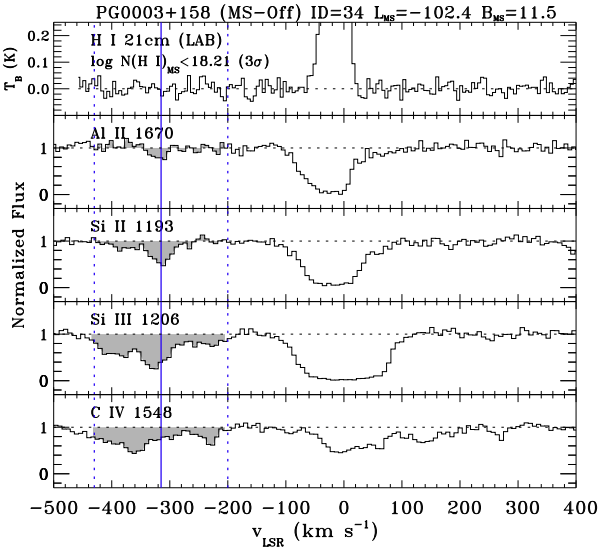
PG0003+158 (MS−Off) ID=34 L_MS=−102.4 B_MS=11.5
H I 21cm (LAB)
log N(H I)_MS<18.21 (3σ)
Al II 1670
Si II 1193
Si III 1206
C IV 1548
T_B (K)
Normalized Flux
v_LSR (km s^-1)

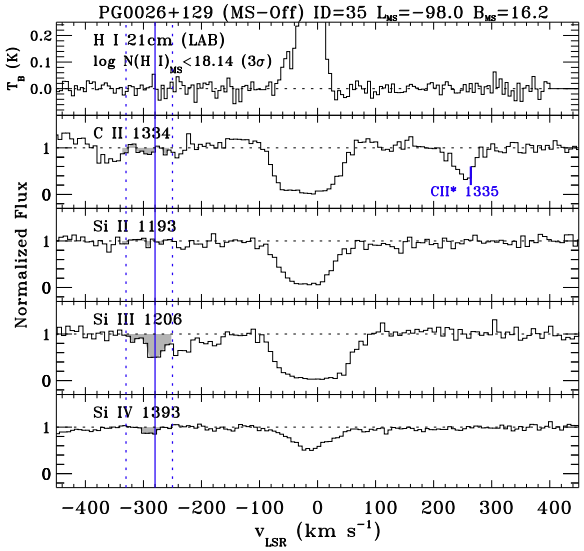
PG0026+129 (MS−Off) ID=35 L_MS=−98.0 B_MS=16.2
H I 21cm (LAB)
log N(H I)_MS<18.14 (3σ)
C II 1334
CII* 1335
Si II 1193
Si III 1206
Si IV 1393
T_B (K)
Normalized Flux
v_LSR (km s^-1)

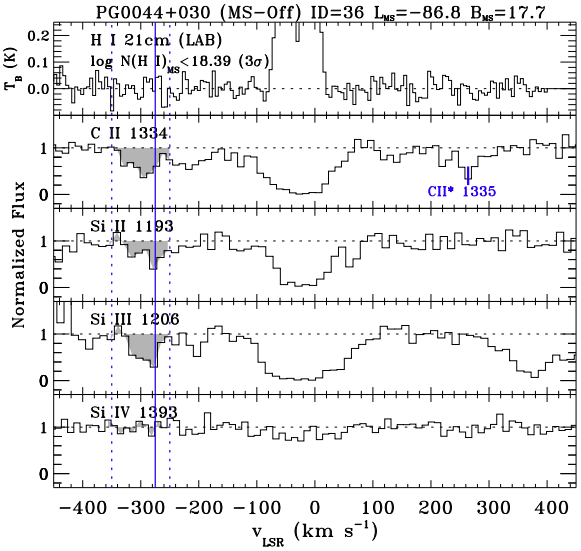
PG0044+030 (MS−Off) ID=36 L_MS=−86.8 B_MS=17.7
H I 21cm (LAB)
log N(H I)_MS<18.39 (3σ)
C II 1334
CII* 1335
Si II 1193
Si III 1206
Si IV 1393
T_B (K)
Normalized Flux
v_LSR (km s^-1)

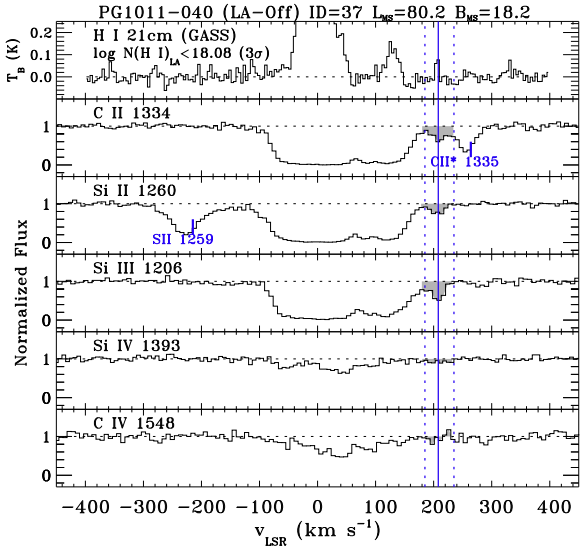
PG1011−040 (LA−Off) ID=37 L_MS=80.2 B_MS=18.2
H I 21cm (GASS)
log N(H I)_LA<18.08 (3σ)
C II 1334
CII* 1335
Si II 1260
SII 1259
Si III 1206
Si IV 1393
C IV 1548
T_B (K)
Normalized Flux
v_LSR (km s^−1)

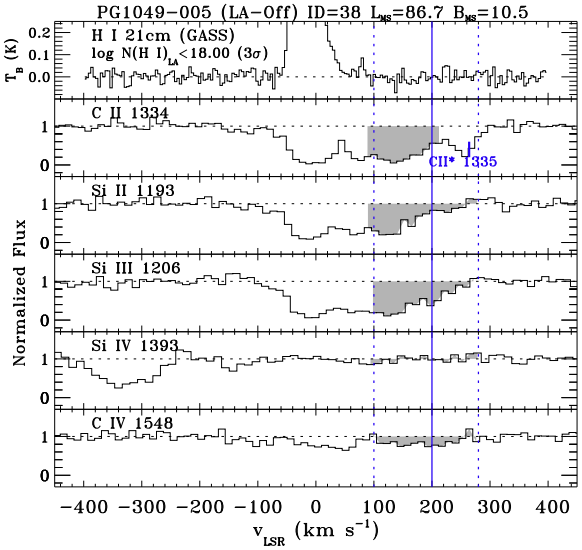
PG1049−005 (LA−Off) ID=38 L_MS=86.7 B_MS=10.5
H I 21cm (GASS)
log N(H I)_LA<18.00 (3σ)
C II 1334
CII* 1335
Si II 1193
Si III 1206
Si IV 1393
C IV 1548
T_B (K)
Normalized Flux
v_LSR (km s^−1)

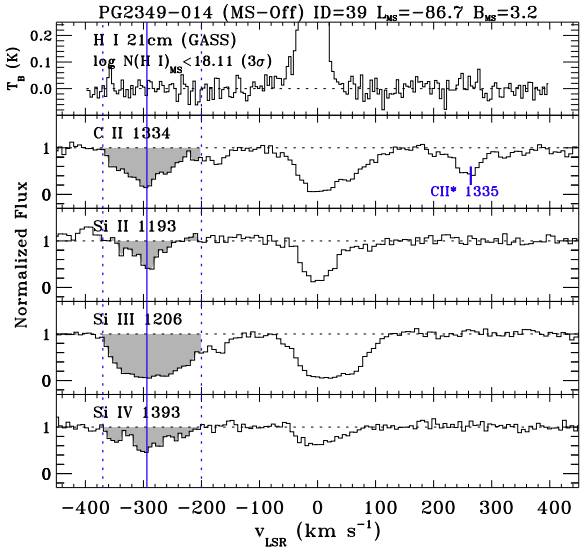
PG2349−014 (MS−Off) ID=39 L_MS=−86.7 B_MS=3.2
H I 21cm (GASS)
log N(H I)_MS<18.11 (3σ)
C II 1334
CII* 1335
Si II 1193
Si III 1206
Si IV 1393
T_B (K)
Normalized Flux
v_LSR (km s^−1)

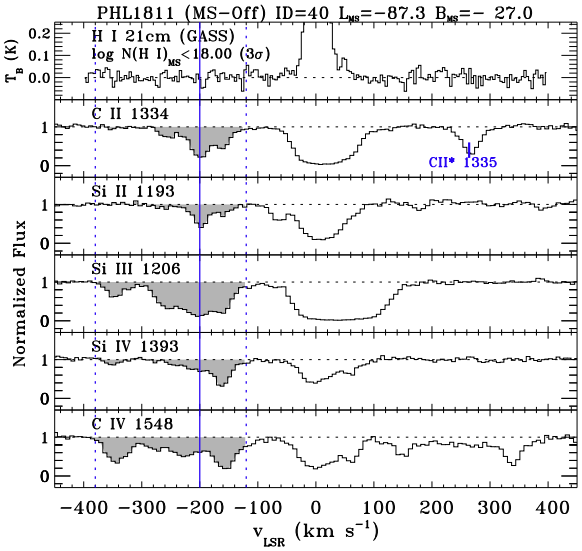
PHL1811 (MS−Off) ID=40 L_MS=−87.3 B_MS=− 27.0
H I 21cm (GASS)
log N(H I)_MS<18.00 (3σ)
C II 1334
CII* 1335
Si II 1193
Si III 1206
Si IV 1393
C IV 1548
T_B (K)
Normalized Flux
v_LSR (km s^−1)

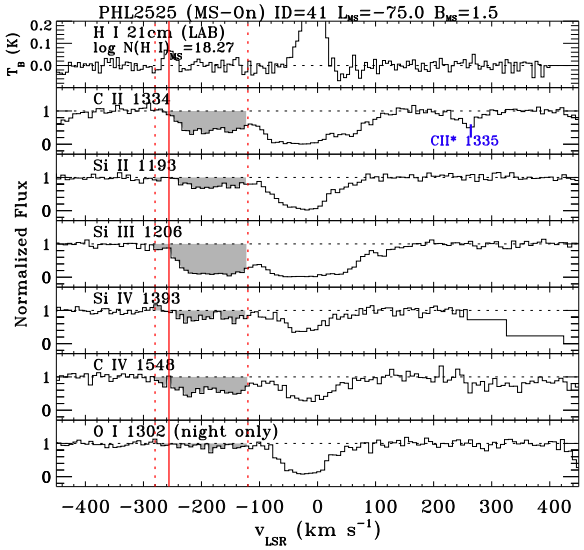
PHL2525 (MS−On) ID=41 L_MS=−75.0 B_MS=1.5
H I 21cm (LAB)
log N(H I)_MS=18.27
C II 1334
CII* 1335
Si II 1193
Si III 1206
Si IV 1393
C IV 1548
O I 1302 (night only)
T_B (K)
Normalized Flux
v_LSR (km s^−1)

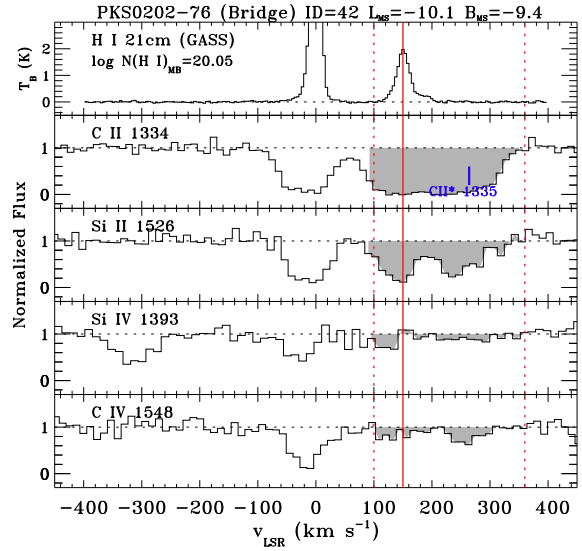
PKS0202−76 (Bridge) ID=42 L_MS=−10.1 B_MS=−9.4
H I 21cm (GASS)
log N(H I)_MB=20.05
C II 1334
CII* 1335
Si II 1526
Si IV 1393
C IV 1548
T_B (K)
Normalized Flux
v_LSR (km s^−1)

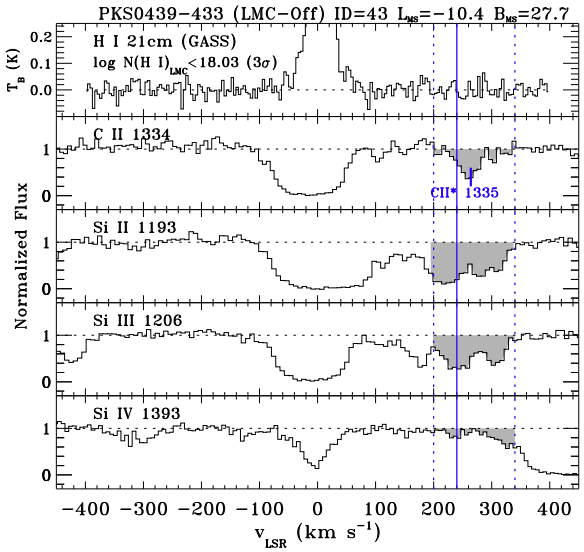
PKS0439−433 (LMC−Off) ID=43 L_MS=−10.4 B_MS=27.7
H I 21cm (GASS)
log N(H I)_LMC<18.03 (3σ)
C II 1334
CII* 1335
Si II 1193
Si III 1206
Si IV 1393
T_B (K)
Normalized Flux
v_LSR (km s^−1)

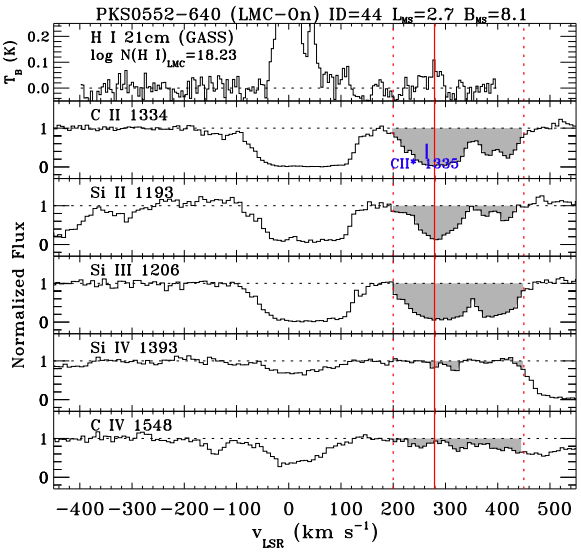
PKS0552−640 (LMC−On) ID=44 L_MS=2.7 B_MS=8.1
H I 21cm (GASS)
log N(H I)_LMC=18.23
C II 1334
CII* 1335
Si II 1193
Si III 1206
Si IV 1393
C IV 1548
T_B (K)
Normalized Flux
v_LSR (km s^−1)

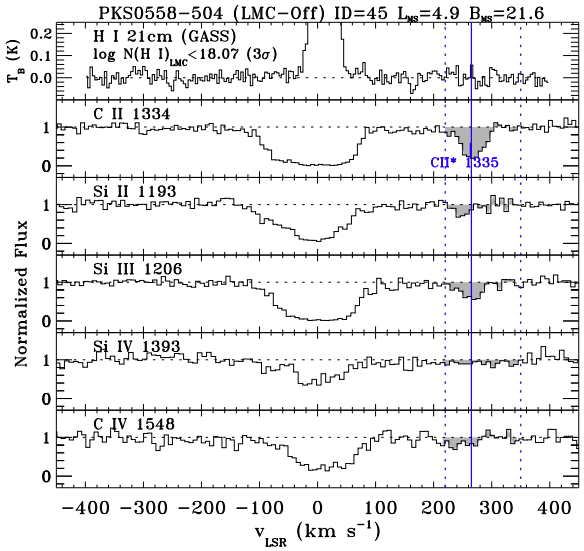
PKS0558−504 (LMC−Off) ID=45 L_MS=4.9 B_MS=21.6
H I 21cm (GASS)
log N(H I)_LMC<18.07 (3σ)
C II 1334
CII* 1335
Si II 1193
Si III 1206
Si IV 1393
C IV 1548
T_B (K)
Normalized Flux
v_LSR (km s^−1)

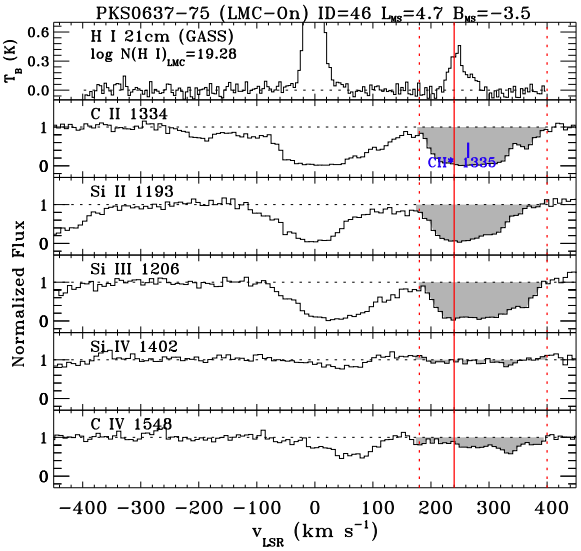
PKS0637−75 (LMC−On) ID=46 L_MS=4.7 B_MS=−3.5
H I 21cm (GASS)
log N(H I)_LMC=19.28
C II 1334
CII* 1335
Si II 1193
Si III 1206
Si IV 1402
C IV 1548
T_B (K)
Normalized Flux
v_LSR (km s^−1)

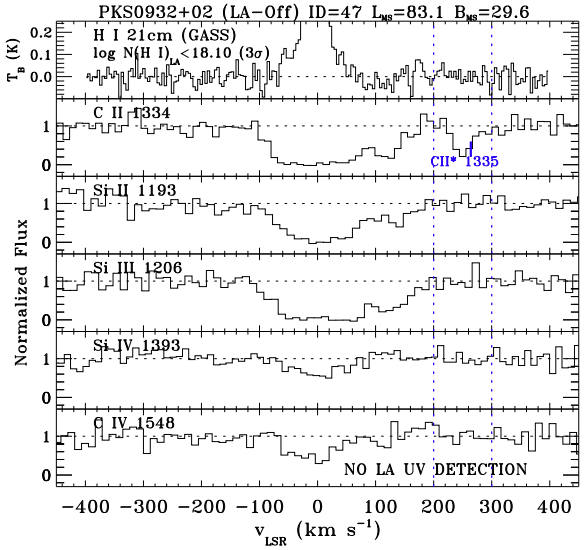
PKS0932+02 (LA−Off) ID=47 L_MS=83.1 B_MS=29.6
H I 21cm (GASS)
log N(H I)_LA<18.10 (3σ)
C II 1334
CII* 1335
Si II 1193
Si III 1206
Si IV 1393
C IV 1548
NO LA UV DETECTION
T_B (K)
Normalized Flux
v_LSR (km s^−1)

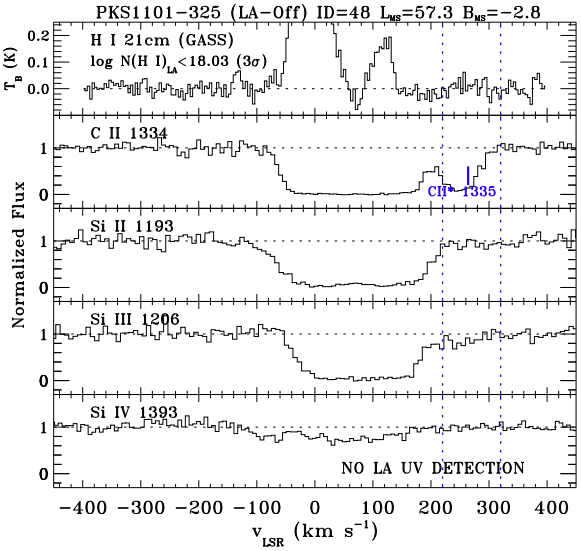
PKS1101−325 (LA−Off) ID=48 L_MS=57.3 B_MS=−2.8
H I 21cm (GASS)
log N(H I)_LA<18.03 (3σ)
C II 1334
CII* 1335
Si II 1193
Si III 1206
Si IV 1393
NO LA UV DETECTION
T_B (K)
Normalized Flux
v_LSR (km s^−1)

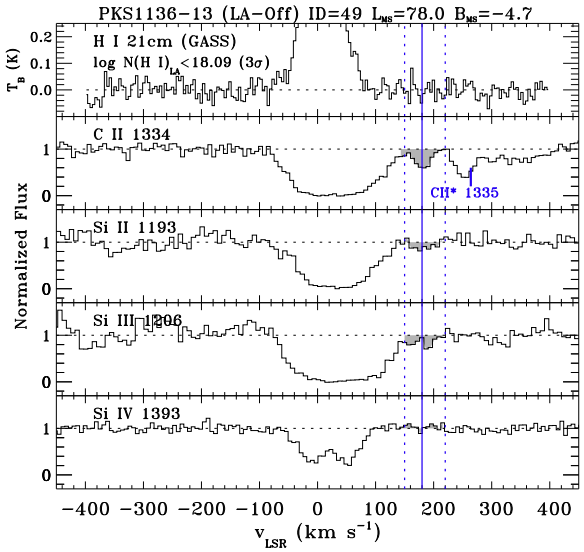
PKS1136−13 (LA−Off) ID=49 L_MS=78.0 B_MS=−4.7
H I 21cm (GASS)
log N(H I)_LA<18.09 (3σ)
C II 1334
CII* 1335
Si II 1193
Si III 1206
Si IV 1393
T_B (K)
Normalized Flux
v_LSR (km s^−1)

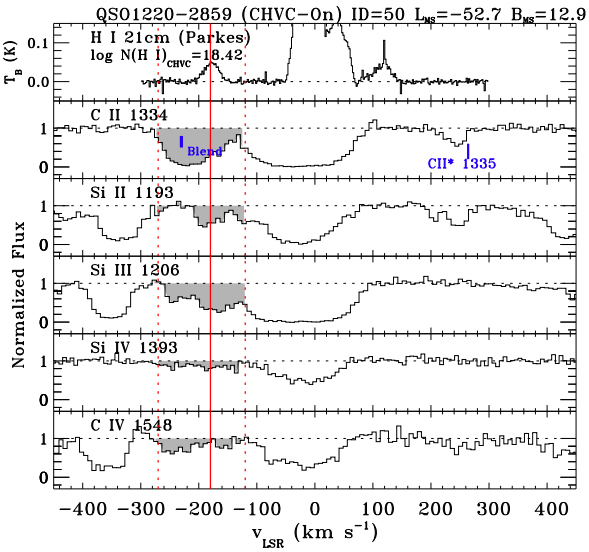
QSO1220−2859 (CHVC−On) ID=50 L_MS=−52.7 B_MS=12.9
H I 21cm (Parkes)
log N(H I)_CHVC=18.42
C II 1334
Blend
CII* 1335
Si II 1193
Si III 1206
Si IV 1393
C IV 1548
T_B (K)
Normalized Flux
v_LSR (km s^−1)

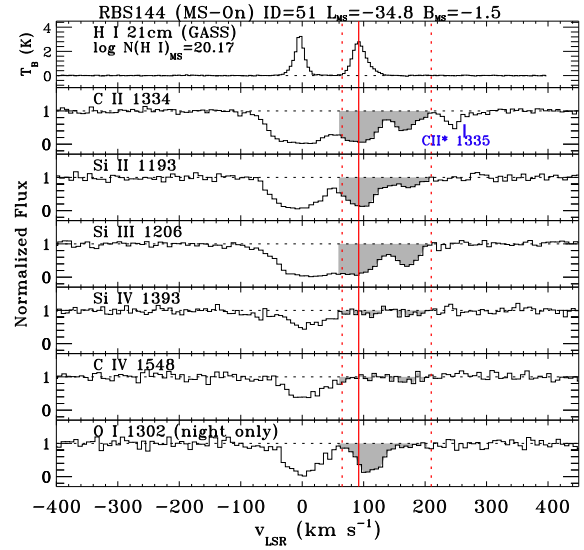
RBS144 (MS−On) ID=51 L_MS=−34.8 B_MS=−1.5
H I 21cm (GASS)
log N(H I)_MS=20.17
C II 1334
CII* 1335
Si II 1193
Si III 1206
Si IV 1393
C IV 1548
O I 1302 (night only)
T_B (K)
Normalized Flux
v_LSR (km s^−1)

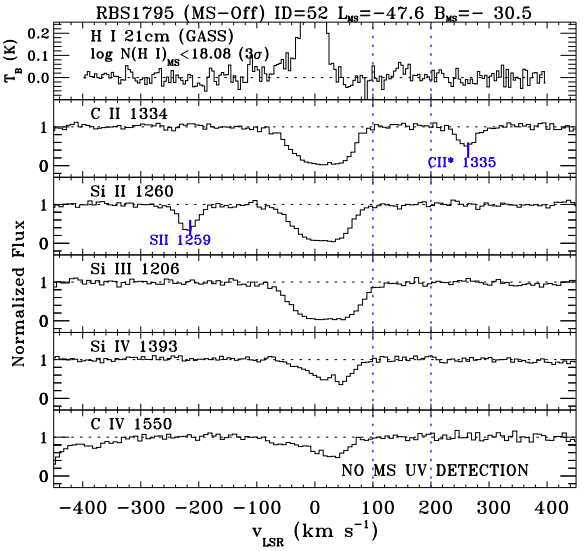
RBS1795 (MS−Off) ID=52 L_MS=−47.6 B_MS=− 30.5
H I 21cm (GASS)
log N(H I)_MS<18.08 (3σ)
C II 1334
CII* 1335
Si II 1260
SII 1259
Si III 1206
Si IV 1393
C IV 1550
NO MS UV DETECTION
T_B (K)
Normalized Flux
v_LSR (km s^−1)

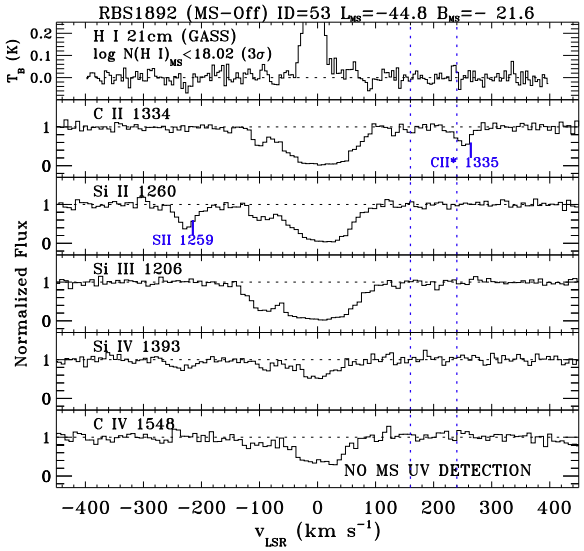
RBS1892 (MS−Off) ID=53 L_MS=−44.8 B_MS=− 21.6
H I 21cm (GASS)
log N(H I)_MS<18.02 (3σ)
C II 1334
CII* 1335
Si II 1260
SII 1259
Si III 1206
Si IV 1393
C IV 1548
NO MS UV DETECTION
T_B (K)
Normalized Flux
v_LSR (km s^−1)

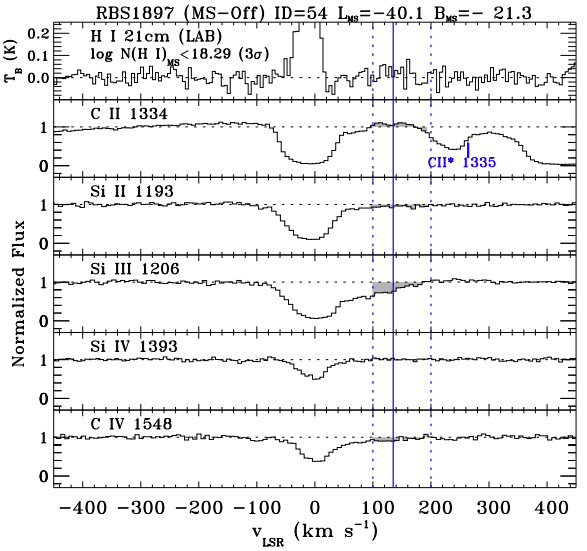
RBS1897 (MS−Off) ID=54 L_MS=−40.1 B_MS=− 21.3
H I 21cm (LAB)
log N(H I)_MS<18.29 (3σ)
C II 1334
CII* 1335
Si II 1193
Si III 1206
Si IV 1393
C IV 1548
T_B (K)
Normalized Flux
v_LSR (km s^−1)

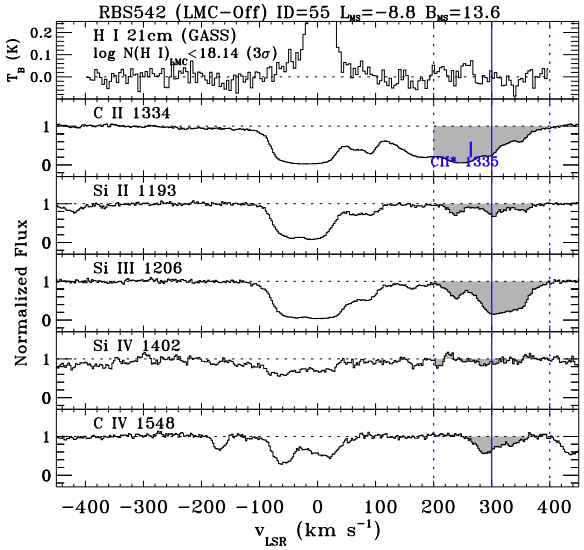
RBS542 (LMC−Off) ID=55 L_MS=−8.8 B_MS=13.6
H I 21cm (GASS)
log N(H I)_LMC<18.14 (3σ)
T_B (K)
C II 1334
CII* 1335
Si II 1193
Si III 1206
Si IV 1402
C IV 1548
Normalized Flux
v_LSR (km s^−1)

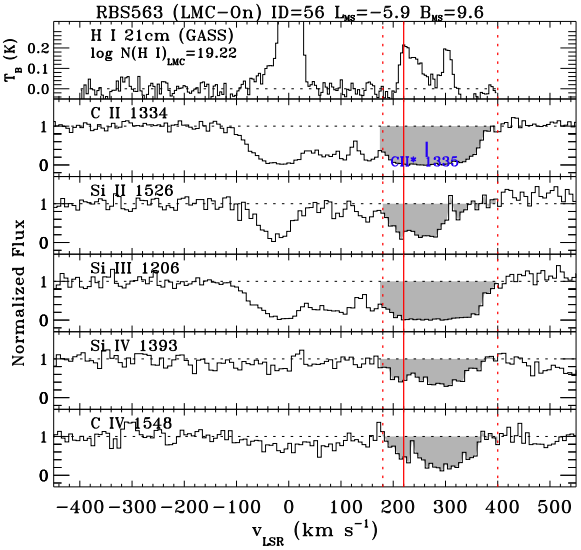
RBS563 (LMC−On) ID=56 L_MS=−5.9 B_MS=9.6
H I 21cm (GASS)
log N(H I)_LMC=19.22
T_B (K)
C II 1334
CII* 1335
Si II 1526
Si III 1206
Si IV 1393
C IV 1548
Normalized Flux
v_LSR (km s^−1)

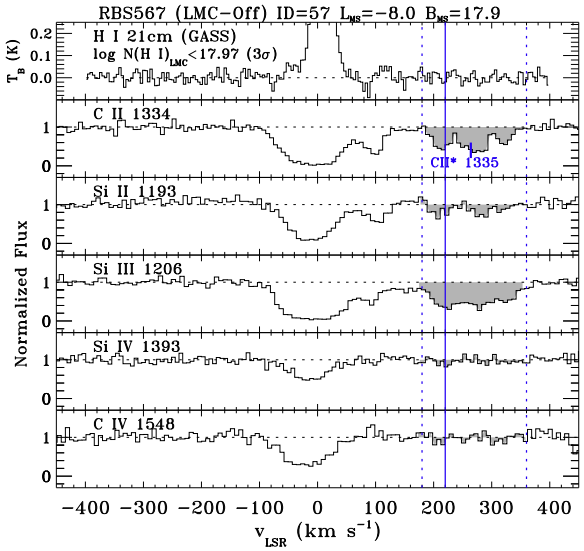
RBS567 (LMC−Off) ID=57 L_MS=−8.0 B_MS=17.9
H I 21cm (GASS)
log N(H I)_LMC<17.97 (3σ)
T_B (K)
C II 1334
CII* 1335
Si II 1193
Si III 1206
Si IV 1393
C IV 1548
Normalized Flux
v_LSR (km s^−1)

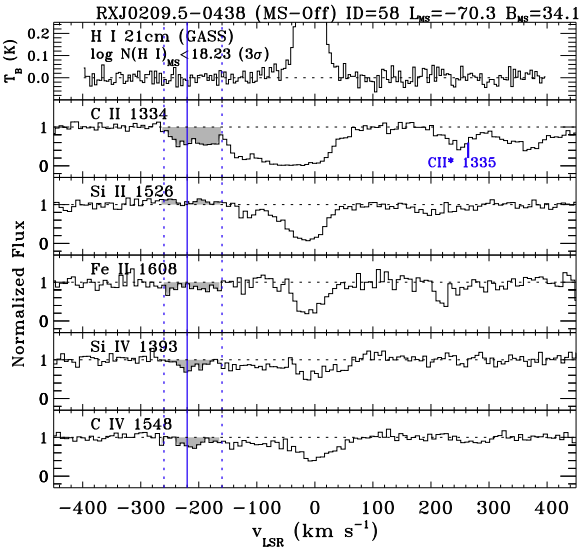
RXJ0209.5−0438 (MS−Off) ID=58 L_MS=−70.3 B_MS=34.1
H I 21cm (GASS)
log N(H I)_MS<18.23 (3σ)
T_B (K)
C II 1334
CII* 1335
Si II 1526
Fe II 1608
Si IV 1393
C IV 1548
Normalized Flux
v_LSR (km s^−1)

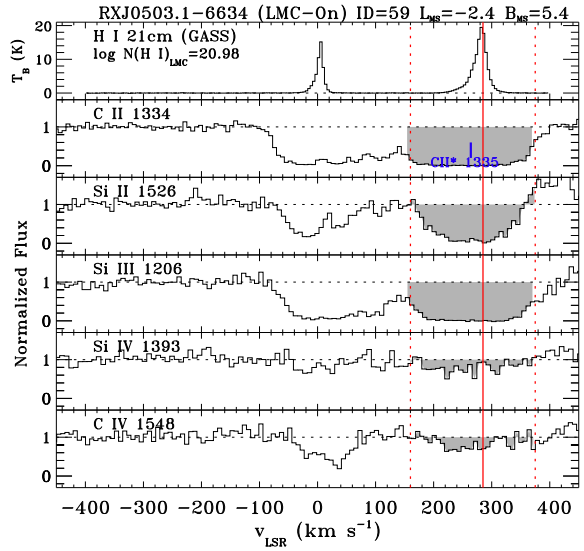
RXJ0503.1−6634 (LMC−On) ID=59 L_MS=−2.4 B_MS=5.4
H I 21cm (GASS)
log N(H I)_LMC=20.98
T_B (K)
C II 1334
CII* 1335
Si II 1526
Si III 1206
Si IV 1393
C IV 1548
Normalized Flux
v_LSR (km s^−1)

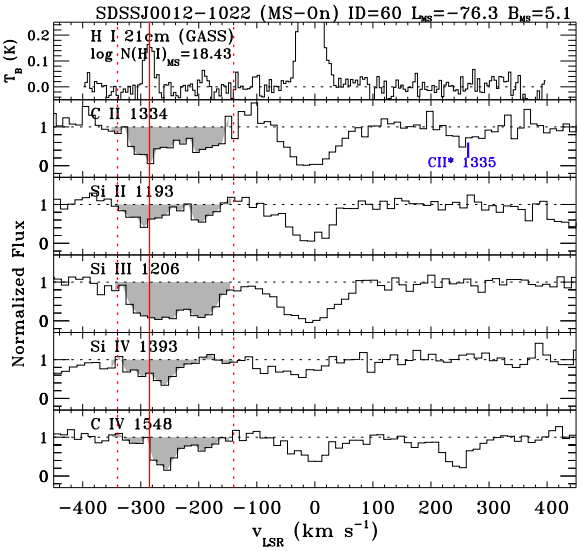
SDSSJ0012−1022 (MS−On) ID=60 L_MS=−76.3 B_MS=5.1
H I 21cm (GASS)
log N(H I)_MS=18.43
T_B (K)
C II 1334
CII* 1335
Si II 1193
Si III 1206
Si IV 1393
C IV 1548
Normalized Flux
v_LSR (km s^−1)

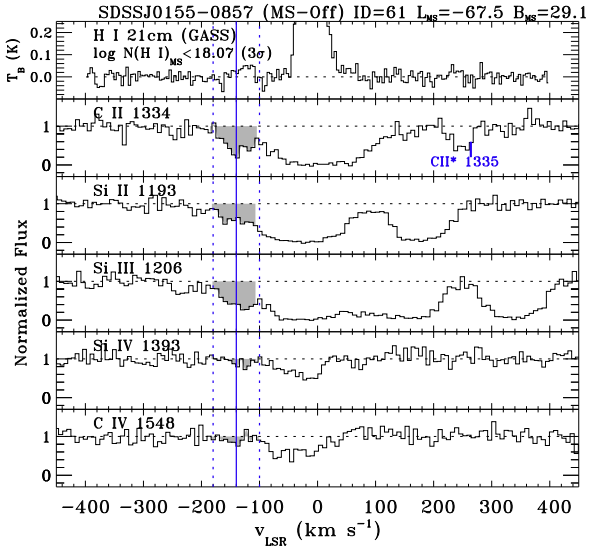
SDSSJ0155−0857 (MS−Off) ID=61 L_MS=−67.5 B_MS=29.1
H I 21cm (GASS)
log N(H I)_MS<18.07 (3σ)
T_B (K)
C II 1334
CII* 1335
Si II 1193
Si III 1206
Si IV 1393
C IV 1548
Normalized Flux
v_LSR (km s^−1)

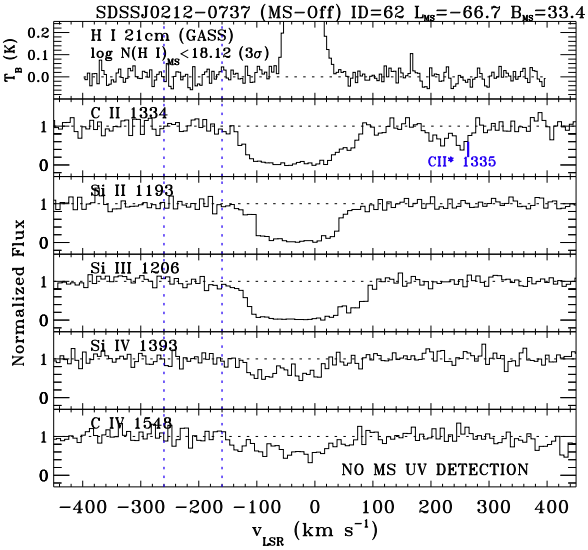
SDSSJ0212−0737 (MS−Off) ID=62 L_MS=−66.7 B_MS=33.4
H I 21cm (GASS)
log N(H I)_MS<18.12 (3σ)
T_B (K)
C II 1334
CII* 1335
Si II 1193
Si III 1206
Si IV 1393
C IV 1548
NO MS UV DETECTION
Normalized Flux
v_LSR (km s^−1)

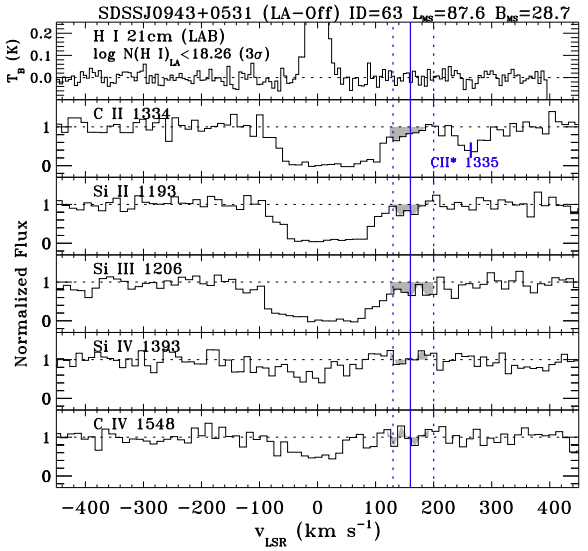
SDSSJ0943+0531 (LA−Off) ID=63 L_MS=87.6 B_MS=28.7
H I 21cm (LAB)
log N(H I)_LA<18.26 (3σ)
T_B (K)
C II 1334
CII* 1335
Si II 1193
Si III 1206
Si IV 1393
C IV 1548
Normalized Flux
v_LSR (km s^−1)

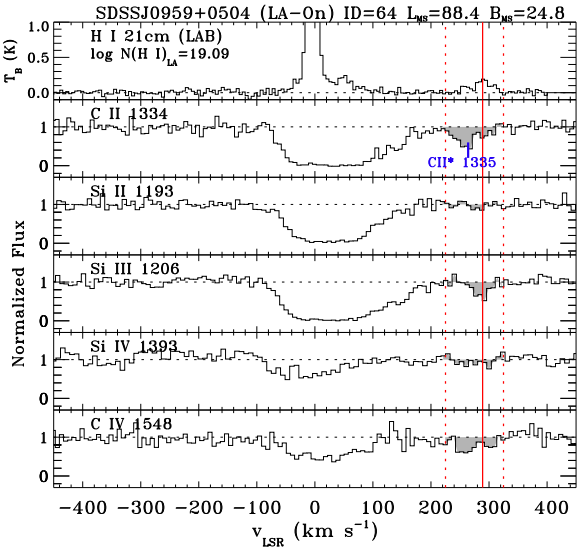
SDSSJ0959+0504 (LA−On) ID=64 L_MS=88.4 B_MS=24.8
H I 21cm (LAB)
log N(H I)_LA=19.09
T_B (K)
C II 1334
CII* 1335
Si II 1193
Si III 1206
Si IV 1393
C IV 1548
Normalized Flux
v_LSR (km s^−1)

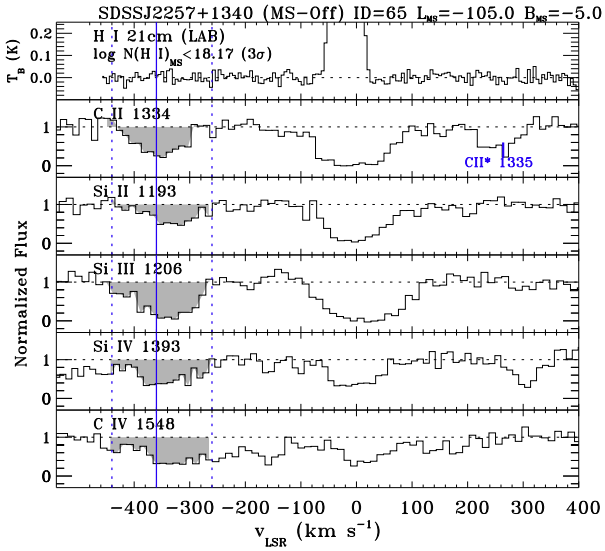
SDSSJ2257+1340 (MS−Off) ID=65 L_MS=−105.0 B_MS=−5.0
H I 21cm (LAB)
log N(H I)_MS<18.17 (3σ)
T_B (K)
C II 1334
CII* 1335
Si II 1193
Si III 1206
Si IV 1393
C IV 1548
Normalized Flux
v_LSR (km s^−1)

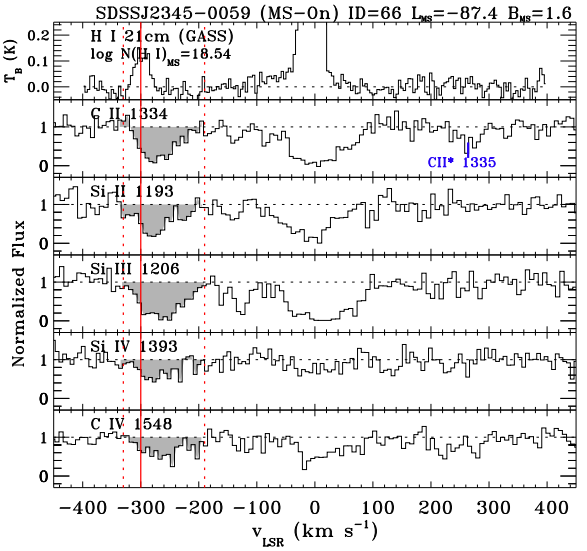
SDSSJ2345−0059 (MS−On) ID=66 L_MS=−87.4 B_MS=1.6
H I 21cm (GASS)
log N(H I)_MS=18.54
T_B (K)
C II 1334
CII* 1335
Si II 1193
Si III 1206
Si IV 1393
C IV 1548
Normalized Flux
v_LSR (km s^−1)

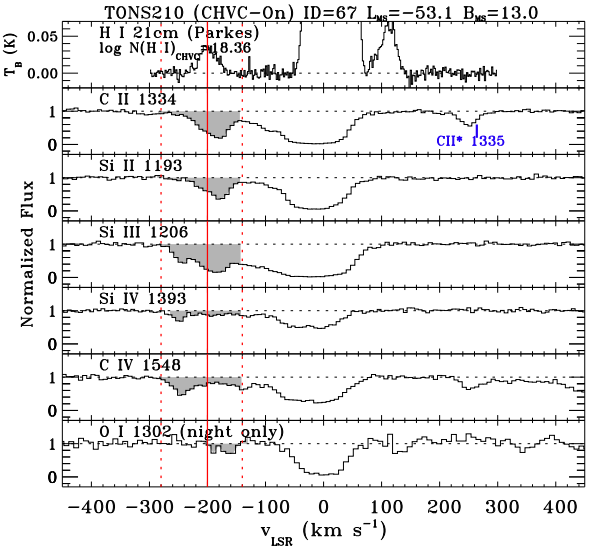
TONS210 (CHVC−0n) ID=67 L_MS=−53.1 B_MS=13.0
H I 21cm (Parkes)
log N(H I)_CHVC=18.36
C II 1334
CII* 1335
Si II 1193
Si III 1206
Si IV 1393
C IV 1548
O I 1302 (night only)
T_B (K)
Normalized Flux
v_LSR (km s^−1)

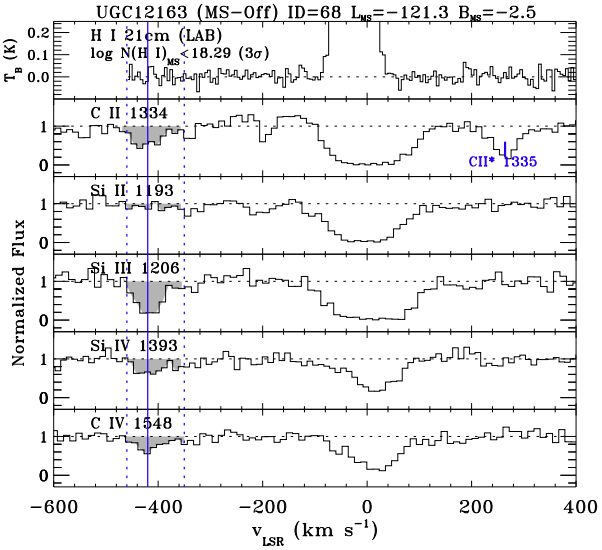
UGC12163 (MS−0ff) ID=68 L_MS=−121.3 B_MS=−2.5
H I 21cm (LAB)
log N(H I)_MS<18.29 (3σ)
C II 1334
CII* 1335
Si II 1193
Si III 1206
Si IV 1393
C IV 1548
T_B (K)
Normalized Flux
v_LSR (km s^−1)

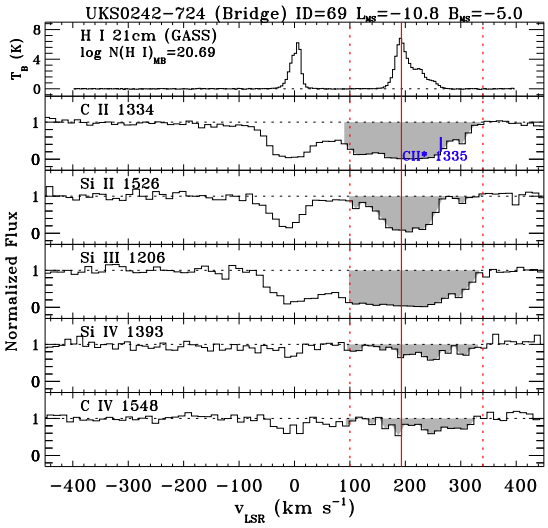
UKS0242−724 (Bridge) ID=69 L_MS=−10.8 B_MS=−5.0
H I 21cm (GASS)
log N(H I)_MB=20.69
C II 1334
CII* 1335
Si II 1526
Si III 1206
Si IV 1393
C IV 1548
T_B (K)
Normalized Flux
v_LSR (km s^−1)

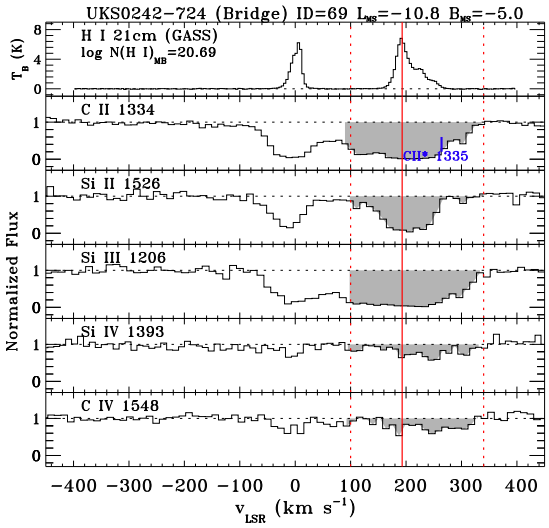
UKS0242−724 (Bridge) ID=69 L_MS=−10.8 B_MS=−5.0
H I 21cm (GASS)
log N(H I)_MB=20.69
C II 1334
CII* 1335
Si II 1526
Si III 1206
Si IV 1393
C IV 1548
T_B (K)
Normalized Flux
v_LSR (km s^−1)